EXPLORING INTERFACIAL PHENOMENA IN PHOTOVOLTAIC MATERIALS STRUCTURES USING FIRST-PRINCIPLES CALCULATIONS AND BEYOND

by

Michael J. Waters

A dissertation submitted in partial fulfillment
of the requirements for the degree of
Doctor of Philosophy
(Materials Science and Engineering)
in the University of Michigan
2016

Doctoral Committee:
    Professor John Kieffer, Chair
    Assistant Professor Emmanouil Kioupakis
    Associate Professor Max Shtein
    Professor Robert M. Ziff

Acknowledgements

First and foremost, I am grateful for the patience of my thesis advisor, John Kieffer, and his willingness to let me engage in projects with long-term rewards and short-term risks. This willingness, combined with funding from the U of M School of Information, allowed Katherine Sebeck, Eleanor Coyle, and myself to unify our group's programming efforts and create our simulation management environment, Kirke. By our combined efforts to develop Kirke, I have been able manage the many simulations, and the analysis and rendering thereof, contained in this document.

Secondly, I must whole-heartedly thank Dr. Hossein Hashemi for thoroughly introducing me to the field of electronic structure calculations, for his day-to-day feedback, and for his ability to focus my sometimes-chaotic productivity.

Finally, I must thank my parents for their unwavering support in all aspects of my education. Even when I was relegated to special education classes for my attention deficit disorder, they spent many hours ensuring that my homework was complete and that I understood the lessons.

Table of Contents

List of Tables

List of Figures

Abstract

Photovoltaics are a large part of the global strategy to reduce carbon dioxide emissions. The strict processing requirements of silicon are viewed as economic and technical barriers to larger scale deployment of solar energy. Many of these materials have photocurrents limited by dissociation of bound excited states. The separation between the photo-excited electron and the hole it leaves behind at the interface between the donor and acceptor material is at the core of the functional response of an organic photovoltaic (OPV) device. We therefore examine the effects of interfacial electrostatics in a semi-classical manner on these excited states for both an organic interface and a hybrid organic-inorganic interface. We use boron subphtalocyanine chloride and C_{60} as our organic interface wherein we also simulate the effects of thermal motion on the excited state energetics using *ab initio* molecular dynamics. For our hybrid interface, we use pentacene and silicon for which the applicability of our model depends on surface termination. We develop a semi-classical model for the description of dissociation between electron and hole, which takes into account the difference of dielectric constants of the materials juxtaposed at the interface, as well as the potentially polar nature of the interfacial termination. Particularly this latter effect can be exploited for device performance optimization.

Hence, using *ab intio* modeling, we explore possible modifications of boron subphthalocyanine chloride derivatives to control the dipole associated with these molecules and their photonic properties. We substitute the axial boron and chlorine atoms for other trivalent and halogen atoms in our derivatives. Through *ab intio* modeling, we explore boron subphthalocyanine chloride derivatives as possible organic photovoltaic materials. Possible

crystal structures are predicted and their electronic and photonic properties for the proposed derivatives. Many of these materials have photocurrents limited by dissociation of bound excited states.

We further refine the semi-classical model, leading to a quantum mechanical model based on the effective mass Schrödinger equation, which utilizes a self-consistent approach for the calculation of excited states. This model reveals that at hybrid organic/inorganic interfaces, the excited electron-hole configuration transitions from a regime where both reside in the donor phase to a regime where they are predominantly separated across the interface, which is uniquely controlled by the attraction between electron and hole and the band edge offset.

CHAPTER 1

Introduction

1.1   Introduction to Computational Science

While the underlying theory of a general purpose computer had already been worked out, the announcement of the ENIAC computer in early 1946 is considered to the genesis of computational science.[1] In the past 70 years, computer simulation has spread to every field of science and has resulted in multiple Nobel prizes. But to the uninitiated, this is a great deal of fuss over computers, which are, despite their original intent, mostly used for communication and entertainment.[2] To enlighten the reader, it is best to describe how and why we do experiments so as to better understand the nature of simulation.

When a scientist wants to learn about some physical system, they have several options. One possibility is, they can look to see if that something has previously been measured for their system. For common systems like steel alloys, rats, aqueous solutions, wheat, carbon nuclei etc., the answer is usually yes, and the scientist can find the information somewhere. If that something about their system follows fairly simple physical laws, they might be able to calculate this thing they want to know accurately enough. Some good examples of this might be water flow rate inside of a pipe, two body orbital mechanics, or voltages inside of a simple circuit. If the system follows complicated and deeply fundamental physical laws, and the scientist deeply enjoys mathematics, they may still try to calculate the thing they are interested by using many approximations and mathematical tricks. These are usually problems like compressible fluid flow, general relativity, and quantum electrodynamics.

The problem with this approach is that the scientist may waste a great amount of time while making no progress, but sometimes, the results are profound and widely helpful.

So if a scientist wants to know something about a physical system, but cannot find that information, cannot use a simple model, and does not want to risk a lengthy calculation, they'll have to conduct an experiment themselves. But there are limits on what can be done in an experiment. Some things are too large to be an experiment. For example, we cannot build our own continents to test plate tectonics, nor can we build our own stars to test stellar fusion. In the end, we are usually limited to experiments that are smaller than a football field. When it comes to time scale of experiments, scientists are unfortunately limited to conducting experiments that are shorter than the average human life expectancy. From these constraints, we can make a map of experiments based on size and time scale as shown in Figure 1.1. Even inside the realm of things that can be experiments, there is another factor: cost. For whatever reason, things that happen very quickly like the particle physics ($<10^{-20}$ s) in the Large Hadron Collider or are as large as the International Space Station ($\approx 10^2$ m) or some combination of the two, roughly form a boundary of steeply increasing cost. For example, an automobile crash test, which involves and an automobile ($\approx 10^1$ m) and a crash ($\approx 10^{-1}$ s) and requires the destruction of a new car on top of the cost of all the scientific equipment and technician time can easily exceed median income of the United States.[3] Thankfully, computer simulations can fill in some of the hard to reach areas in this picture.
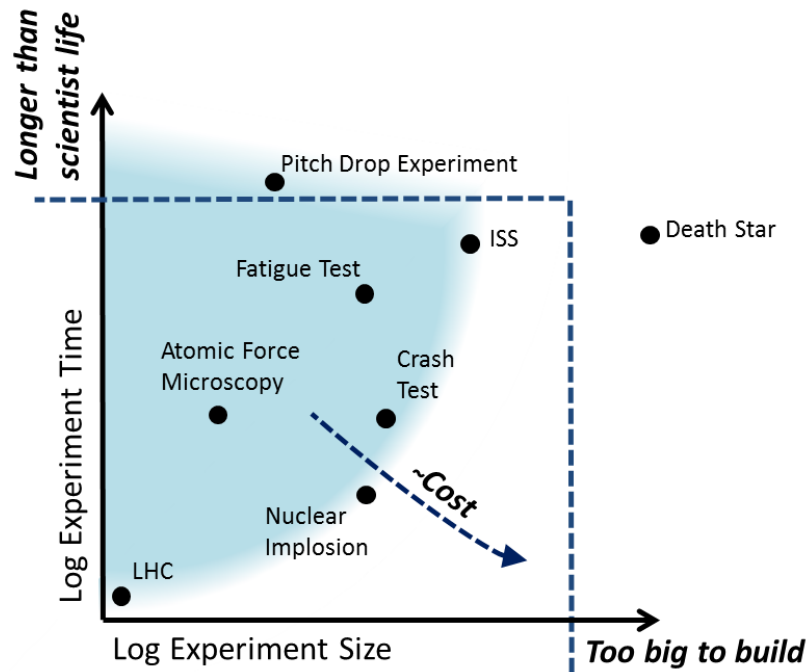
Figure 1.1 A diagram of experiment time and size with some well-known experiments. The shaded blue area is roughly the regime of what are possible experiments.

With computer simulation, there is almost always a means of simulating a system, no-matter the size scale. The crux is that a good mathematical model for the system has to exist for that system at every size scale but for many systems, they do. For example, the mechanical response of a material can be modeled from the kilometer scale down to the millimeter scale using non-linear elasticity and flow plasticity theory. From the millimeter scale down to the 100 nanometer scale, phase field theory works well. From 100 nanometer scale down to the Angstrom scale, atomistic models such as molecular dynamics work well. Below this size scale, macroscopic concepts such as stress and strain become unclear, but density function theory can still model the behavior of chemical bonds well. The only problem is that each time a lower level model is used, computation complexity increases dramatically, i.e. the computer has to work dramatically harder. This sort of behavior generally means that the maximum simulated time decreases every time a lower level model is used. This leads to an overall relationship between simulation size and time scales that is schematically shown in Figure 1.2. Wonderfully, many of the experimentally difficult to reach size and time scales

3

are easily within the reach of simulation. Also, there are more than just size and time scale reasons to use computer simulations. Because computer simulations are not bound by the same rules of as reality, we can also do things that are otherwise impossible in experiment.
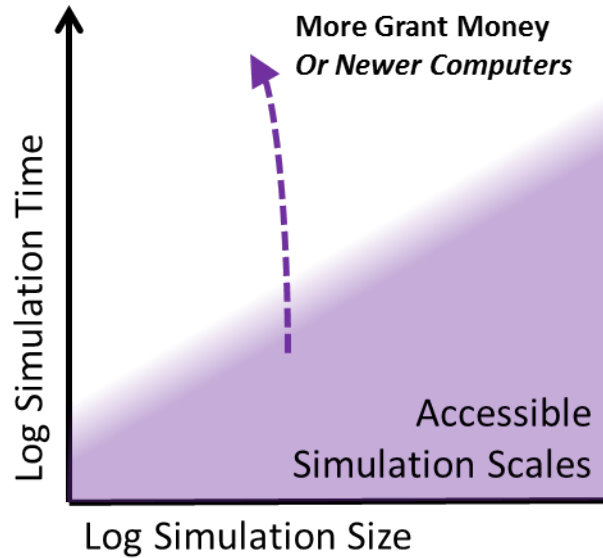
Figure 1.2. Across many simulation types and size scales, there is an upper bound on the amount of time that can be simulated for a simulation size. This time increases with available computational power.

The first and possibly the most important advantage of simulations is the ability to explain and differentiate phenomena. In an experiment where something inexplicable happens, we can perform simulations using the physical laws that we hypothesize are involved. If the inexplicable result is replicated in simulation, we know that the interplay of a set or subset of the physics implemented in simulation give rise to the inexplicable result. From there, physical laws can be eliminated one by one from the simulation one by one till only the ones that reproduce the inexplicable result remain. This is a brute-force means of elucidating the underlying physics of the phenomenon. Simulations can also differentiate phenomena. For example, if an experiment yields some measurement but cannot determine what contributes to that measurement, a simulation of the measurement can be done. Since in the computer

4

all the contributions to a measurement are calculated, it is usually trivial to examine contribution of each phenomenon.

The second area where simulations can excel compared to experiment is in throughput. If someone wants to perform a destructive test on a sample, they often have make/buy/prepare a new sample each time. In a computer, we can email copies of the sample to each other. Some of our simulations have become so well established that the computational cost of performing one is trivial compared to human time required to setup the simulation. In this case, we can automate the setup and execution of simulations to test original samples under a huge number of conditions. We can also do this the other way around, and use automation to perform the same simulated test on many possible design candidates to find the best one quickly. This is known as high-throughput screening.

The third major reason to use simulations is that some experiments are very difficult or impossible to do. We cannot do experiments on neutron star matter on earth because nothing can withstand the required pressures. Experiments involving nuclear chain reactions are generally either illegal or bureaucratic nightmares due to safety and security issues. It is difficult to measure the properties of interfaces in materials, any probing requires mechanical access to the interface which makes it a surface not an interface. Scattering methods like electron microscopy and x-ray scattering can be used on interfaces but don't as work well on molecular materials. This inaccessibility of interfaces is the major motivation for the development of the models presented in chapters two and four.

The majority of the work in this thesis comprises *ab initio* calculations of photovoltaic materials to explore new architectures and materials, and to better understand these solar cells. Ultimately, improvements in solar cells are part of our species' plan to ween ourselves from polluting our atmosphere with carbon dioxide to power our machines. Because *ab initio* calculations are the most computationally intensive class of calculations in materials science, there is considerable irony given the amount of carbon dioxide released as a

byproduct of the electrical energy that powered the processors used to perform the calculations with the purpose of reducing global carbon dioxide emissions.

1.2   An Introduction to Ab Initio Calculations

What are *ab initio* and first principles models/calculations/simulations? In the context of materials modeling, *ab initio*, which literally translates to 'from the beginning', and first principles both imply that by beginning with the quantum mechanical behavior of electrons, you can predict materials properties. Ironically, all of these methods are based on the Schrodinger equation in some form or another and not on quantum electrodynamics which makes them, in fact, still approximations. Nonetheless, any model that captures significant phenomena is wise to disregard unnecessary complexity. This brings us back to the Schrodinger equation, because it and its many variations are sufficient for describing most materials. In its most concise form it is:

$$\widehat{H}\Psi = E\Psi$$

Where $\widehat{H}$ is the Hamiltonian operator, Ψ is the wave function, and E is the energy eigenvalue. Unfortunately, this is very alien to those unfamiliar with quantum mechanics. In practical application, the Schrodinger equation is more of a recipe for constructing quantum mechanical problems than an all-encompassing solution in the same way that the proper use of Newton's laws allows the solution of classical mechanical problems.

As a gentle introduction, starting with a single particle, 1-dimensional, time independent case in real space we have:

$$\widehat{H} = -\frac{\hbar^2}{2m}\frac{\partial^2}{\partial x^2} + V$$

$$-\frac{\hbar^2}{2m}\frac{\partial^2 \psi}{\partial x^2} + V\psi = E\psi$$

The wave function ψ is related to the probability density, ρ, of the particle being at a certain x value via $\psi^*\psi = \rho$. (This means wave functions have strange units due to the space in which they are defined. In this linear example, the units are $electrons/\sqrt{meter}$.) The first term represents kinetic energy, and V is the potential energy imposed on the particle through some interaction as a function of position. Finally, E is the energy of the particle. E is also the energy eigenvalue. What this means is that only some functional forms of ψ can solve this equation and for each functional form (eigenvector), there is only one energy eigenvalue. This can be more easily understood if this differential equation is conceptualized as a linear algebra problem. As an example, in this matrix formulation we have discretized the x coordinate in periodic system. The Hamiltonian is represented as a matrix and the wave function as a vector.

$$\mathbf{H}\begin{bmatrix}\psi_1\\\psi_2\\\psi_3\\\psi_4\\\psi_5\end{bmatrix} = E\begin{bmatrix}\psi_1\\\psi_2\\\psi_3\\\psi_4\\\psi_5\end{bmatrix}$$

$$\left(\frac{-\hbar^2}{2m}\frac{1}{(\Delta x)^2}\begin{bmatrix}-2 & 1 & 0 & 0 & 1\\1 & -2 & 1 & 0 & 0\\0 & 1 & -2 & 1 & 0\\0 & 0 & 1 & -2 & 1\\1 & 0 & 0 & 1 & -2\end{bmatrix} + \begin{bmatrix}V_1 & 0 & 0 & 0 & 0\\0 & V_2 & 0 & 0 & 0\\0 & 0 & V_3 & 0 & 0\\0 & 0 & 0 & V_4 & 0\\0 & 0 & 0 & 0 & V_5\end{bmatrix}\right)\begin{bmatrix}\psi_1\\\psi_2\\\psi_3\\\psi_4\\\psi_5\end{bmatrix} = E\begin{bmatrix}\psi_1\\\psi_2\\\psi_3\\\psi_4\\\psi_5\end{bmatrix}$$

Since we don't know E or ψ, but do know the Hamiltonian matrix, this is an eigenvalue problem where the state energies are eigenvalues and the eigenvectors are the spatial variation of the state wave functions. In this case, there are 5 energy eigenvalues and 5 eigenvectors. In reality, with its continuous space there can be infinitely many. The only problem for real systems is that they have many electrons and finding eigenvalues becomes expensive. Using an orthonormal basis set of functions to represent wave functions is the most common means of reducing the work involved. For example, the spherical harmonics

and Gaussians are often used to represent atomic and molecular orbitals (MO) because they are so similar and only require a few coefficients to represent the MO well. Since the basis has known mathematical properties and only coefficients need to be saved, much computational efficiency is gained. In periodic systems, plane waves are a common choice.

1.2.1 Multiple Electrons and Hartree-Fock

What about multiple electrons? The first and simplest approximation is the uncorrelated wave function. Basically, when constructing a wave function for a multi-electron system, is the probability of finding an electron at a certain place dependent on the probability of another electron being found at some other location? If so, then the electron wave function depends on 6 dimensions. (3N dimensions for the N-electron system). However if our electrons are uncorrelated, then the probability of finding an electron at a location is just the product of the two independent probability densities. As a wave function this looks like this:

$$\Psi(\mathbf{r}_1, \mathbf{r}_2) = \psi_1(\mathbf{r}_1)\psi_2(\mathbf{r}_2)$$

This approximation is a good one. Except for a small subclass of materials known as strongly correlated materials (such as super conductors), this can mostly be ignored. Also, it creates two 3-dimenstional problems out of a 6-dimentional problem, which is highly preferable computationally.

The next and possibly least intuitive component is the exchange interaction. I will cover it shortly for completeness sake, but for a more thorough description (14 pages long), see Leach.[4]Briefly, because electrons are indistinguishable, only the total wave function is disguisable (i.e. observable). This means that electron one in state *a* and electron two in *b* cannot be distinguished from electron one in state *b* and electron two in state *a*. The total wave function cannot be changed if the two electrons are swapped since this would affect the total energy. The answer is that total wave function can be expressed in symmetric and

anti-symmetric ways, which leave the total wave function intact when the electrons are exchanged. The symmetric and anti-symmetric cases are:

$$\Psi(\mathbf{r}_1, \mathbf{r}_2) = \frac{1}{\sqrt{2}}[\psi_1(\mathbf{r}_1)\psi_2(\mathbf{r}_2) + \psi_1(\mathbf{r}_2)\psi_2(\mathbf{r}_1)]$$

$$\Psi(\mathbf{r}_1, \mathbf{r}_2) = \frac{1}{\sqrt{2}}[\psi_1(\mathbf{r}_1)\psi_2(\mathbf{r}_2) - \psi_1(\mathbf{r}_2)\psi_2(\mathbf{r}_1)]$$

The symmetric and anti-symmetric wave functions alone does not create an immediate peculiarity because they are merely a result of statistics, however, the inclusion of intrinsic spin does create a peculiarity. For spin-1/2 particles like electrons, symmetric total wave functions equate to zero. So, total electron wave functions must be anti-symmetric. This is where most authors would explore the slater determinate for its simple representation of the antisymmetric total N-electron wave function, but this should be left to more eloquent and patient authors.

With the multi-electron wave function glossed over, the next step is a multi-electron Hamiltonian. For two electrons:

$$\widehat{H} = -\frac{\hbar^2}{2m}\nabla_{\mathbf{r}_1}^2 - \frac{\hbar^2}{2m}\nabla_{\mathbf{r}_2}^2 + V_{int}(\mathbf{r}_1, \mathbf{r}_2) + V_{ext}$$

The kinetic energy of an electron is represented by the Laplacian of the total wave function with respect to that electron's position. (For a correlated wave function, this Laplacian couples the masses.) The next term, V_{int}, is the interaction potential, V_{ext}, which depends on the location of the two electrons. The final term, V_{ext}, represents an externally applied potential, which for materials, represents the field of nuclear cores, applied fields, *etc*. The simplest and strongest electron-electron interaction is the Coulomb interaction which is formulated as:

$$V_{int}(\mathbf{r_1}, \mathbf{r_2}) = \frac{e^2}{4\pi\epsilon_o |\mathbf{r_1} - \mathbf{r_2}|}$$

For the total energy of this two electron system, we rely on the expectation value of the Hamiltonian to tell us the total energy:

$$E = \frac{\int\int \Psi^* \hat{H} \Psi d\mathbf{r_1} d\mathbf{r_2}}{\int\int \Psi^* \Psi d\mathbf{r_1} d\mathbf{r_2}}$$

For the two electron system with the proper anti-symmetric wave functions, this expands to:

$$E = -\frac{\hbar^2}{2m} \int \psi_1^* \nabla_{\mathbf{r_1}}^2 \psi_1 d\mathbf{r_1} - \frac{\hbar^2}{2m} \int \psi_2^* \nabla_{\mathbf{r_2}}^2 \psi_2 d\mathbf{r_2}$$

$$+ \frac{e^2}{4\pi\epsilon_o} \int\int \frac{\psi_1^*(\mathbf{r_1})\psi_1(\mathbf{r_1})\psi_2^*(\mathbf{r_2})\psi_2(\mathbf{r_2})}{|\mathbf{r_1} - \mathbf{r_2}|} d\mathbf{r_1} d\mathbf{r_2}$$

$$- \frac{e^2}{4\pi\epsilon_o} \int\int \frac{\psi_1^*(\mathbf{r_1})\psi_2(\mathbf{r_2})\psi_1^*(\mathbf{r_2})\psi_2(\mathbf{r_1})}{|\mathbf{r_1} - \mathbf{r_2}|} d\mathbf{r_1} d\mathbf{r_2}$$

$$+ \int \psi_1^* \psi_1 V_{ext}(\mathbf{r_1}) d\mathbf{r_1} + \int \psi_2^* \psi_2 V_{ext}(\mathbf{r_2}) d\mathbf{r_2}$$

The first two terms are the kinetic energy and the third is the coulomb integral between the charge densities of the two electrons. This is sometimes referred to as K_{12}

$$K_{12} = \frac{e^2}{4\pi\epsilon_o} \int\int \frac{\psi_1^*(\mathbf{r_1})\psi_1(\mathbf{r_1})\psi_2^*(\mathbf{r_2})\psi_2(\mathbf{r_2})}{|\mathbf{r_1} - \mathbf{r_2}|} d\mathbf{r_1} d\mathbf{r_2}$$

The fourth term is the exchange energy also known as J_{12}. It is the result of the anti-symmetric component of the total wave function going into to coulomb interaction. This is known as the exchange integral.

$$J_{12} = \frac{e^2}{4\pi\epsilon_o} \int\int \frac{\psi_1^*(\mathbf{r_1})\psi_2(\mathbf{r_2})\psi_1^*(\mathbf{r_2})\psi_2(\mathbf{r_1})}{|\mathbf{r_1} - \mathbf{r_2}|} d\mathbf{r_1} d\mathbf{r_2}$$

It is important to note that in multi-electron system, exchange terms not involving both electrons of the two-electron operator go to zero. So for the multi-electron system, we only need to consider all the possible pairs of electrons. Finally, the last two terms represent the effect of the external potential on the electrons.

From here we will switch to a multi-electron description by summing over all the electrons for the single-electron operators of the Hamiltonian namely the kinetic energy and the external field interaction. For the coulomb and exchange interaction energies K_{ij} and J_{ij}, we can sum over all pairs or in the case below double count and divide by 2. Since $K_{ii} - J_{ii} = 0$, we don't have the exclude these terms from the sum.

$$E = -\frac{\hbar^2}{2m}\sum_i \int \psi_i^* \nabla_{\mathbf{r}_i}^2 \psi_i d\mathbf{r}_i + \frac{1}{2}\sum_{i,j}(K_{ij} - J_{ij}) + \sum_i \int \psi_i^* \psi_i V_{ext}(\mathbf{r}_i) d\mathbf{r}_i$$

This is the Hartree-Fock formulation for the electron energy. It has exact exchange and no correlation correction. By applying the variational principle to this, we can get the Fock equation or a single particle Hamiltonian which reduces the problem to a single particle equation. But first, we should create Coulomb $k_i(\mathbf{r}_i)$ and exchange $j_i(\mathbf{r}_i)$ one-electron operators:

$$k_i(\mathbf{r}_i) = \frac{e^2}{4\pi\epsilon_o}\sum_{j\neq i} \int \frac{\psi_j^*(\mathbf{r}_j)\psi_j(\mathbf{r}_j)}{|\mathbf{r}_i - \mathbf{r}_j|} d\mathbf{r}_j$$

$$j_i(\mathbf{r}_i)\psi_i(\mathbf{r}_i) = \frac{e^2}{4\pi\epsilon_o}\sum_{j\neq i}\left[\psi_j^*(\mathbf{r}_i)\int d\mathbf{r}_j \frac{\psi_i^*(\mathbf{r}_j)\psi_j(\mathbf{r}_j)}{|\mathbf{r}_i - \mathbf{r}_j|}\right]$$

The exchange operator is an integral operator and it has to be this way so that the expectation value computes correctly. This all results in the Fock equation:

$$\left(-\frac{\hbar^2}{2m}\nabla_{\mathbf{r}_i}^2 + V_{ext}(\mathbf{r}_i) + k_i(\mathbf{r}_i) - j_i(\mathbf{r}_i)\right)\psi_i = \varepsilon_i\psi_i$$

11

Where the ε_i is the energy eigenvalue of an electron. This equation is hugely important because allow each electron to be solved separately and then updated with each other and re-solved in a self-consistent manner (self-consistent iteration). The single particle Hamiltonian is also hugely important since it is what is actually implemented in software for solving electronic structure problems.

Before continuing, it's important to discuss the meaning of these energy eigenvalues. The energy eigenvalue reflects the energy level of an electron relative to vacuum. Or more simply the negative of the energy required to remove the electron from the system while keeping all the other electrons frozen. Or mathematically:

$$\sum_i \varepsilon_i \neq E$$

1.2.2 DFT and Beyond

Any astute computationalist will have noticed that a naïve implementation of Hartree-Fock will be at least $O(N^4)$ if the single particle wave functions are exactly. D1sson solver (fast Fourier transform, fast multipole method, multilevel summation method, etc.) on the coulomb integral to speed that up but that still leaves the computationally nasty exchange term. The solution is yet another set of approximations that lead to density functional theory (DFT).

The main idea is that we try to treat the electron density rather than the wave functions as much as possible. To start, the electron density is defined as:

$$\rho(\mathbf{r}) = \sum_i \psi_i^*(\mathbf{r})\psi_i(\mathbf{r})$$

And the total number N of electrons:

$$N = \int \rho(\mathbf{r})d\mathbf{r}$$

Using this we can write the total energy as a functional of the electron density as per suggestion of Kohn and Sham[6]:

$$E[\rho(\mathbf{r})] = E_{KE}[\rho(\mathbf{r})] + E_{ext}[\rho(\mathbf{r})] + E_H[\rho(\mathbf{r})] + E_{XC}[\rho(\mathbf{r})]$$

The first term is the kinetic energy, followed by the interaction with an external potential, the classical coulombic intra-action of the electron density (Hartree energy), and finally a functional for the exchange and correlation correction (not necessarily combined).

The kinetic energy functional is:

$$E_{KE}[\rho(\mathbf{r})] = -\frac{\hbar^2}{2m} \sum_i \int \psi_i^* \nabla_{\mathbf{r}_i}^2 \psi_i d\mathbf{r}_i$$

The external energy functional is:

$$E_{ext}[\rho(\mathbf{r})] = \int \rho(\mathbf{r}) V_{ext}(\mathbf{r}) d\mathbf{r}$$

The Hartree functional is the classical self-interaction of a charge density (again the ½ for the double counting):

$$E_H[\rho(\mathbf{r})] = \frac{1}{2} \frac{e^2}{4\pi\epsilon_o} \int \int \frac{\rho(\mathbf{r}_1)\rho(\mathbf{r}_2)}{|\mathbf{r}_1 - \mathbf{r}_2|} d\mathbf{r}_1 d\mathbf{r}_2$$

And finally the exchange and correlation energy is:

$$E_{XC}[\rho(\mathbf{r})] = ?$$

Nobody knows or will likely ever know the exact or even optimal form, however there are great approximations. Now the resulting single particle Hamiltonian known as a Kohn-Sham equation is:

$$\left(-\frac{\hbar^2}{2m} \nabla_{\mathbf{r}_1}^2 + V_{ext}(\mathbf{r}_1) + \frac{e^2}{4\pi\epsilon_o} \int \frac{\rho(\mathbf{r}_2)}{|\mathbf{r}_1 - \mathbf{r}_2|} d\mathbf{r}_2 - V_{XC}[\mathbf{r}_1] \right) \psi_i = \varepsilon_i \psi_i$$

Where,

$$V_{XC}[\mathbf{r}] = \frac{\delta E_{XC}[\rho(\mathbf{r})]}{\delta \rho(\mathbf{r})}$$

This equation should look familiar because it is so similar to the Fock equation. However, it is much more easily solved! The kinetic energy and external potentials were already local (meaning that no integral was needed to calculate them). The Coulombic term is much less difficult than before. In fact, the coulomb potential only needs to be calculated over all space while being reused for all the electrons. Finally, the exchange and correlation functional becomes some sort of local potential for speed reasons.

If only the charge density is used in the exchange and correlation functional, it is referred to as a local density approximation (LDA). If the density and some of the gradients of the density are included, it is referred to as a general(lized) gradient approximation (GGA). There are many formulations of LDA and GGA. Because of an oddity of DFT, it tends to under-predict band gaps and highest occupied, lowest unoccupied molecular orbital, HOMO/LUMO, gaps in materials and molecules. However, Hartree-Fock tends to over predict it. Because of this, there are many hybrid formulations that can be tuned by a linear mixing parameter to correctly predict band gaps. None of the methods above have mentioned electron spin or spin-density, and spin polarized versions of all of these theories exist. For transition metals, a popular correction for correlation and spin-polarized systems called LDA+U based on the Hubbard Hamiltonian and on-site energies is common.[7] Currently, the most popular approximation for correctly calculating electronic structure beyond the ground state is the GW approximation for Σ, which is the self-interaction energy correction through polarization of the other electrons.[8]

None of these methods address excited state wave functions properly. The desire to simulate excited states has lead to the development of time-dependent DFT (TDDFT). More recently, the Bethe-Salpeter equation is used to solve for correlated electron-hole

excitations. There are more methods still, but these are getting far outside the scope of a relatively brief introduction.

1.3 References

1.   *ENIAC: Celebrating Penn Engineering History*. University of Pennsylvania School of Engineering and Applied Science, 2016.

2.   Ofcom, *The Communications Market 2015 (August)*, 2015.

3.   Proctor, C. D.-W. A. B. D. "Income and Poverty in the United States: 2013." U.S. CENSUS BUREAU (2014)

4.   Leach, A. R. 2001. Molecular Modelling Principles and Applications, Second Edition. Pearson.

5.   Whitfield, J. D., P. J. Love, and A. Aspuru-Guzik "Computational complexity in electronic structure." Phys. Chem. Chem. Phys. 15 (2): 397–411. (2013)

6.   Kohn, W. "Self-Consistent Equations Including Exchange and Correlation Effects." Physical Review 140 (4A): A1133–A1138. (1965)

7.   Liechtenstein, A. I. "Density-functional theory and strong interactions: Orbital ordering in Mott-Hubbard insulators." Physical Review B 52 (8): R5467–R5470. (1995)

8.   Shishkin, M. "Accurate Quasiparticle Spectra from Self-Consistent GW Calculations with Vertex Corrections." Physical Review Letters 99 (24): 246403. (2007)

CHAPTER 2

Semi-Classical Model for Calculating Exciton and Polaron Pair Energetics at Interfaces

2.0 Synopsis

Exciton and polaron pair dissociation is a functional requirement of photovoltaic devices. To improve upon the current state of interfacial transport models, we augment the existing classical models of dielectric interfaces by incorporating *ab initio* simulations, allowing us to calculate exciton and polaron binding energies more accurately. We demonstrate the predictive capabilities of this new model using two interfaces: (i) the boron subphthalocyanine chloride (SubPc) and C_{60} interface which is an archetype for many organic photovoltaic devices; and (ii) pentacene and silicon (100), which represents a hybrid between organic and inorganic semiconductors. We find that molecular dipoles may be useful as an engineering parameter for improving polaron pair dissociation and that sharp transitions in permittivity can have a stronger effect on polaron pair dissociation than even the electron-hole Coulomb interaction.

2.1 Motivation and Background

In all photovoltaic devices, photons excite charge carriers that must be separated and collected to generate current. In all materials, the excited electron and the pseudo particle hole interact. In most cases, this interaction is dominated by the Coulomb component, which acts to bind the excited electron and hole into a charge neutral effective particle: the

17

exciton. When an exciton becomes split over and interface where the electron and hole are mostly located on opposite sides of the interface yet still bound, a polaron pair is formed. The polaron pair binding energy is one of the largest limiting factors to the performance of organic and hybrid organic/inorganic photovoltaic devices. It subtracts from the open circuit voltage and directly limits the device current via the dissociation rate of polaron pairs at the accepter/donor interface (shown in Figure 2.1).[1, 2] Direct measurement of polaron pair states is difficult and progress with respect to the theoretical description of polar pair dissociation kinetics has been slow, limiting the accuracy of device scale transport models. The most commonly used models are based the Onsager-Braun models.[1-3] Onsager's original model was developed for the electric field assisted dissociation of ions in solution,[4] which Braun applied to the dissociation of excitons and charge transfer states.[5] While some shortcomings of these models in describing polaron pairs have already been pointed out in the literature, [6] here we examine the electrostatics of the interface and the excitonic differences of the two materials. The effect of the excitonic differences between materials on the polaron pair behavior can be best understood by reviewing the two prototypical forms of excitons discussed below. Following this, we present a short review of the theory as its stands for exciton and polaron pairs at heterojunctions.
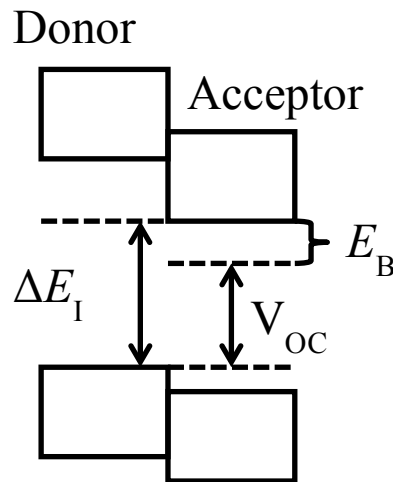
Donor

Acceptor

ΔE_{I}

E_{B}

V_{OC}

2.1.1 Wannier Excitons

In traditional semiconductors made of inorganic materials, photo-excited electrons and their holes behave, for most intents and purposes, as separate particles. However, weakly bound exciton states do exist, typically called Wannier or Wannier-Mott excitons. These excitons are characterized by hydrogenic states delocalized over many unit cells that travel via wave propagation. The energy levels are quantized as

$$E_n = \frac{\mu e^4}{8(\epsilon h n)^2} = \frac{\mu^*}{\epsilon_r^2} \frac{1}{n^2} \frac{m_e e^4}{8(\epsilon_0 h)^2} = \frac{\mu^*}{\epsilon_r^2} \frac{1}{n^2} R_y \approx \frac{\mu^*}{\epsilon_r^2} \frac{1}{n^2} \times 13.605 \text{ eV},$$

Where $\mu = \frac{m_e^* m_h^*}{m_e^* + m_h^*}$ and $\mu^* = \frac{1}{m_e}\left(\frac{m_e^* m_h^*}{m_e^* + m_h^*}\right)$ are the reduced effective mass and scaled reduced effective mass of the electron-hole pair. n is the quantum number of the exciton. The Bohr radius for the ground state, which gives an approximation for the minimum exciton size is:

$$a_r = \frac{\epsilon h^2}{\mu \pi e^2} = \frac{\epsilon_r}{\mu^*} \frac{\epsilon_0 h^2}{m_e \pi e^2} = \frac{\epsilon_r}{\mu^*} a_0 \approx \frac{\epsilon_r}{\mu^*} \times 0.52918 \text{ Å} \quad (2.0)$$

For most classical semiconductors, which have small effective masses and large dielectric constants, the binding energies are small (usually less than $k_B T$) and the radii are large (10s ofÅ). For example, the above formulas applied to silicon yield a binding energy of 55 meV and a radius of 21 Å.

2.1.2 Frenkel Excitons

In the more recently popularized organic semiconductors, excited electrons are by comparison strongly bound to their holes, forming Frenkel excitons. This binding leads to the exciton pseudo-particle where the electron and hole travel together as an effective

neutral particle. The strong binding and localization mean that Frenkel excitons tend to travel via tunneling from site to site. The binding interaction is usually described as purely Coulombic, as with the Wannier type. The difference is that the strongly localized electron and holes require treatment of the actual wave function rather than treating them as perturbations of valence and conduction bands. A good approximation of the binding energy is:

$$E_{bind} = \frac{e^2}{4\pi\epsilon} \iint \frac{|\psi_h(\mathbf{r}_h)|^2 |\psi_e(\mathbf{r}_e)|^2}{|\mathbf{r}_h - \mathbf{r}_e|} d\mathbf{r}_h d\mathbf{r}_e,$$

Which uses the dielectric permittivity of the bulk material to account for the screening of other atoms and molecules. The exciton radius is oftentimes computed based on a measured binding energy according to

$$r_{e-h} = \frac{e^2}{4\pi\epsilon E_{bind}}.$$

However, the exact spatial distribution of charges is disregarded, which can lead to error. As a case in point, consider that two spherically symmetric co-centered Gaussian charge distributions have a finite binding energy but no distance between them. (See Appendix2.1 for derivation.)

We immediately see that, in the case of the Wannier exciton, spatial confinement of the wave function comes from the interaction between electron and hole, whereas in the case of Frenkel excitons, it comes in part, from the spatial extent of the molecular orbitals. If we consider a polaron pair to be an exciton split over an interface, then three possible pairings of interfaces can be made by categorizing them as combinations of exciton type: Frenkel-Frenkel, Wannier-Wannier, and Frenkel-Wannier.

In the case of the Frenkel-Frenkel pairs, most treat the exciton binding energy with the Mulliken rule from optical measurements.[7-9] Although, some have included classical image potentials from dielectric interfaces into the binding energy considerations.[10] For

20

the most part, it seems that exciton binding energies are calculated from the interaction between the electron and hole states. These are then fed into the Onsager-Braun model to calculate dissociation rates. However a Poole-Frenkel model may be more accurate.[3, 11, 12]

In the case of Wannier-Wannier polaron pairs, there has been much analytical work on solving exciton Hamiltonians in the presence of dielectric interfaces with image potentials near interfaces.[13-17] Unfortunately these calculations have constrained the excitons to one material by application of infinite potential barrier. Ideally, finite potential barriers related to the differing band structures of the two materials would spatially separate the carriers.

In the case of hybrid interface, neither model can accurately describe the system. One may consider hydrogen like states trapped in a half space for one of the carriers, but then each position of the Frenkel-like carrier has a different set of quantized exciton binding energies. To further complicate that matter, the electric field dependence of the dissociation rate requires a full quantum mechanical treatment. Considering the small size of Frenkel excitons relative to Wannier excitons, a hybrid polaron pair might be treatable as a hydrogenic atom in two adjacent dielectric half spaces where one half-space has a finite potential. Some work has been done for hydrogen in a single dielectric material with an infinite half space.[18, 19]

In this work we focus on the statics of the polaron pair binding energy as the first step in the creation of more accurate polaron pair dissociation and recombination rate models. The first part of this paper consists of an overview of electrostatic interaction at a dielectric interface. In the second part, we apply these equations to an interface between C_{60} and boron subphthalocyanine chloride (SubPc) as an example of Frenkel-Frenkel polaron pair. Finally, we examine the interface between pentacene and a silicon (100) surface as an example of Wannier-Frenkel pair.

2.2 Classical Electrostatic Effects

Since most novel or experimental photovoltaic devices tend to be planar due to production via spin coating or some sort of chemical or vapor deposition method, we elected to examine the idealized case of carrier interactions near a planar interface. Since this is a straightforward electrostatics problem, some solutions already exist.[20] The following relations were derived from theses known solutions in the context of device performance in the form of energetic effects on polaron pair binding energy and are summarized here, for a more complete description, see Appendix 2.2.

In the simplest configuration, a single carrier (of charge q_1), rests in material 1 near the interface with material 2. An areal bound charge density is created at the interface due to the difference in the dielectric displacement as seen in Fig. 2.2.
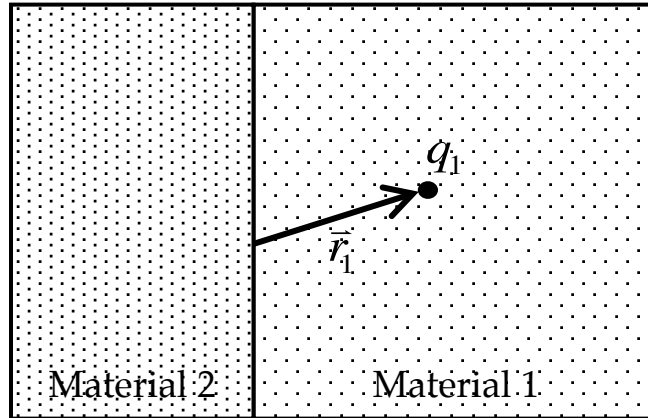
Figure 2.2. A charge of q_1 in located in material 1

This areal bound charge density acts on the carrier to draw it into the material with the higher dielectric constant. The charge interacts effectively with its own image charge.[10] This is the self-polarization energy[21] and it causes the carrier to move away from the interface and deeply into material 1, and is given by Equation 2.1, where h_o is the initial distance to the interface. It should be noted that this energy is proportional to the difference in the dielectric constants and can be either positive or negative.

$$\Delta U_{leave} = -\frac{q_1^2}{16\pi\epsilon_1 h_o}\left(\frac{\epsilon_1-\epsilon_2}{\epsilon_1+\epsilon_2}\right) \quad (2.1)$$
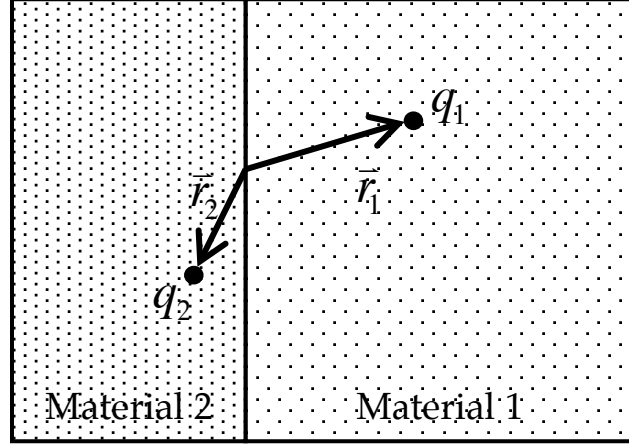
Figure 2.3. Two charges, q_1 and q_2, are located on either side of the interface.

In the case of a polaron pair, two carriers are on either side of the interface between material 1 and material 2 as in Figure2.3.The electrostatic potential between the two carriers is surprisingly simple and is described by Equation 2.2, where d is the distance between the charges.

$$U_{charge-charge} = \frac{q_1 q_2}{4\pi d(\epsilon_1+\epsilon_2)/2} \quad (2.2)$$

This is result is interestingly valid no matter what the positions of the two charges are, so long as they are on different sides of the interface. This result can be easily extended to diffuse charges on either side of the interface in Equation 2.3.

$$U_{charge-charge} = \frac{1}{4\pi(\epsilon_1+\epsilon_2)/2}\int d^3r_1 \int d^3r_2 \left[\frac{\rho_1(\vec{r}_1)\rho_2(\vec{r}_2)}{|\vec{r}_2-\vec{r}_1|}\right] \quad (2.3)$$

The charge densities of the two diffuse charges are ρ_1 and ρ_2.

In some cases, there may be a local polarization of the material near an interface as a result of epitaxy. In the case of perovskites, a thin layer of polarized material can occur as result of epitaxial strain near the interface but be relieved in bulk by misfit dislocations. In the case of

23

an amorphous SubPc film on C_{60}, the preferred molecular orientation of the polar SubPc molecules can lead to local polarization.[22] For a thin polar layer between the two materials the resulting potential field exhibits a discontinuity at the interface. The change in potential across is:

$$\Delta\phi_{2\rightarrow1} = \frac{\sigma_z}{2}\left[\frac{1}{\epsilon_1} + \frac{1}{\epsilon_2}\right] \qquad (2.4)$$

Where σ_z is the areal dipole moment density perpendicular to the interface. Depending on the configuration of the system of interest, this may just accelerate the formation of a polaron pair from the exciton or reduce the polaron pair binding energy. In perovskites, a more complex situation may occur where flexoelectric polarization density decays with distance from the interface as misfit dislocations relieve a lattice mismatch.[23-25] The net result in either system is a small built-in field that can increase or decrease the polaron pair binding energy.

2.3 SubPc on C_{60}

For the SubPc/C_{60} interface, previous work has shown the preferred orientation of SubPc on C_{60}(111) surfaces is the ball-in-cup configuration. In this configuration, it is ultimately favorable for an electron to excite from the HOMO of the SubPc to the LUMO of the C_{60}. [26] This is also observed with phthalocyanine and C_{60}.[27] However, it was not known if room temperature thermal motion would lead to significant variation of the polaron pair binding energy. To investigate this, the thermal motion of an isolated SubPc sitting on the (111) surface of C_{60} is simulated using *ab initio* MD. The C_{60} (111) surface comprises one unit cell containing four C_{60}molecules in a single layer as seen in Figure 2.4. A series of single-point *ab initio* calculations is performed to determine to spatial extent of the SubPc HOMO and the C_{60} LUMO as a function of centroid distance between the two. These are done using a single isolated pair of a SubPc and C_{60} molecules as shown in Figure 2.7.
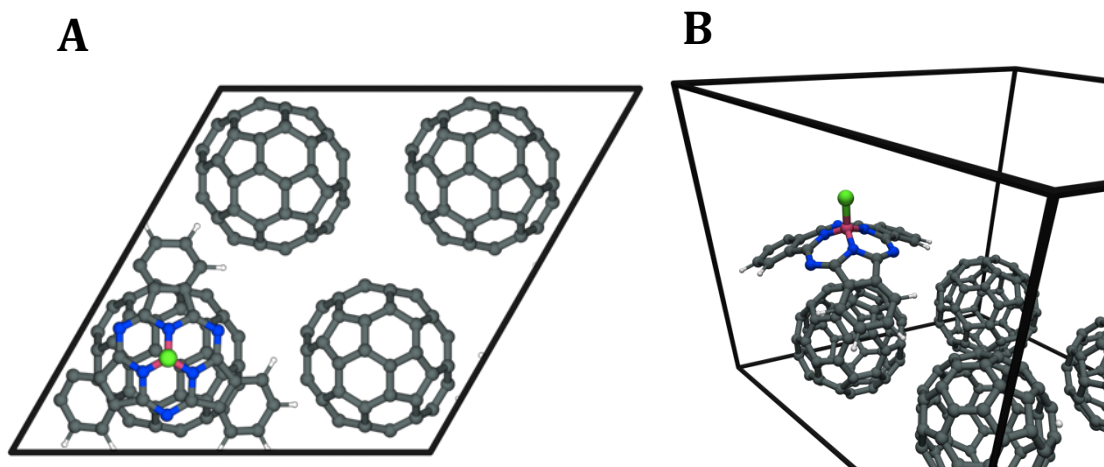
Figure 2.4. (a) Top down view of the SubPc molecule and C$_{60}$ surface. (b) perspective view of the same SubPc molecule and C$_{60}$ surface.

2.4 Pentacene on Silicon

Two (001) silicon slabs were created. One with a bare surface and the other one with a hydrogenated surface, both consisting of 27 layers of silicon atoms (~35 Å thick). The relaxed bare surface exhibits the p(2 x 2) buckled dimer reconstruction and the hydrogenated surface the symmetric dimer reconstruction. There are several reconstructions of the silicon (001) surface with different buckling orders of the dimers. The energy differences between these are less than $k_B T$ per dimer.[28] Projected band structures were calculated for the two surfaces to compare to bulk silicon and identify surface states using relaxed 2 x 2 unit cell slabs. For interactions with pentacene, the 2 x 2 unit cells slabs are duplicated twice in each surface direction to provide enough space for the pentacene molecule. The molecule is placed in line with the dimer ridges. Calculations for each orientation are costly since each system consists of at least 900 atoms. This large number of atoms is required to minimize vertical quantum confinement effect on the electronic structure, which typically is inversely proportional to the square of the slab thickness.
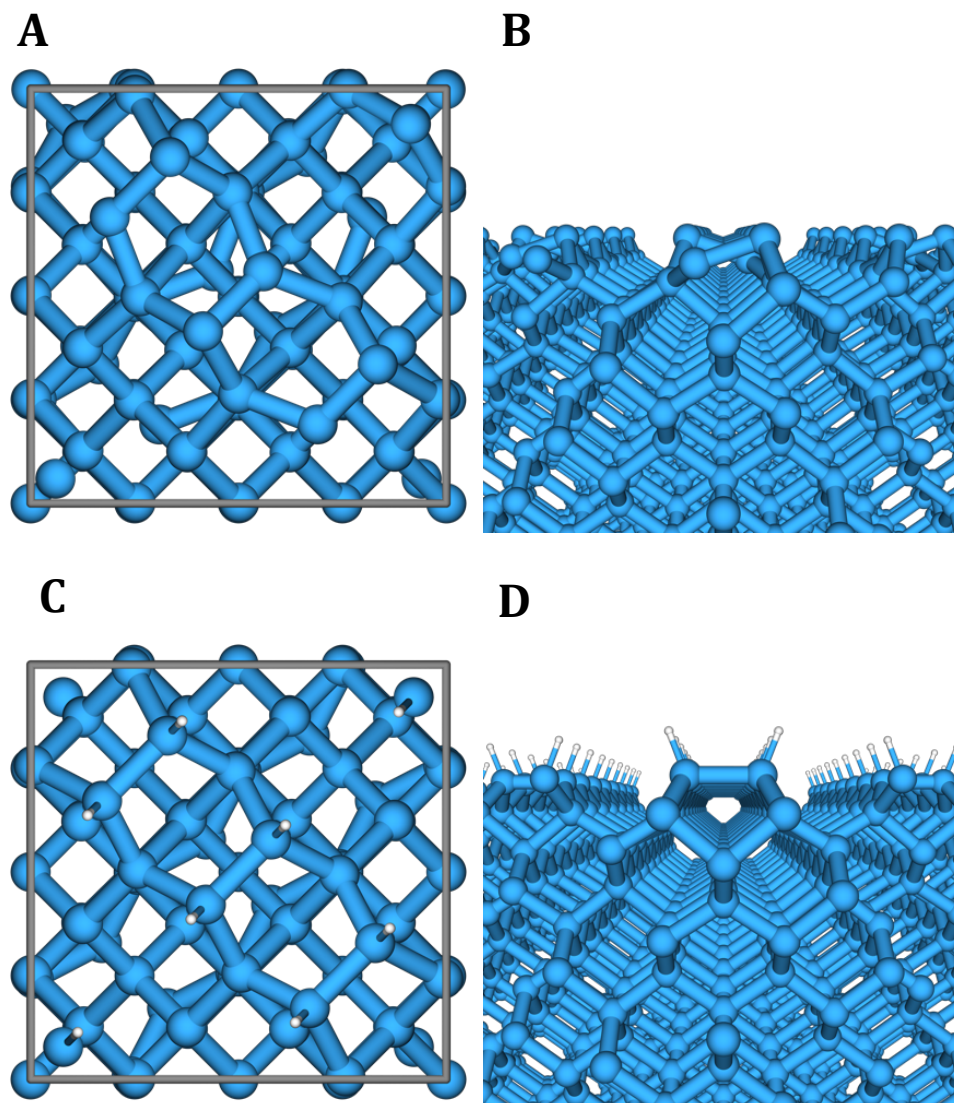
Figure 2.5. (a) The clean silicon (001) surface is viewed top down and (b) along the alternating dimer ridges. (c) The hydrogenated surface is also viewed top down and (c) along the hydrogen terminated dimer ridges

2.5 Methods

2.5.1 SubPc on C_{60}

Ab initio molecular dynamics simulations are done using VASP (version 5.3.3) using the PAW method[29] with the PBE exchange-correlation functional. [30]. Augmented plane waves with a cutoff energy of 120 eV form the basis set. Van der Waals interactions were

accounted for using the VdW-DFT approach developed in Ref.[31, 32] with removed PBE correlation correction. In the initial configuration, a 7 Å vacuum gap was added to the super cell between the chlorine atom of the Subpc molecule and the bottom of the C_{60} to minimize interactions with the periodic images in the surface normal direction (z-direction). Partial occupancies are determined using Gaussian smearing with a width of 0.172 eV. Nuclear motion is integrated with a time step of 1 fs. A Nosé-Hoover thermostat is employed with a target temperature of 300 K and an equilibration time of ~ 3 ps. Once the system is equilibrated, simulations are continued for another 12 ps to capture the relative position space of the C_{60}/SubPc pair. The relative orientation and position of the SubPc molecule at each time step are calculated using Procrustes (Also known as Kabsch) analysis, which is based on computing the least squares rotation matrix after the centroid motion has been accounted for.[33]

A series of single-point electronic structure calculations are performed on the SubPc molecule and the C_{60} molecule immediately beneath it as function of centroid separation distance between the two. For these single point calculations, Gaussian 09, Revision C.01 is used with the B3LYP hybrid functional and the 6-31G(d) basis set. For each centroid distance, a Coulomb integral is evaluated on the density mesh automatically generated by Gaussian. To simplify the intensive six dimensional integral, only cells inside the isodensity surface containing 99 % of the HOMO or LUMO states are used. Effective cell densities are corrected for the loss of the remaining 1%. While this does not change the asymptotic computational complexity of the calculation, it results in a 222-fold speedup at the cost of less than 5 meV error. The Coulombic contribution to the polaron pair binding energy at each time step is interpolated among a series of single point calculations using a cubic spline. All isolated molecular structures are created in Avogadro and relaxed using the built-in potentials before being used as input for *ab initio* calculations.[34]

2.5.2 Pentacene on Silicon

All electronic structure calculations are carried out using VASP version 5.3.5 (build Mar. 31, 2014). The augmented plane wave basis set is cut off at 400 eV and electronic relaxations are converged to an energy difference of 10 μ eV. A Gaussian energy smearing width of 100 meV width is used. The PBE exchange-correlation density functional is used for structural relaxations.[30] The more costly HSE06 hybrid DFT/HF method is used for more accurate electronic structure calculations.[35] For structural relaxations of slabs, ions are relaxed until no atomic force exceeds 10 meV/Å. k-point grids are automatically generated using the Monkhorst-Pack scheme. Total energy calculations of bulk silicon are found to converge within 150 μ eV/atom using an 8 x 8 x 8 k-point grid and the aforementioned plane wave cut-off. The lattice parameter of silicon calculated using HSE06 is used for the construction of silicon slabs. The bulk electronic structure of silicon is calculated using the conventional cell with a 16 x 16 x 16 k-point grid. For the slabs used to compute the projected band structure, a 4 x 4 x 1 k-point grid is used since the slab is not periodic in the surface normal direction. For the final structures with the pentacene molecule, only one k-point is used due to computational cost. Van der Waals interactions between the surface and the pentacene molecule were accounted for using the VdW-DFT method developed in Ref.[31, 32] with removed PBE correlation correction. All slabs have a vacuum gap of 10 Å between the highest and lowest atoms to remove periodic interaction in the surface normal direction. Wave functions are extracted using the WaveTrans[36] code developed for Ref. [37]. Coulomb integrals are calculated as they were in Section 2.5.1 using the dielectric constants of 3.61 for pentacene [38] and 11.7 [39] for silicon.

2.6 Results and Discussion

2.6.1 SubPc on C_{60}

From tracking the relative position and orientation of the SubPc molecule, it's found that the SubPc molecule strays less than 10° from surface normal with a mean of only 3.6°, only the centroid distance to the nearest C_{60} molecule was considered for Coulomb integrals. The distribution of the centroid distributions is shown in Figure 2.6.
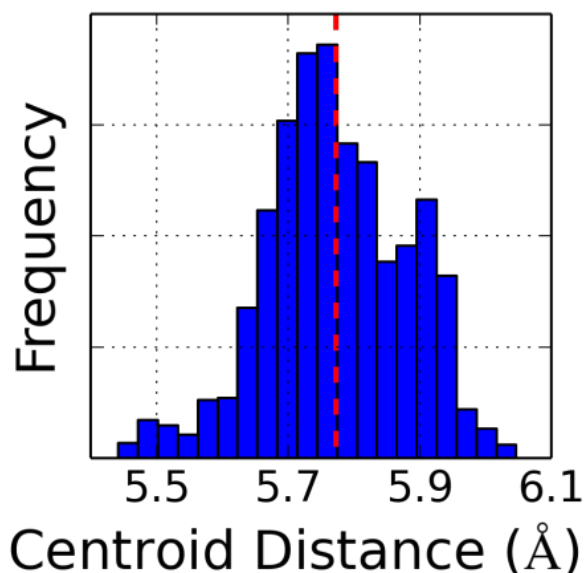
Figure 2.6. **The distribution of the centroid distances of the SubPc molecule and nearest C_{60} molecule with the mean centroid distance shown as a dotted red line.**

For each single-point calculation, Coulomb integrals were evaluated to obtain the Coulombic contribution to the polaron pair binding energy as a function of the centroid distance, as shown in Figure 2.7. The Coulombic contribution to the polaron pair binding energy at each time step was interpolated from the series single-point calculations to get a mean and standard deviation of the Coulombic contribution to the polaron pair binding energy.
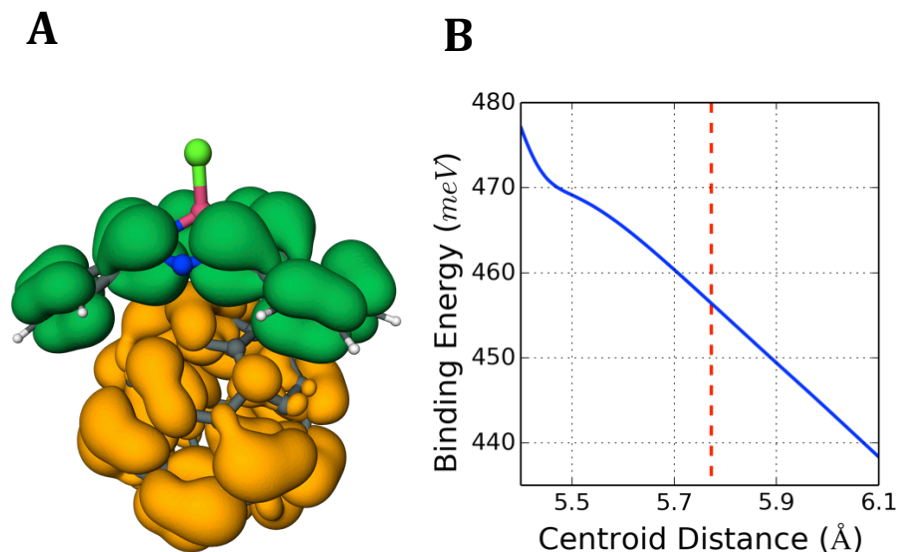
Figure 2.7. (a) The HOMO of the SubPc is shown in green and the LUMO of the C$_{60}$ is shown in gold. Both are shown as isodensity surfaces containing 80% of the state. (b) The Coulomb contribution to the polaron pair binding energy is plotted as function of the centroid distance between the SubPc and C$_{60}$ molecules. The mean centroid distance shown as a dotted red line.

The most important result of the *ab initio* MD simulation is the small effect that thermal motion has on the Coulombic contribution to the polaron pair binding energy. In fact, the difference between the energy associated with the equilibrium position and that of any position within the thermal distribution is safely smaller than $k_B T$. The insignificance of thermal motion in this case is further underscored by the lack of neighboring molecules to hinder motion of the SubPc molecule in our model surface. The charge center approximation often used by simpler models does well to first order, but in the current race for highly efficient devices it is not likely accurate enough considering the 80 meV between the two.

Table 2.1. The Coulomb contribution to the polaron pair binding energy from various calculation methods.

Charge center (Equ. 2.2)	537 meV
Coulomb integral at equilibrium (Equ. 3.3)	457 meV
Coulomb integrals over thermal distribution	456 ± 6 meV

The Coulomb integral results can be combined with an estimate on the upper bound of the effect polarized interface (the net ordering of dipoles at the interface) and the self-polarization energies to gain a better understanding of their relative contributions. The Procrustes analysis shows that the SubPc molecules do not significantly tilt from vertical, which means that their dipole moments are normal to the interface. We estimate the upper bound interface dipole density as the case where half of the C_{60} sites have a vertical SubPc molecule. The upper bound polarized interface energy is large enough to non-trivially weaken the polaron pair binding energy. Without a full experimental or molecular dynamics study of the SubPc molecular orientations it is not possible to accurately calculate this value. It is also important to note that, even though in this case the polarized interface reduces the polaron pair binding energy, there is no reason that, in another system, it could do the opposite. In conjunction with the work in Ref.[44], the effect of the molecular dipole moment on the I-V curve of a real SubPc/C_{60} device is modeled for five cases: no molecular alignment, ¼ of C_{60} sites covered with SubPc molecules, ½ of C_{60} sites covered with SubPc molecules and dipole inversions the last two cases. In Figure 2.8, it can be seen that alignment of the molecular dipoles can have a large effect on device performance.
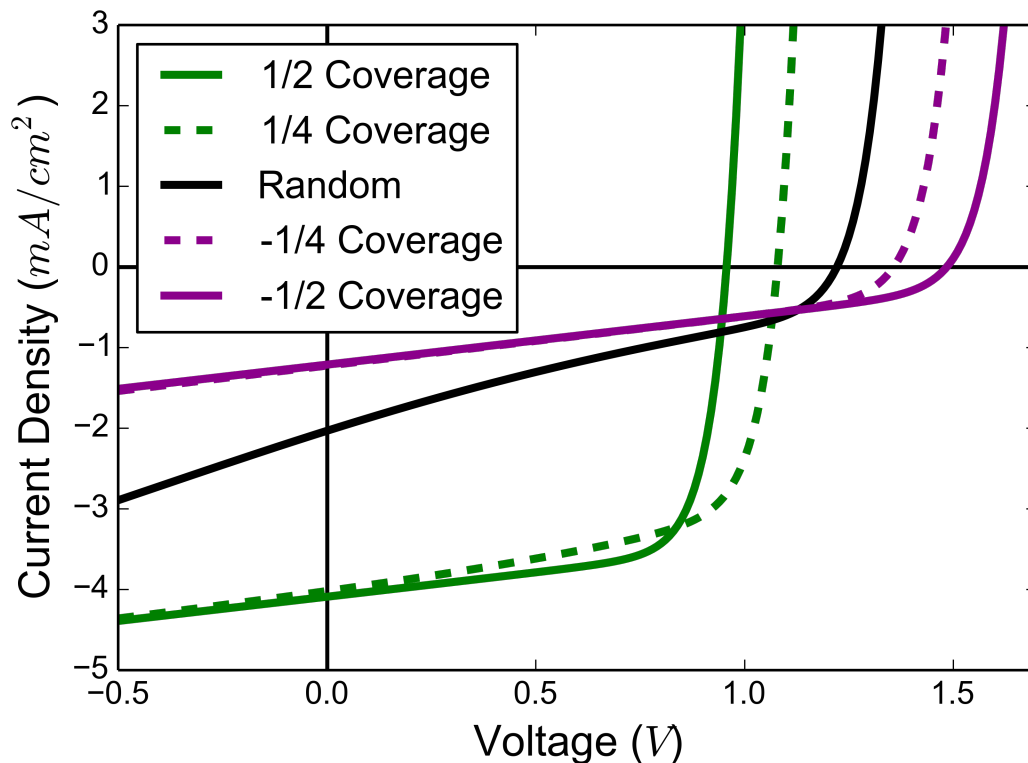
Figure 2.8. The modeled I-V curves for a SubPc/C$_{60}$ device with half of the C$_{60}$ sites covered with SubPc molecules (solid green line), one quarter of the C$_{60}$ sites covered with SubPc molecules (dashed green line), random SubPc molecule orientation (solid black line), one quarter of C$_{60}$ sites covered with inverted SubPc molecules (dashed purple line), and half of C$_{60}$ sites covered with inverted SubPc molecules (solid purple line).

For the self-polarization energy, we estimate the interface is halfway between the lowest hydrogen atom of the SubPc molecule and the highest carbon atom of the neighboring C$_{60}$ molecule. The resulting effects on the polaron pair binding energy are collected in Table 2.2 below. Unsurprisingly, the small difference in permittivity between SubPc and C$_{60}$ gives a negligible self-polarization energy contribution.

Table 2.2 All of the semi–classical corrections to the polaron pair binding energy for the SubPc/C_{60} interface are tabulated. *The polarized interface energy is an upper bound.

Self-Polarization Energy (Equ. 2.1)	17 meV
Polarized Interface Energy* (Equ. 2.4)	-237 meV
Coulomb Contribution (Equ. 2.3)	456 meV
Total Polaron Pair Binding Energy	236 meV

To demonstrate the effect of the dielectric constant, the same device as in Figure 2.8 has been simulated only changing the dielectric permittivity of the C_{60}. The dielectric constant of C_{60} is fictitiously increased from the experimental value of 5.0 to 15.0 in Figure 2.9 below. As the Coulomb interaction weakens, the self-polarization energy grows holding holes in the SubPc more strongly to the interface. The self-polarization energy grows more slowly than the Coulomb energy decreases due to the smaller leading coefficient. The net effect is that increasing the dielectric permittivity improves device performance but there is no significant improvement after a relative permittivity of 10.0.
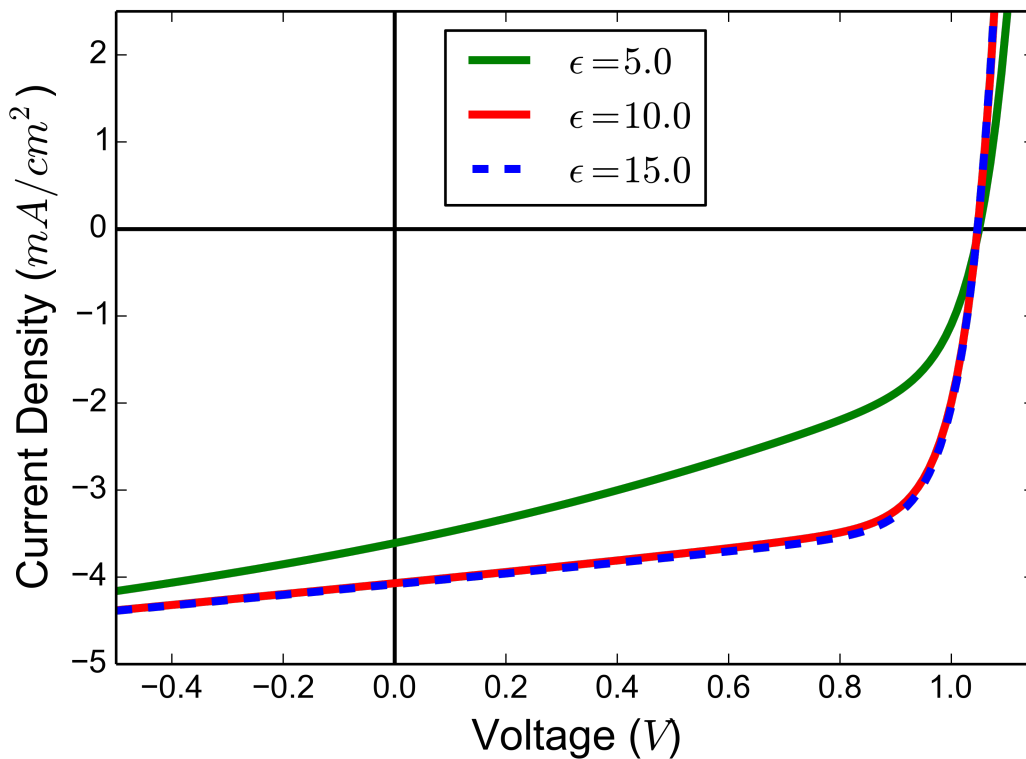
Figure 2.9. Simulated I-V curves of a hypothetical SubPc/C$_{60}$ device where the relative permittivity of C$_{60}$ is the experimental value (solid green line), 10.0 (solid red line), and 15.0 (dashed blue line).

2.6.2 Pentacene on Silicon

For bulk silicon, the lattice parameter and bulk modulus have been calculated using both HSE06 and PBE. Both agree well with experiment for structural and mechanical properties. (Table 2.3) As usual, PBE (and DFT in general) under predicts the band gap, which is why HSE06 was used for electronic structure calculations despite the significant increase in computational cost.

Table 2.3. The calculated properties of silicon compared with experimental values

	PBE	HSE06	Experimental
Lattice Parameter (Å)	5.4685 [+0.72 %]	5.4332 [+0.07 %]	5.4293 (0K)[40]
Bulk Modulus (GPa)	92.5 [-6.28 %]	99.8 [+1.11 %]	98.7 (233 K) calculated from Ref.[41]
Band gap (eV)	0.579 [-50.44 %]	1.158 [-1.03 %]	1.170 (0K) [42]

The projected band structures of the two surfaces reveal distinctly different electronic structures near the band gap. The clean surface has two distinctive bands that sit in the middle of the band gap as seen in Figure. 2.10a. These bands can clearly be seen to be surface states associated with the surface reconstruction in Figure2.10c and 2.10d. The band gap for the clean surface is 0.615 eV (1.268 eV if the surface states are ignored) and 1.209 eV for the hydrogenated surface. These band gaps are slightly larger than the bulk band gap, which is easily attributable to quantum confinement in the z-direction.
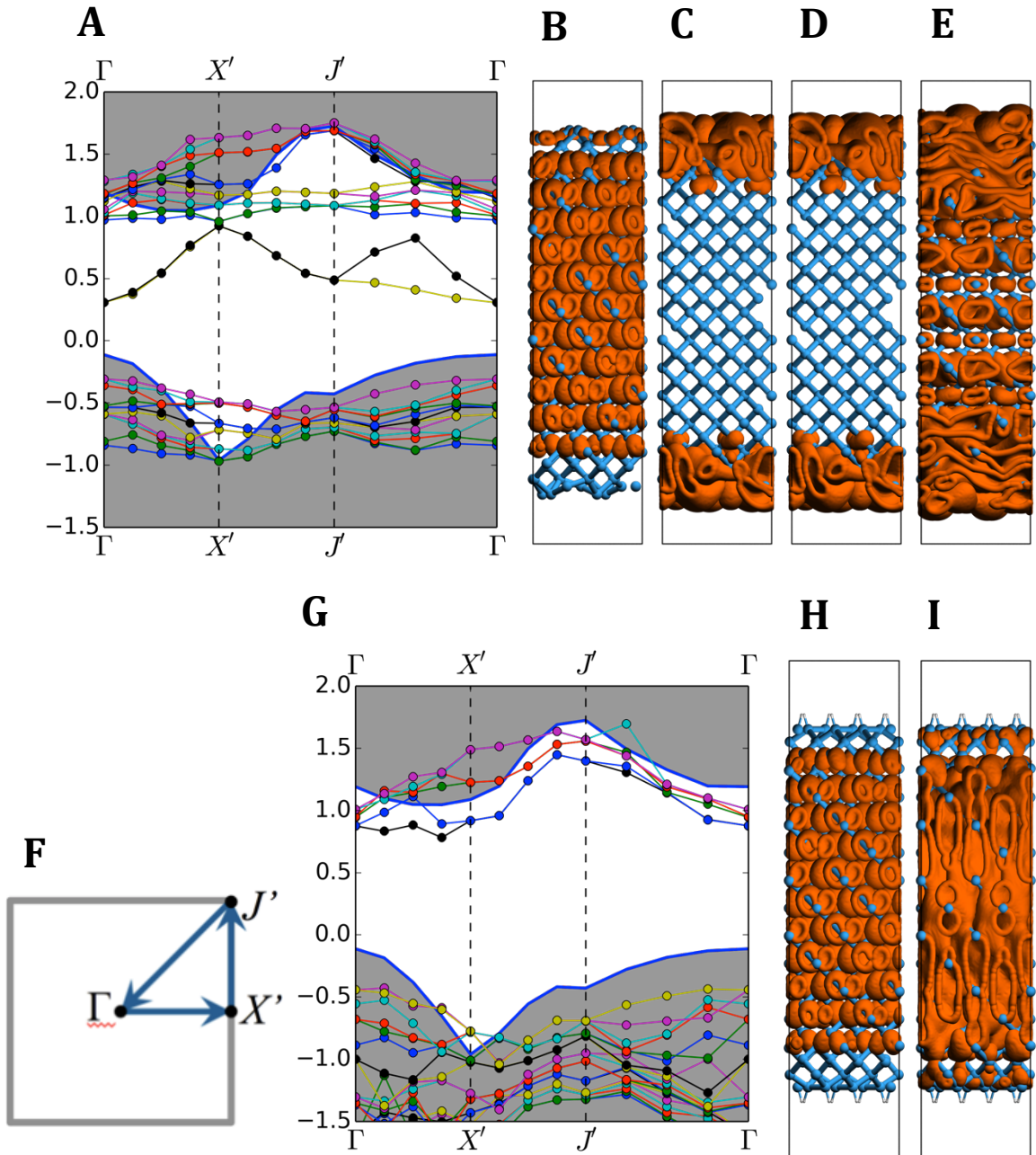
Figure 2.10. The projected band diagrams of the clean surface and the hydrogenated surface are shown in (a) and (g) respectively. At the Γ-point, the valence band, the first surface state, the second surface state, and the conduction band for the clean surface are shown in (b), (c), (d), and (e), respectively. Also At the Γ-point, the valence band and the conduction band for the hydrogenated surface are shown in (h) and (i), respectively. (f) shows the band diagram path through the Brilliouin zone use in (a) and (g).

For the pentacene functionalized surfaces, we found that the pentacene molecule adsorbed to the clean surface in the A-1 sub-type single symmetric dimer of Choudhary et al.[43] Meanwhile on the hydrogenated surface, the molecule remained flat and aligned with the dimer ridge. Both surfaces can be seen in Figure2.11.
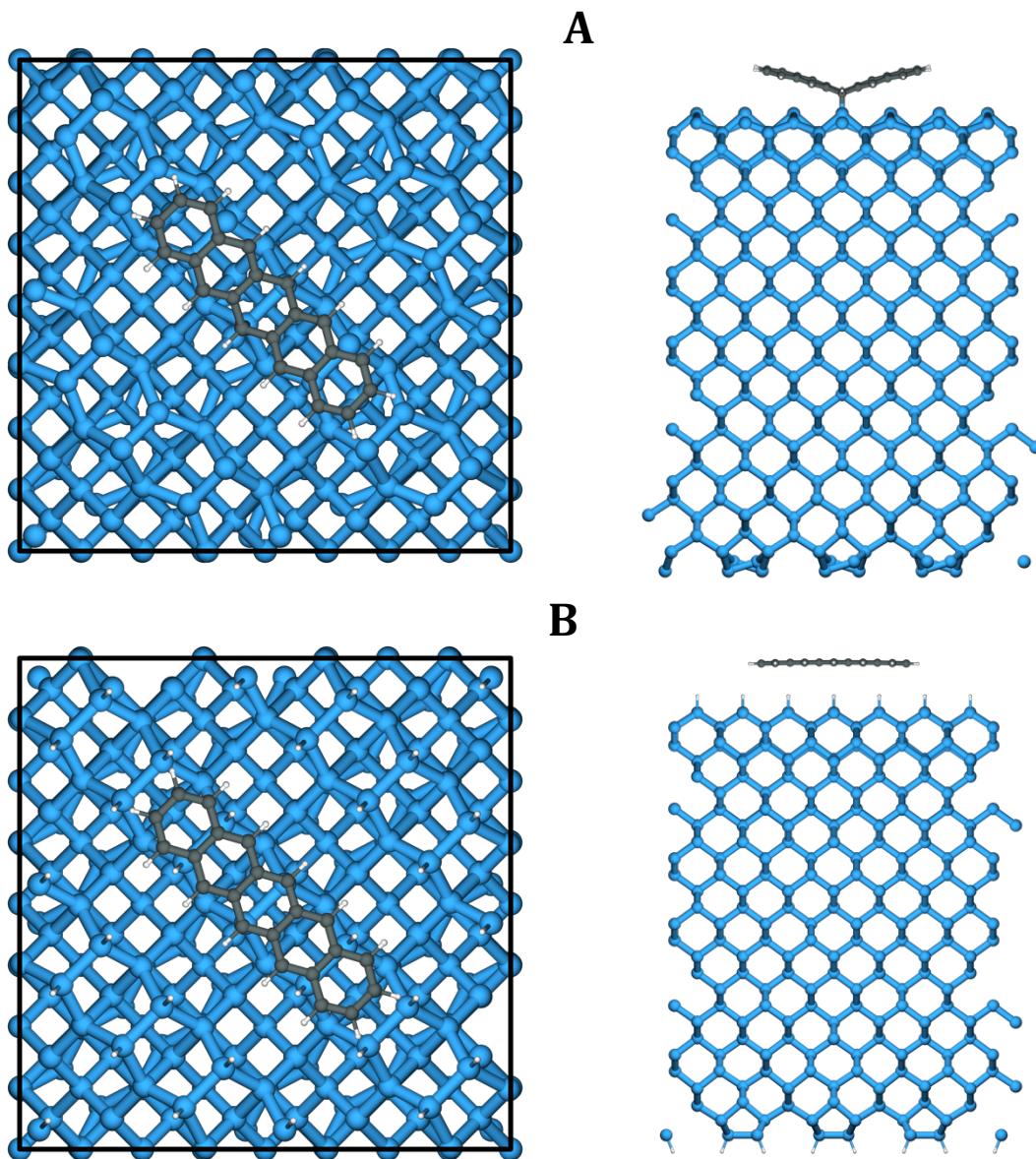
Figure 2.11. Pentacene adsorbed to a pristine (a) and a hydrogenated (b) Si (111) surface. In the latter case, the pentacene remains unreacted.

The electronic structures of the two surfaces are very different. The hydrogenized surface displays essentially independent electronic states between the silicon slab and pentacene molecule. The highest filled state (HFS) is simply the HOMO for pentacene molecule essentially unperturbed from the isolated molecule. The second highest filled state (HFS-1) is the valence band of the silicon slab. The lowest unoccupied state (LUS) is the conduction band of silicon. The HFS/LUS gap was found to be 1.256 eV. The state corresponding to the LUMO of the pentacene molecule is 478 meV above the LUS. These states are shown below with their corresponding DOS in Figure2.12.
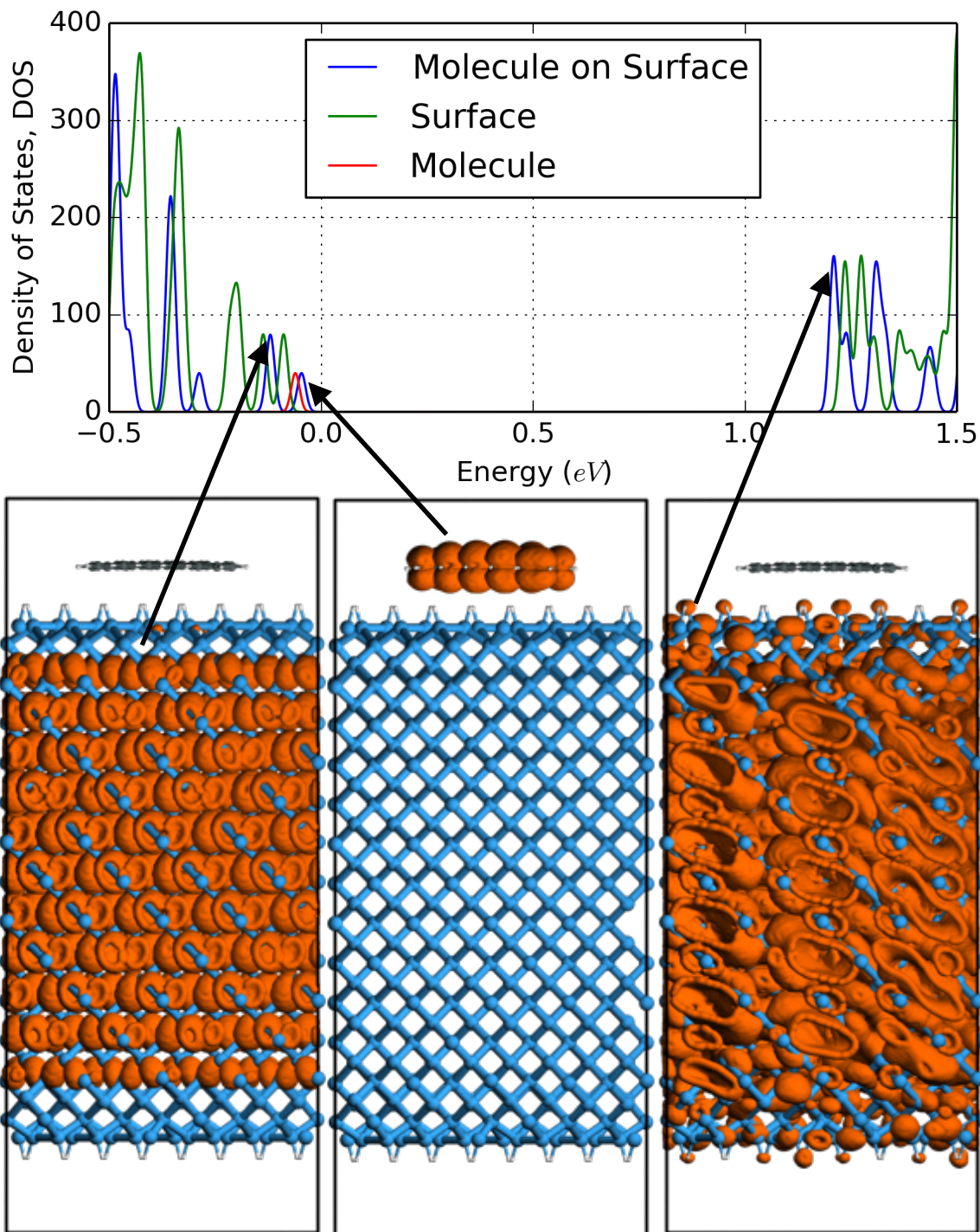
Figure 2.12. On top, the DOS of the hydrogenated surface with the pentacene molecule. From the left to right on the bottom, the HFS-1, HFS, and LUS which for an isolated surface correspond to the valence band of silicon, the HOMO of pentacene and the conduction band of silicon, respectively.

For the molecule on the clean surface, the reaction between the two completely changes the nature of the silicon surface states and the MOs of the pentacene molecule. The HFS now resides on the distorted pentacene molecule and penetrates into the surface. In fact, HFS-6 was the highest state with obvious distortion in relation to the pentacene molecule. These can be seen in the DOS shown in Figure 2.13. In the other direction, the LUS is the relatively undisturbed surface state on the opposing side of the silicon slab. The LUS+1 has a similar mixing of surface state and MO as the HFS. The lower unoccupied states all resided at the surfaces and the lowest state, residing mostly in the bulk of slab, was LUS+5. The HFS/LUS gap was found to be 0.668 eV and the HFS/LUS+1 gap was found to be 0.606 eV. This gap represents the interface transitions better since both states actually reside there.
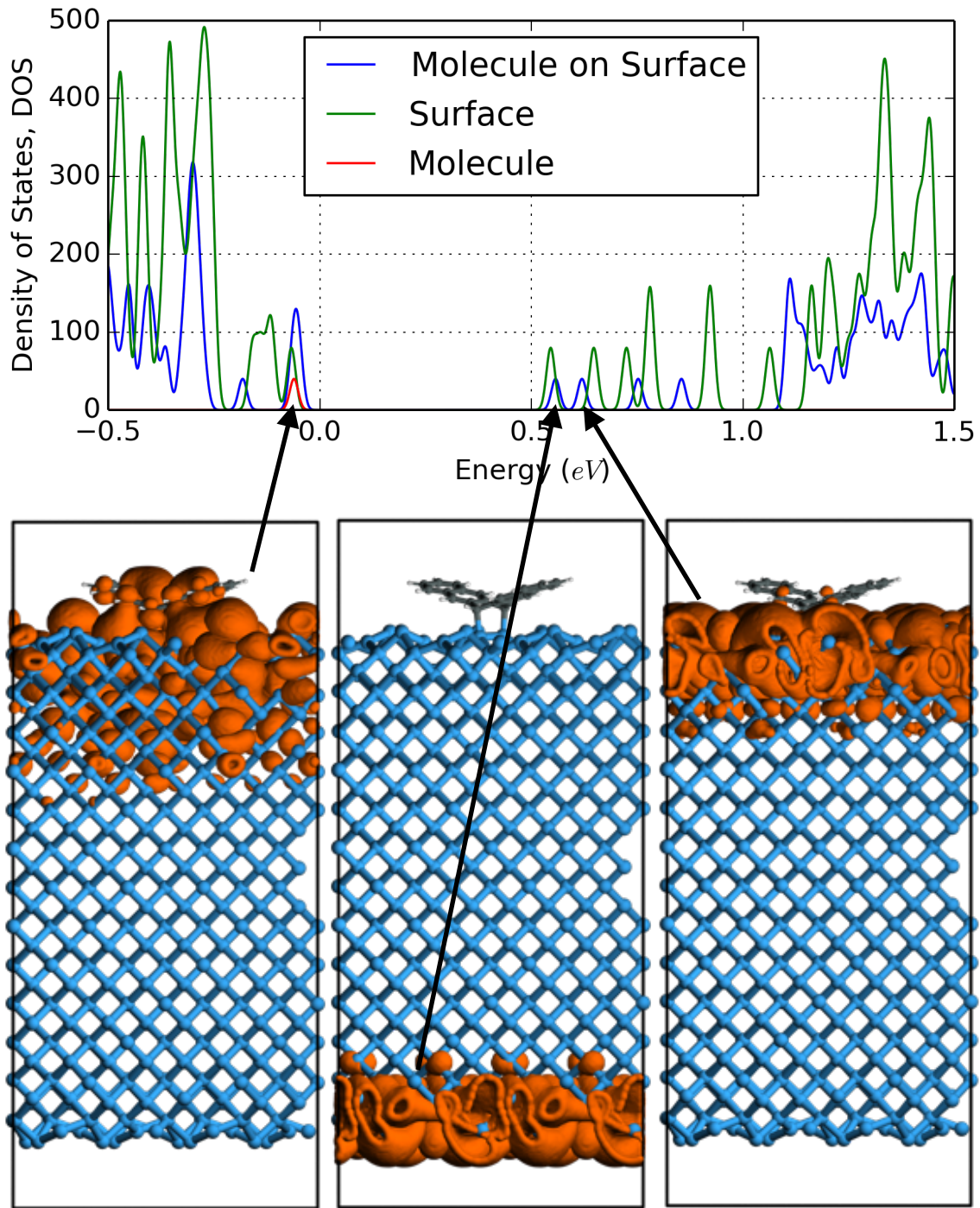
Figure 2.13. On top, the silicon surface with and without the molecule have very different DOS due to the states formed by the reaction of the molecule with the surface. From left to right on the bottom, the HFS, LUS, and LUS+1 are shown.

The calculation of the polaron pair binding energies using the semi-classical formulas present in Section 2.2 requires some approximation. For the hydrogenated surface, a surface height in the z-direction had to be defined to allow the use the carrier-interface potential. The mean height of the hydrogen atoms on the surface is chosen for this because it also corresponds very closely to the height where the valence electron density decreases to half the bulk value. Any part of the states of interest that extended beyond this height is truncated because the carrier-interface potential is ill-defined for crossing the interface. [39] The truncation of the HFS and LUS across the interface was less than 0.005% of the total states. For the unhydrogenized interface, the centroids of the HFS and LUS+1 are both well inside the silicon and significantly distributed across the interface, which makes the carrier-interface potential completely inapplicable. The Coulomb integral, while it can be calculated, it is not as applicable when the states are mixing across the interface. Nonetheless, we present the values for the unhydrogenized interface. The Renshaw model treats the coulomb interaction between the electron and hole using an electron distance from the interface that is the bulk exciton radius obtained from Equation 2.0 and a hole distance from the interface that is computed from the molecular geometry.[2] We find this gives reasonable values coulomb interaction. However, the unaccounted self-polarization contribution is significant for hybrid structures and cannot be ignored.

Table 2.4. The contributions to the total polaron pair binding energy are given for the hydrogenized and unhydrogenized surfaces with the estimate from the Renshaw model.

Energies (meV)	Clean	Hydrogenated
Self-Polarization Energy	N/A	194
Coulomb Integral	201	87
Total polaron pair binding energy	201*	281
Renshaw Model [2]	53	53

2.7 Conclusions

We have attempted a more rigorous calculation of the electrostatic effects of interfaces on carriers, excitons, and polaron pairs. By taking a semi-classical approach, we aimed to correct small scale *ab initio* simulations for being part of a larger system. In doing so, we found that for small molecule organic semiconductors, thermal motion likely has an insignificant effect on the Coulomb interaction of a polaron pair. We have also found that Coulomb integrals are more reliable than charge centers for calculating the Coulombic contribution to the polaron pair binding energy, especially if the hole and electron wave functions start to overlap. Proper surface termination is well known to be critical to predictable electronic properties of interfaces. Our work underscores this fact, as the electronic properties of unhydrogenated interfaces were significantly different both without the pentacene molecule and with it present, the chemical reaction of pentacene and silicon created completely new electronic states. The new electronic states defied the reasonable application of our semi-classical models for polaron pair binding energy. However with good surface termination, hybrid polaron pair binding energies calculated with the methods here should be reasonably accurate. If these static models of polaron pair binding prove sufficient in most cases, then a clear path exists toward creating better kinetic models.

2.8 Appendices

Appendix 2.1 The Coulomb Interaction of spherically symmetric co-centered Gaussian electron and hole distributions

A Gaussian electron charge density of net charge q_e is defined by:

$$\rho_e(r) = \frac{q_e}{\sigma_e^3 \sqrt{2\pi}^3} e^{-\frac{1}{2}\left(\frac{r}{\sigma_e}\right)^2}$$

$$\int \rho_e(r) d^3\mathbf{r} = q_e$$

The potential field:

$$\phi_e(r) = \frac{1}{4\pi\varepsilon} \frac{q_e}{r} \operatorname{erf}\left(\frac{r}{\sqrt{2}\sigma_e}\right)$$

Satisfies the Poisson equation:

$$\nabla^2 \phi_e = -\frac{\rho_e(r)}{\epsilon}$$

So a hole's charge density is:

$$\rho_h(r) = \frac{q_h}{\sigma_h^3 \sqrt{2\pi}^3} e^{-\frac{1}{2}\left(\frac{r}{\sigma_h}\right)^2}$$

The electrostatic energy is:

$$U = \int \rho_h(r)\phi_e(r) d^3\mathbf{r}$$

$$U = \int_0^\infty \rho_h(r)\phi_e(r)4\pi r^2 dr$$

$$U = \int_0^\infty \left(\frac{q_h}{\sigma_h^3 \sqrt{2\pi}^3} e^{-\frac{1}{2}\left(\frac{r}{\sigma_h}\right)^2} \right) \left(\frac{1}{4\pi\varepsilon} \frac{q_e}{r} \operatorname{erf}\left(\frac{r}{\sqrt{2}\sigma_e}\right) \right) 4\pi r^2 dr$$

$$U = \int_0^\infty \left(\frac{q_h}{\sigma_h^3 \sqrt{2\pi}^3} e^{-\frac{1}{2}\left(\frac{r}{\sigma_h}\right)^2} \right) \left(\frac{q_e}{\varepsilon} \operatorname{erf}\left(\frac{r}{\sqrt{2}\sigma_e}\right) \right) r dr$$

$$U = \frac{q_e q_h}{\varepsilon\sigma_h^3 \sqrt{2\pi}^3} \int_0^\infty r e^{-\frac{1}{2}\left(\frac{r}{\sigma_h}\right)^2} \operatorname{erf}\left(\frac{r}{\sqrt{2}\sigma_e}\right) dr$$

$$U = \frac{q_e q_h}{\varepsilon\sigma_h^3 \sqrt{2\pi}^3} \sigma_h^2 \left[\frac{\sigma_h \operatorname{erf}\left(\frac{r\sqrt{\sigma_h^2+\sigma_e^2}}{\sqrt{2}\sigma_e\sigma_h}\right)}{\sqrt{\sigma_h^2 + \sigma_e^2}} - e^{-\frac{1}{2}\left(\frac{r}{\sigma_h}\right)^2} \operatorname{erf}\left(\frac{r}{\sqrt{2}\sigma_e}\right) \right]_0^\infty$$

$$U = \frac{q_e q_h}{\varepsilon\sqrt{2\pi}^3} \frac{1}{\sqrt{\sigma_h^2 + \sigma_e^2}}$$

Finally:

$$U = \frac{q_e q_h}{4\pi\varepsilon} \frac{1}{\sqrt{\pi}\sqrt{\frac{\sigma_h^2+\sigma_e^2}{2}}}$$

Despite there being no distance between the distribution centers, there is still a finite Coulomb interaction unlike with point particles.

Appendix 2.2 Classical Electrostatics of Interfaces

2.2.1 Electrostatic potential and bound charge of a carrier near an interface

For this configuration, we define the interface as the x-y plane and positive z direction
pointing into material 1. The solution for the electrostatic potential and bound interface
charge density are adapted from Jackson's image charge analysis.[45] The electrostatic
potential ϕ^1 of q_1 is split into two parts: the potential in material 1, ϕ_1^1 and the potential in
material 2, ϕ_2^1.

$$\phi^1(\vec{r}) = \begin{cases} \phi_1^1(\vec{r}), z > 0 \\ \phi_2^1(\vec{r}), z < 0 \end{cases}$$

$$\phi_1^1(\vec{r}) = \frac{q_1}{4\pi\epsilon_1}\left[\frac{1}{|\vec{r}-\vec{r}_1|} + \frac{\alpha_1}{|\vec{r}-\vec{r}_1'|}\right] \alpha_1 = \frac{\epsilon_1 - \epsilon_2}{\epsilon_1 + \epsilon_2}$$

$$\phi_2^1(\vec{r}) = \frac{q_1}{4\pi\epsilon_2}\left[\frac{\beta_1}{|\vec{r}-\vec{r}_1|}\right]\beta_1 = \frac{2\epsilon_2}{\epsilon_1 + \epsilon_2}$$

The eletric field from charge 1 is:

$$E_1^1(\vec{r}) = \frac{q_1}{4\pi\epsilon_1}\left[\frac{\vec{r}-\vec{r}_1}{|\vec{r}-\vec{r}_1|^3} + \alpha_1\frac{\vec{r}-\vec{r}_1'}{|\vec{r}-\vec{r}_1'|^3}\right]$$

$$E_2^1(\vec{r}) = \frac{\beta_1 q_1}{4\pi\epsilon_2}\left[\frac{\vec{r}-\vec{r}_1}{|\vec{r}-\vec{r}_1|^3}\right]$$

The areal bound charge density at the interface induced by charge 1 is

$$\sigma_1 = \frac{q_1 h}{8\pi r_h^3}\left[\frac{\epsilon_0(\epsilon_1 - \epsilon_2)}{\epsilon_1(\epsilon_1 + \epsilon_2)}\right]$$

$$r_h = \sqrt{h^2 + \rho^2}$$

where h is the distance of charge 1 above the interface and ρ is a the radial distance on the
interface, e.g. $\rho = 0$ is the closest point in the interface to charge 1.

2.2.2 Carrier interaction with bound charge at interface.

The bound charge density Columbicly interacts with the charge that induced it. It's electric field is same as that of the image charge at $-\vec{r}_1{}'$.

$$E_1^{\sigma_1}(\vec{r}) = \frac{q_1\alpha_1}{4\pi\epsilon_1}\left[\frac{\vec{r} - \vec{r}_1{}'}{\left|\vec{r} - \vec{r}_1{}'\right|^3}\right]$$

Thus the electric field acting on charge 1 due to its bound interfacial charge density is:

$$E_1^{\sigma_1}(\vec{r}_1) = \frac{q_1\alpha_1}{4\pi\epsilon_1}\left[\frac{\vec{r}_1 - \vec{r}_1{}'}{\left|\vec{r}_1 - \vec{r}_1{}'\right|^3}\right]$$

The distance vector $\vec{r}_1 - \vec{r}_1{}'$ is mearly twice the distance to the interface.

$$\vec{r}_1 - \vec{r}_1{}' = 2h\hat{z}$$

$$E_1^{\sigma_1}(\vec{r}_1) = \frac{q_1\alpha_1\hat{z}}{16\pi\epsilon_1 h^2}$$

With this, we can calculate the change in the energy for charge 1 leaving from a distance h_o to the interface and traveling infinitly far into material 1 by integrating the force on charge 1.

$$\Delta U_{leave} = -\int_{h_o}^{\infty} q_1 E_1^{\sigma_1}\cdot\hat{z}dh = -\frac{q_1^2\alpha_1}{16\pi\epsilon_1 h_o}$$

Thus if $\alpha_1 > 0$, i.e. $\epsilon_1 > \epsilon_2$ then it is energetically favorible for charge 1 to leave the interface into material 1. Alternatively, if the opposite is true $\epsilon_1 < \epsilon_2$, then it will be favorable for charge 1 to move towards the interface. This result can be extended to diffuse classical charge density by means of coulumb integral of the charge desity with it's image density. However, in this context, the expecation value of this potential applied to a single

particle wave function results in a simpler relation that is more in line with a quantum mechanical approach.

$$\Delta U_{leave} = -\frac{q_1^2 \alpha_1}{16\pi\epsilon_1} \int\limits_{z>0} \frac{|\psi_1(\vec{r}_1)|^2}{z} d^3 r_1$$

2.2.3 Two Carriers Near and Interface

The interaction energy of two charges at on either side of the interface can found by the potential field of charge 1 acting on charge 2, q_2, at its position $\vec{r}_2$.

$$U_{charge-charge} = q_2 \phi_2^1(\vec{r}_2)$$

$$U_{charge-charge} = \frac{q_2}{4\pi\epsilon_2}\left[\frac{\beta_1 q_1}{|\vec{r}_2 - \vec{r}_1|}\right] = \frac{q_1 q_2}{4\pi \, (\epsilon_1 + \epsilon_2)/2}\left[\frac{1}{|\vec{r}_2 - \vec{r}_1|}\right]$$

This result is interesting in its simplicity. As long as the charges are on opposite sides of the interface, it does not matter where; the interaction is Coulombic where the permittivity is average of the two materials. This result can also be easily extended to diffuse charges on either side of the interface:

$$U_{charge-charge} = \frac{1}{4\pi \, (\epsilon_1 + \epsilon_2)/2} \int\limits_{z>0} d^3 r_1 \int\limits_{z<0} d^3 r_2 \left[\frac{\rho_1(\vec{r}_1)\rho_2(\vec{r}_2)}{|\vec{r}_2 - \vec{r}_1|}\right]$$

The charge densities of the two diffuse charges are ρ_1 and ρ_2. This the same as the expectation value of the coulomb interaction between two uncorrelated, non-exchangeable particles.

2.2.4 Polarized Interface

We can approximate a polar molecule at the interface as a pair of opposite charges on either side with the same distance. This will start with the combined potential fields in material 1 and 2.

48

$$\vec{r}_2 = \vec{r}_1{}', \quad \vec{r}_1 = \vec{r}_2{}', \quad -q_1 = q_2$$

$$\phi_1(\vec{r}) = \frac{1}{4\pi\epsilon_1}\left[\frac{q_1}{|\vec{r} - \vec{r}_1|} + \frac{\alpha_1 q_1}{|\vec{r} - \vec{r}_2|}\right] + \frac{1}{4\pi\epsilon_1}\left[\frac{\beta_2 q_2}{|\vec{r} - \vec{r}_2|}\right]$$

$$\phi_2(\vec{r}) = \frac{1}{4\pi\epsilon_2}\left[\frac{\beta_1 q_1}{|\vec{r} - \vec{r}_1|}\right] + \frac{1}{4\pi\epsilon_2}\left[\frac{q_2}{|\vec{r} - \vec{r}_2|} + \frac{\alpha_2 q_2}{|\vec{r} - \vec{r}_1|}\right]$$

which simplfy to:

$$\phi_1(\vec{r}) = \frac{q_1}{4\pi\epsilon_1}\left[\frac{1}{|\vec{r} - \vec{r}_1|} + \frac{-1}{|\vec{r} - \vec{r}_2|}\right]$$

$$\phi_2(\vec{r}) = \frac{q_1}{4\pi\epsilon_2}\left[\frac{-1}{|\vec{r} - \vec{r}_2|} + \frac{1}{|\vec{r} - \vec{r}_1|}\right]$$

These can be treated with a dipole expansion:

$$\vec{d} = \vec{r}_1 - \vec{r}_2$$

$$\vec{p} = q_1 \vec{d}$$

$$\vec{r}_d = \frac{\vec{r}_1 + \vec{r}_2}{2}$$

$$\phi_1(\vec{r}) \approx \frac{1}{4\pi\epsilon_1}\frac{\vec{p}\cdot(\vec{r} - \vec{r}_d)}{|\vec{r} - \vec{r}_d|^3}$$

$$\phi_2(\vec{r}) \approx \frac{-1}{4\pi\epsilon_2}\frac{\vec{p}\cdot(\vec{r} - \vec{r}_d)}{|\vec{r} - \vec{r}_d|^3}$$

The molecular dipole moment is $\vec{p}$ and the location of the dipole is $\vec{r}_d$.

If there is a thin sheet of these oreiented molecules at the interface due to texturing order, a net potential field is created. A diagram of this arrangement is avaible in Figure 3.12.
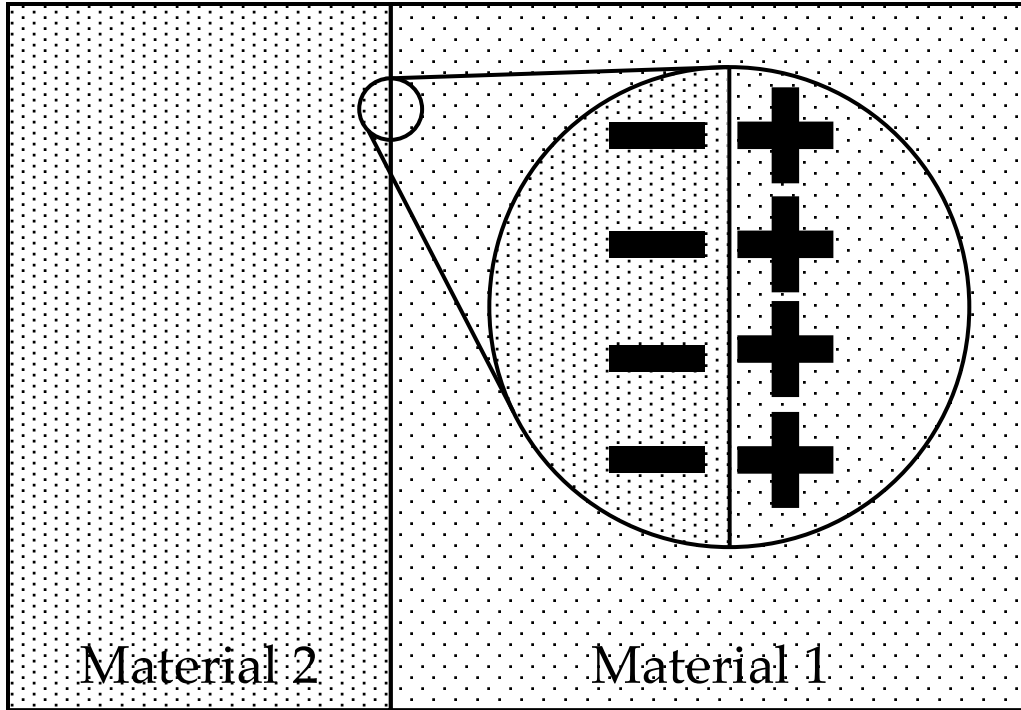
Figure 2.12. A thin layer of dipoles is arranged at the interface. They collectively act to form a potential field which is dependent on the dipole moment density.

The dipole density of this sheet in dipole moments $\vec{p}$, per area A, is given by $\vec{\sigma}$.

$$\vec{\sigma} = \frac{\vec{p}}{A}$$

The net potential field is given by integrating over interface.

$$\phi(\vec{r}) = \int \vec{g}(\vec{r} - \vec{r}_d) \cdot \vec{\sigma}(\vec{r}_d) \, d^2 r_d$$

where $\vec{r}_d$ is a position in the interface and $\vec{g}$ is the dipole field given by:

$$\vec{g}(\vec{r}) = \frac{1}{4\pi\epsilon} \frac{\vec{r}}{|\vec{r}|^3}$$

The permativity ϵ is ϵ_1 in material 1 and is ϵ_2 in material 2.

This integral can be switched to polar form for easier evaluation:

$$\rho = |\vec{r}_d|$$

$$\phi(\vec{r}) = \int\limits_{\rho=0}^{\rho=\infty} \rho d\rho \int\limits_{\theta=0}^{\theta=2\pi} d\theta \, \vec{g}(\vec{r} - \vec{r}_d) \cdot \vec{\sigma}(\vec{r}_d)$$

With a constant polarization density and substituting:

$$\phi(\vec{r}) = \frac{1}{4\pi\epsilon} \int\limits_{\rho=0}^{\rho=\infty} \rho d\rho \int\limits_{\theta=0}^{\theta=2\pi} d\theta \, \frac{1}{|\vec{r} - \vec{r}_d|^3} (\vec{r} \cdot \vec{\sigma} - \vec{r}_d \cdot \vec{\sigma})$$

There is no z component to $\vec{r}_d$ since it is just a sheet.

$$\vec{r}_d \cdot \vec{\sigma} = \rho |\vec{\sigma}| cos(\theta_\sigma - \theta)$$

where θ_σ is the angle of projection of the dipole moments onto the x-y plane.

$$\phi(\vec{r}) = \frac{1}{4\pi\epsilon} \int\limits_{\rho=0}^{\rho=\infty} \rho d\rho \left(\int\limits_{\theta=0}^{\theta=2\pi} d\theta \, \frac{\vec{r} \cdot \vec{\sigma}}{|\vec{r} - \vec{r}_d|^3} - \int\limits_{\theta=0}^{\theta=2\pi} d\theta \, \frac{\rho |\vec{\sigma}| cos(\theta_\sigma - \theta)}{|\vec{r} - \vec{r}_d|^3} \right)$$

Since our system is translationally ivarient in the x and y directions, we only need consider the z component of our position vector:

$$\vec{r} = h\hat{z}$$

$$|h\hat{z} - \vec{r}_d| \to (h^2 + \rho^2)^{\frac{1}{2}}$$

and the potential becomes:

$$\phi(h) = \frac{1}{4\pi\epsilon} \int\limits_{\rho=0}^{\rho=\infty} \rho d\rho \left(\int\limits_{\theta=0}^{\theta=2\pi} d\theta \, \frac{h\hat{z} \cdot \vec{\sigma}}{(h^2 + \rho^2)^{\frac{3}{2}}} - \int\limits_{\theta=0}^{\theta=2\pi} d\theta \, \frac{\rho |\vec{\sigma}| cos(\theta_\sigma - \theta)}{(h^2 + \rho^2)^{\frac{3}{2}}} \right)$$

the two interior integrals can be evaluted easily since the first has no dependce on θ and the second evalutes to zero. Also the only z component of $\vec{\sigma}$ maters so we can replace it

51

$$\phi(h) = \frac{1}{4\pi\epsilon} \int\limits_{\rho=0}^{\rho=\infty} \rho d\rho \ 2\pi \frac{h\hat{z} \cdot \vec{\sigma}}{(h^2 + \rho^2)^{\frac{3}{2}}} = \frac{\sigma_z}{2\epsilon} \frac{|h|}{h}$$

thus:

$$\phi_1 = \frac{\sigma_z}{2\epsilon_1}$$

$$\phi_2 = -\frac{\sigma_z}{2\epsilon_2}$$

The jump across the interface is then:

$$\Delta\phi_{2\to1} = \frac{\sigma_z}{2}\left[\frac{1}{\epsilon_1} + \frac{1}{\epsilon_2}\right]$$

$$\Delta\phi_{1\to2} = -\frac{\sigma_z}{2}\left[\frac{1}{\epsilon_1} + \frac{1}{\epsilon_2}\right]$$

If there is pair of charges across this ordered interface, the energy is then:

$$U_{inter} = \frac{\sigma_z}{2}\left[\frac{q_1}{\epsilon_1} - \frac{q_2}{\epsilon_2}\right]$$

2.9 References

1.   Giebink, N. C., B. E. Lassiter, G. P. Wiederrecht, M. R. Wasielewski, and S. R. Forrest "Ideal diode equation for organic heterojunctions. II. The role of polaron pair recombination." Phys. Rev. B 82 (15): (2010)

2.   Renshaw, C. K., and S. R. Forrest "Excited state and charge dynamics of hybrid organic/inorganic heterojunctions. I. Theory." Phys. Rev. B 90 (4): (2014)

3.   Street, R. A., M. Schoendorf, A. Roy, and J. H. Lee "Interface state recombination in organic solar cells." Physical Review B 81 (20): 205307. (2010)

4.   Onsager, L. "Deviations from Ohm's Law in Weak Electrolytes." J. Chem. Phys. 2 (9): 599. (1934)

5.   BRAUN, C. L. "ELECTRIC-FIELD ASSISTED DISSOCIATION OF CHARGE-TRANSFER STATES AS A MECHANISM OF PHOTOCARRIER PRODUCTION." J. Chem. Phys. 80 (9): 4157–4161. (1984)

6.   Wojcik, M., and M. Tachiya "Accuracies of the empirical theories of the escape probability based on Eigen model and Braun model compared with the exact extension of Onsager theory." The Journal of chemical physics 130 (10): 104107. (2009)

7.   Stein, T., L. Kronik, and R. Baer "Reliable prediction of charge transfer excitations in molecular complexes using time-dependent density functional theory." Journal of the American Chemical Society 131 (8): 2818–2820. (2009)

8.   Cho, S. W., L. F. J. Piper, A. DeMasi, A. R. H. Preston, K. E. Smith, K. V. Chauhan, P. Sullivan, R. A. Hatton, and T. S. Jones "Electronic structure of C60/phthalocyanine/ITO interfaces studied using soft x-ray spectroscopies." The Journal of Physical Chemistry C 114 (4): 1928–1933. (2010)

9.   Arkhipov, V. I., and H. Bässler "Exciton dissociation and charge photogeneration in pristine and doped conjugated polymers." physica status solidi (a) 201 (6): 1152–1187. (2004)

10.   Muntwiler, M., Q. Yang, W. A. Tisdale, and X.-Y. Zhu "Coulomb barrier for charge separation at an organic semiconductor interface." Physical review letters 101 (19): 196403. (2008)

11.   Emin, D. "Generalized adiabatic polaron hopping: Meyer-Neldel compensation and Poole-Frenkel behavior." Physical review letters 100 (16): 166602. (2008)

12.   Hartke, J. L. "The Three Dimensional Poole Frenkel Effect." Journal of Applied Physics 39 (10): 4871–4873. (1968)

13.   d'Andrea, A., and R. Del Sole "Wannier-mott excitons in semi-infinite crystals: Wave functions and normal-incidence reflectivity." Physical Review B 25 (6): 3714. (1982)

14.   Gu, S. W., and H. Sun "Excitons near interfaces of polar crystals." Physical Review B 37 (15): 8805. (1988)

15.   Sun, H., and S. W. Gu "Excitons near interfaces of polar-nonpolar crystals with strong interactions between the excitons and optical phonons." Physical Review B 38 (18): 13271. (1988)

16.   Paziuk, V. V., and M. V. Tkach "Presurface Exciton on the Media Parting Border." physica status solidi (b) 177 (2): 325–334. (1993)

17.   Viri, D., and R. Del Sole "Effect of the image potential on excitons in semi-infinite semiconductors." Physical Review B 52 (16): 11891. (1995)

18.   Thoai, D. B. T., R. Zimmermann, M. Grundmann, and D. Bimberg "Image charges in semiconductor quantum wells: Effect on exciton binding energy." Physical Review B 42 (9): 5906. (1990)

19.   Wu, S.-T., and C. Eberlein "Quantum electrodynamics of an atom in front of a non–dispersive dielectric half–space." Proceedings of the Royal Society of London. Series A: Mathematical, Physical and Engineering Sciences 455 (1987): 2487–2512. (1999)

20.   Jackson, J. D. 1962. Classical Electrodynamics. John Wiley & Sons, Inc.

21.   Xue, C., and S. Deng "Coulomb Green's function and image potential near a planar diffuse interface, revisited." Computer Physics Communications 184 (1): 51–59. (2013)

22.   Lindell, L., D. Çak r, G. Brocks, M. Fahlman, and S. Braun "Role of intrinsic molecular dipole in energy level alignment at organic interfaces." Applied physics letters 102 (22): 223301. (2013)

23.   Ma, W. "A study of flexoelectric coupling associated internal electric field and stress in thin film ferroelectrics." physica status solidi (b) 245 (4): 761–768. (2008)

24.   Lee, D., and T. W. Noh "Giant flexoelectric effect through interfacial strain relaxation." Philosophical Transactions of the Royal Society A: Mathematical, Physical and Engineering Sciences 370 (1977): 4944–4957. (2012)

25.   Karthik, J., R. V. K. Mangalam, J. C. Agar, and L. W. Martin "Large built-in electric fields due to flexoelectricity in compositionally graded ferroelectric thin films." Physical Review B 87 (2): 024111. (2013)

26.   Kieffer, H. H. A. J. "Energetically favorable SubPc molecule orientations on C60 Surfaces." In Preparation

27.   Jailaubekov, A. E., A. P. Willard, J. R. Tritsch, W.-L. Chan, N. Sai, R. Gearba, L. G. Kaake, K. J. Williams, K. Leung, P. J. Rossky, and X.-Y. Zhu "Hot charge-transfer excitons set the time limit for charge separation at donor/acceptor interfaces in organic photovoltaics." Nat Mater 12 (1): 66–73. (2013)

28.   Zhu, Z., N. Shima, and M. Tsukada "Electronic states of Si (100) reconstructed surfaces." Physical Review B 40 (17): 11868. (1989)

29.   Blöchl, P. E. "Projector augmented-wave method." Physical Review B 50 (24): 17953. (1994)

30.   Perdew, J. P., K. Burke, and M. Ernzerhof "Generalized gradient approximation made simple." Physical review letters 77 (18): 3865. (1996)

31.   Klimeš, J., D. R. Bowler, and A. Michaelides "Chemical accuracy for the van der Waals density functional." Journal of Physics: Condensed Matter 22 (2): 022201. (2010)

32.   Klimeš, J., D. R. Bowler, and A. Michaelides "Van der Waals density functionals applied to solids." Physical Review B 83 (19): 195131. (2011)

33.   Gower, J. C. "Generalized procrustes analysis." Psychometrika 40 (1): 33–51. (1975)

34.   Hanwell, M. D., D. E. Curtis, D. C. Lonie, T. Vandermeersch, E. Zurek, and G. R. Hutchison "Avogadro: an advanced semantic chemical editor, visualization, and analysis platform." Journal of cheminformatics 4 (1): 1–17. (2012)

35.   Krukau, A. V., O. A. Vydrov, A. F. Izmaylov, and G. E. Scuseria "Influence of the exchange screening parameter on the performance of screened hybrid functionals." J. Chem. Phys. 125 (22): (2006)

36.   Widom, R. M. F. A. M. "WaveTrans: Real-space wavefunctions from VASP WAVECAR file ." (2015)

37.   Feenstra, R. M., N. Srivastava, Q. Gao, M. Widom, B. Diaconescu, T. Ohta, G. L. Kellogg, J. T. Robinson, and I. V. Vlassiouk "Low-energy electron reflectivity from graphene." Physical Review B 87 (4): 041406. (2013)

38.   Kim, C. H., O. Yaghmazadeh, D. Tondelier, Y. B. Jeong, Y. Bonnassieux, and G. Horowitz "Capacitive behavior of pentacene-based diodes: Quasistatic dielectric constant and dielectric strength." J. Appl. Phys. 109 (8): 083710. (2011)

39.   Stern, F. "Image potential near a gradual interface between two dielectrics." Physical Review B 17 (12): 5009–5015. (1978)

40.   Giri, A. K., and G. B. Mitra "Extrapolated values of lattice constants of some cubic metals at absolute zero." J. Phys. D: Appl. Phys. 18 (7): L75–L78. (1985)

41.   Ng, E. J., V. A. Hong, Y. Yang, C. H. Ahn, C. L. M. Everhart, and T. W. Kenny "Temperature Dependence of the Elastic Constants of Doped Silicon." JOURNAL OF MICROELECTROMECHANICAL SYSTEMS Accepted but not yet published. (2015)

42.   O'Donnell, K. P., and X. Chen "Temperature dependence of semiconductor band gaps." Appl. Phys. Lett. 58 (25): 2924. (1991)

43.   Choudhary, D., P. Clancy, and D. R. Bowler "Adsorption of pentacene on a silicon surface." Surf. Sci. 578 (1-3): 20–26. (2005)

44.   S.E., Morris, B. D., S. M.E., H. H., W. M.J., K. J., K. J., and S. M. "Effect of axial halogen substitution on the performance of subphthalocyanine based organic photovoltaic cells." Organic Electronics 15 (12): 3660 − 3665. (2014)

45.   Jackson, J. D. 1962. Classical Electrodynamics. John Wiley & Sons, Inc.

CHAPTER 3

Predictive Simulations for Tuning Electronic and Optical Properties of SubPc Derivatives

3.0 Synopsis

Boron subphthalocyanine chloride is an electron donor material currently used in small molecule organic photovoltaics. In order to enhance the electronic and optical properties of subphthalocyanines for this application, we use first-principles calculations to investigate a series of derivatives of the boron subphthalocyanine chloride molecule where the boron and chlorine atoms are substituted with other trivalent and halogen atoms. Gas phase molecular structures and properties are predicted. Using positions and orientations of the known compounds as the starting coordinates for these molecules, stable crystalline structures are derived following a procedure that involves perturbation and energy minimization. Electronic structure and photonic properties of the predicted crystals are computed using the GW method.

3.1 Motivation and Background

Organic photovoltaics (OPV) are a promising technology for large-scale deployment of renewable energy generation. They have the advantages of being more easily processed, using less material, and being more substrate-independent than traditional inorganic PV's such as silicon.[1] Of the OPV materials, there are two types: polymeric and molecular. Of the molecular OPV materials, a group of macrocyclic compounds known as phthalocyanines

have been found to be good absorbers/electron donors. Boron subphthalocyanine chloride, a related material, has been shown to offer improved efficiency.[2] As opposed to the typically planar geometry of phthalocyanines consisting of four fused diiminoisoindole rings, boron subphthalocyanine chloride adopts an inverted umbrella shape with only three fused diiminoisoindole rings. The boron subphthalocyanine chloride molecular structure is shown in Figure 3.1.
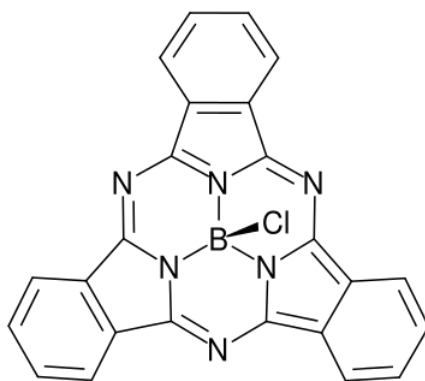
Figure 3.1. The structure of the most commonly known subphthalocyanine, boron subphthalocyanine chloride is shown.

The goal of this work is to use *ab intio* methods to computationally evaluate and identify useful trends in derivatives of boron phthalocyanine chloride where the boron and chlorine atoms have been substituted for other trivalent elements and halogen atoms, respectively. The trivalent site elements explored in this work were boron, aluminum, gallium, indium, scandium, and yttrium. The halogen site elements used in this work were fluorine, chlorine, bromine, and iodine. Thus, a total of twenty-four molecules were examined in our simulation matrix. For the remainder of this paper, to designate a subphtalocyanine with a given pairing of trivalent element T and halogen element X, we use the abbreviation T-X. For example, B-Cl refers to the commonly described boron subphthalocyanine chloride. Of the molecules explored here, the B-F, B-Cl, and B-Br molecules have been observed experimentally and their crystal structures are known.[3, 4] In order to evaluate these concept molecules as OPV materials, the structure, as well as several electrical and optical

properties, have been calculated for each molecule in the gas phase and then in their predicted crystal structures.

Most of the molecules simulated in this work have not been synthesized or are difficult to synthesize,[3] Therefore, by identifying the most promising candidates for a given application via the simulation-based predictive evaluation of molecular concepts, we hope to facilitate on-target materials selection and provide motivation for the development of the necessary synthesis routes.

The B-Cl molecule is used to validate our electronic and optical properties calculations since its properties are known experimentally. The B-Cl material is a purple compound with an optical bandgap of $2.0 - 2.1$ eV. [2, 3, 5] The molecule has non-linear optical properties that have been of some interest to researchers in that field.[6]

The crystal structures of the B-F, B-Cl, and B-Br derivatives have been found using X-ray diffraction to be orthorhombic of space group *Pnma*, with each unit cell containing four molecules.[4, 7] All molecules have the shape of an inverted umbrella with a molecular dipole pointing from the electronegative halogen towards trivalent site. In the crystal structure, there is no net polarization due to the alternating arrangement of molecular dipoles. The B-Cl unit cell configuration is shown in Figure 3.2.
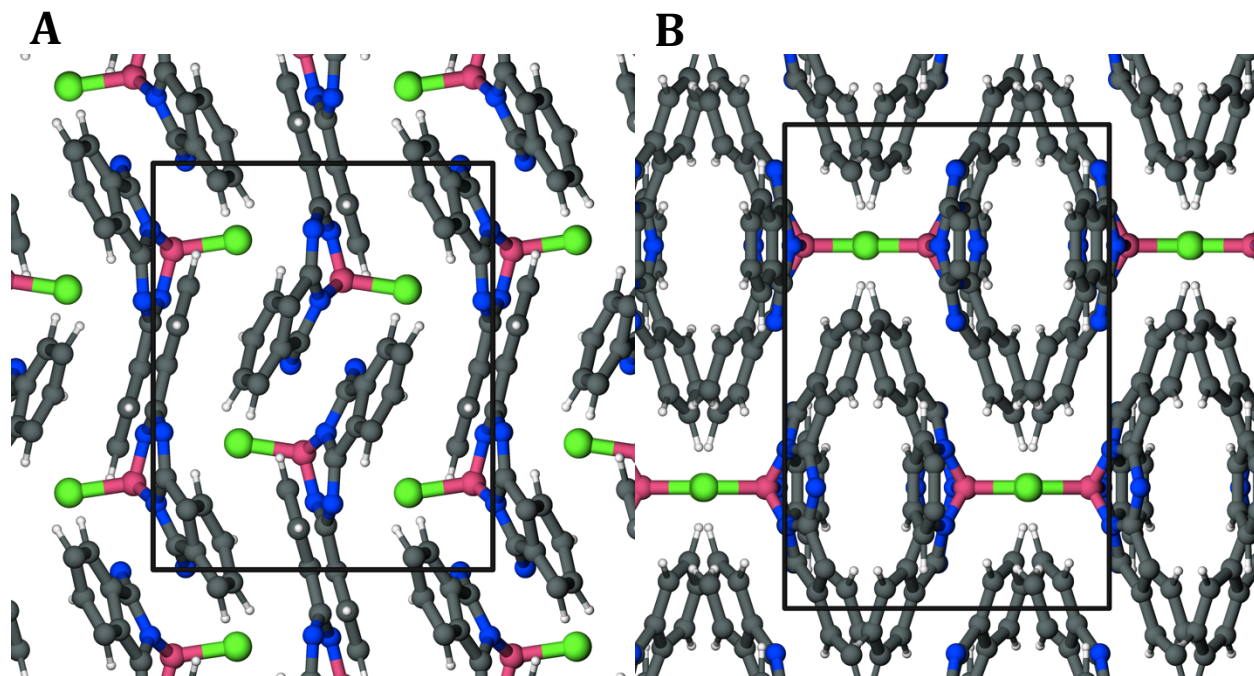
Figure 3.2. The B-Cl unit cell viewed along the *c* direction (left) and *b* direction (right) rendered from Ref. [7]. In both renderings, the *a* direction is horizontal.

3.2 Properties of Interest

For the gas-phase molecules, the relaxed geometry is used to compute the HOMO/LUMO relative to the vacuum level. These are central properties in organic electronic device design.[8] The molecular dipole moments were also calculated from the relaxed geometry. The dipole moment of a molecule can play a significant role in electronic properties of interfaces. [9]

For the crystal structures of the molecules, we are faced with the reality that crystal structure prediction is a difficult and outstanding problem in solid-state physics and materials science.[10, 11] Considering that the geometries of the relaxed isolated molecules do not differ from each other very much, we opted to pursue a procedure in which the new structures are obtained via energy relaxation by using the known structures of other family members as the starting configuration. This method is described in more detail in the methodology section.

Once possible crystal structures are found, the property of greatest interest is the electronic band structure and, in conjunction, the band gap. The complex permittivity and complex refractive indices have previously been calculated in literature, since researchers in the OPV field commonly employ these for optical modeling of devices.[12] The static permittivity has also been calculated using the long wavelength limit of the complex permittivity. The static permittivity is often used in modeling exciton dissociation energy via a simple Coulombic formula such as[8]

$$E_{e+h} = \frac{q^2}{4\pi\epsilon_o\epsilon_r R_{e+h}}.$$

3.3 Computational Methodology

To obtain the isolated molecular geometry, molecules are created and relaxed using the program Avogadro with its built-in empirical classical potentials.[13] This is done to save computational effort in the more intensive DFT computation. The final molecular geometry of isolated molecules is computed via relaxation using Gaussian 09 (Rev. C). The exchange-correlation functional employed is B3LYP, which is a variation of the hybrid functional created by Becke.[14] The B3LYP hybrid functional utilizes a linear combination of the correlation functionals from VWN[15] and LYP[16]. The basis set used for molecules with atoms below atomic number 36 is 6-31G(d) from Ref.[17]. For molecules containing species with higher atomic number, the DGDZVP basis set is used.[18, 19] The dipole moments of the molecules are calculated from the volume integrals of the electron density.

Calculations of crystals of the SubPc's were done using VASP (version 5.3.3). These calculations employ the PAW method [20] with the PBE exchange-correlation functional,[21] where augmented plane waves form the basis set and van der Waals interactions are accounted for using the VdW-DFT method developed in Ref.[22, 23] with removed PBE correlation correction.

For relaxations of the crystal structure, the electronic component is accomplished using the Kosugi algorithm.[24] A maximum energy difference between iterations of 0.01 meV served as the convergence criterion. Partial occupancies are determined with a Gaussian smearing width of 0.1 eV. The cutoff energy for the plane wave basis set is 400 eV. The number of Fourier space grid points used is twice as many as needed to equate to the energy cutoff wave vector.

3.4 Crystal Structure Prediction

There are several codes that are designed to find the lowest energy crystal structure such as USPEX, CALYPSO, XtalOpt, and Polymorph/GULP. The state of the art of crystal structure prediction based on these codes allows for ~100 atoms per unit cell.[25] Subphthalocyanines are relatively large molecules with 44 atoms each and the known structures contain four molecules per unit cell. Hence, using any crystal structure prediction codes was impractical. Instead, we devised a sequence of procedures involving manipulation of atomic positions and structural relaxation, based on the assumption that the new derivatives conceived here have crystals structures similar to those of the three known crystal structures, and that achieving the same results via different structural progression pathways provides additional validation of the predicted structure. Moreover, simple substitution and relaxation does not necessarily result in the lowest energy state structure. Of all the approaches we explored, the following three treatments produced the lowest energy structures:

In a first treatment, we simply substitute elements in the known B-Cl crystal structure. The structures and their corresponding unit cells are relaxed while maintaining their space group symmetry. The relaxed structures are then relaxed again without symmetry conservation. As a simple means of perturbing the structures, the unit cells and molecules inside are dilated by 10% in each lattice direction and then allowed to relax again. In the second and third treatments, elements are replaced in the isolated B-Cl molecules with known structure

and the isolated derivative molecules are relaxed before they are assembled into a crystalline configuration. During the assembly procedure the trivalent atom in the derivatives is positioned on the boron location of the known B-Cl crystal structure and the relaxed gas-phase molecules are rotated about their trivalent site so that their halogen bonds and nitrogen bonds are aligned with the corresponding bonds in the known B-Cl crystal structure. From this point, in the second treatment the unit cell and molecular positions are expanded independently along each lattice direction by small increments. Upon each incremental expansion, a single point energy calculation is performed to determine the energy associated with this configuration. The procedure is repeated until the energy minima in each independent crystallographic direction are clearly identified. The corresponding unit cell vector dilations were then applied to the original structure and it is allowed to relax. The third treatment is essentially the same as the second with the exception that the molecules themselves are not dilated with the unit cell. The purpose of these procedures is to systematically perturb the crystal unit cells after elemental substitutions and to provide for different relaxation pathways and to verify that the equilibrium structures are reached in each case.

3.5 Electronic Structure Calculations

Standard DFT calculations fail to reproduce an electronic band gap even as large as the known optical band gap in B-Cl. This under-prediction is a well-known weakness of DFT. To remedy this, the GW approximation is used. The complex dielectric function is computed using the method in Ref.[26]. The Bethe-Salpeter equation (BSE) is used to calculate the complex dielectric function of the materials in order to account for excitonic effects.[27]

For the GW calculations, the recommended GW PAW pseudo-potentials included with VASP is used with a cut off energy of 300 eV. The Gaussian energy smearing is set to a width of 0.05 eV. GW response functions are truncated to 100 eV since increasing this cut-

off had no effect. 1216 bands with 50 frequency points are included in the calculation. Increasing the number of total bands considered does not affect the predicted extinction coefficient. A grid of 2x2x2 k-points is used in the reduced Brillouin zone since larger grids are computationally intractable.

BSE calculations are carried out with 256 frequency points, and the GW response functions are truncated at the same value as the in the previous GW calculations. 100 occupied and unoccupied states are considered for the calculation. The complex shift in the Kramers-Kronig transformation for determining the dielectric function is set to 0.03 eV

3.6 Gas Phase Results

After structural relaxation, all of the proposed subphthalocyanine derivatives retain the 3-fold symmetric inverted umbrella structure. The degree of openness of the umbrella structures canopy varies between the proposed derivatives. To quantify this openness, the angle between the nearest nitrogen atom, the trivalent atom, and the halogen is computed. This nitrogen-trivalent-halogen (NTX) angle depends almost entirely on the size of the trivalent atom as seen in Figure 3.3. This degree of openness may be useful for conformation or epitaxy to substrates.
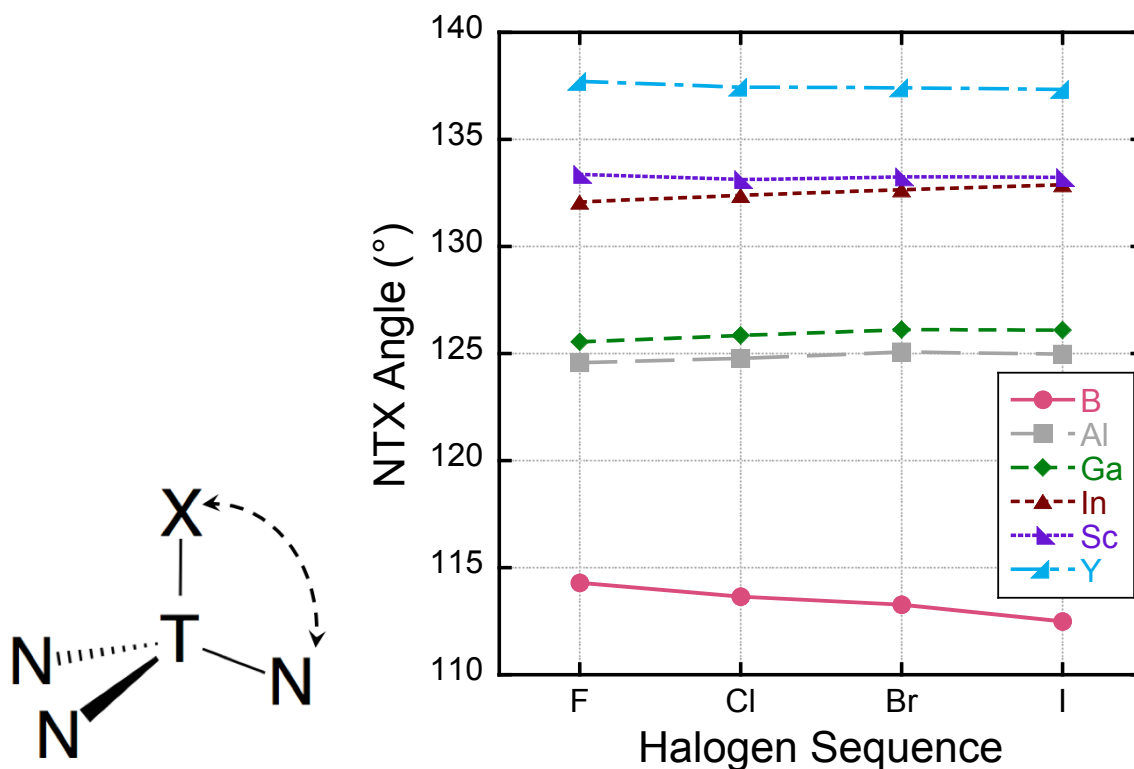
Figure 3.3. In the plot of the nitrogen-trivalent-halogen angle above, the angle is mostly unchanged by halogen substitution depending much more strongly on the identity of the trivalent atom.

The molecular dipole moments of the proposed subphthalocyanine derivatives are found to vary widely from 1 ~ 6 D. All of the dipole moments are axial pointing in the direction from the halogen atom to the trivalent atom. No simple model or trends could be found to predict the variations in the molecular dipole moments as seen in Figure 3.4. Using electronegativity or the Mulliken charges and structure does not describe the dipole moments found. Despite the lack of a model for describing the trends found, the range of dipole moments allows for a new experimental parameter to be exploited.
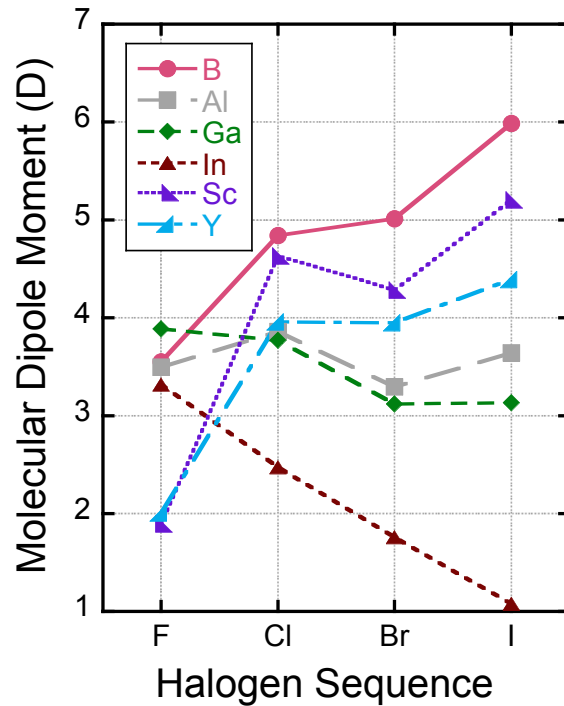
Figure 3.4. The proposed molecules yielded a wide range of molecular dipole moments despite having no obvious trends.

The HOMO and LUMO levels are not strongly affected by the substitution of either halogen or trivalent species. We attribute this to the spatial distribution of the HOMO and LUMO, which are almost entirely located on the diiminoisoindole rings. This is visualized with the B-F molecule in Figure 3.5a. One rudimentary trend that can be observed is that with higher atomic number substitution the HOMO/LUMO gap decreases, which can be seen in Figure 3.5b.
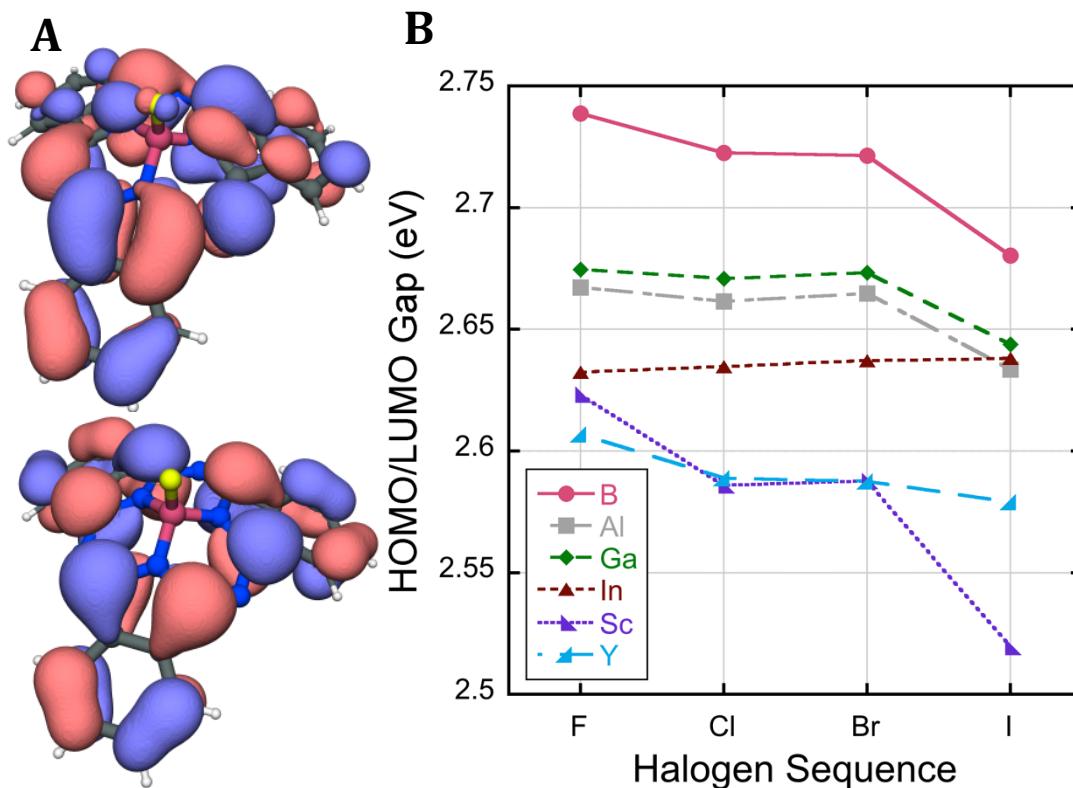
Figure 3.5. (a) The HOMO and LUMO are shown (LUMO on top) as isodensity surfaces containing 80% of each state. The blue/pink coloring indicates positive/negative values of the wave function. (b) The HOMO/LUMO difference is shown versus the halogen sequence.

3.7 Crystal Structure Results

The crystal structures determined for the concept molecules match experiment well for the known molecules B-F, B-Cl, and B-Br. The largest lattice parameter error is $\approx 4.5\%$. All of the crystal structures found are orthorhombic of the space group *Pnma*. Interestingly, the equilibrium structures of the scandium derivatives no longer have axial halogen atoms. Instead, the halogen atoms are displaced towards the second nearest scandium atom. This is apparent in Figure 3.6, where the Al-Cl and Sc-Cl structures are rendered side by side. Unfortunately, the crystals containing yttrium and indium derivatives are not stable when subject to systematic perturbations used to find the minimum energy structures. This may simply indicate that these molecules form different crystalline structures that cannot be accessed using the above procedure, which implicitly lends credibility to our approach in

66

that it shows selectivity. The lattice parameters for all the proposed crystal structures are available in Table 3.1.
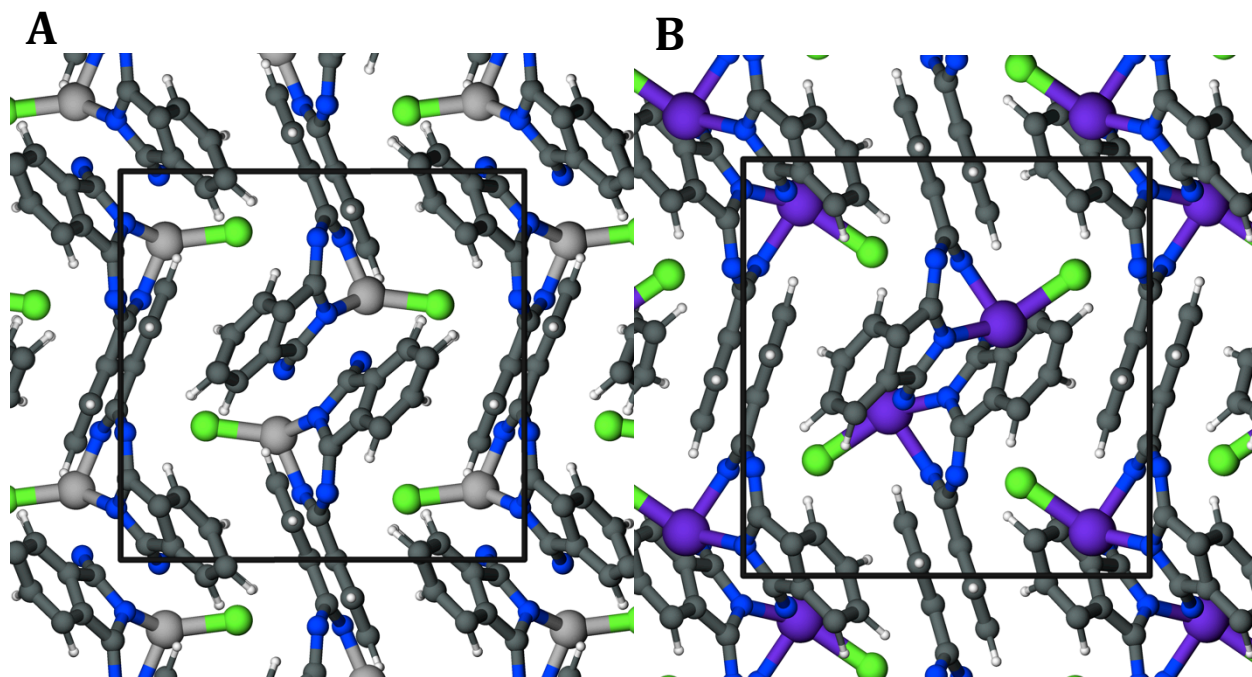
Figure 3.6. (a) The Al-Cl crystal has axial halogen atoms whereas (b) the Sc-Cl crystal does not. All of the scandium derivatives have halogens are tilted towards the second neighboring scandium atom. Both unit cells are viewed such that the *a*, *b*, and *c* lattice directions are horizontal, vertical, and into the page respectively.

Table 3.1. The predicted lattice parameters of the subphthalocyanine derivatives. The percentage deviations from experiments are shown in parenthesis if available.[32]

Molecule	a Lattice Parameter (Å)	b Lattice Parameter (Å)	c Lattice Parameter (Å)
B-F	9.8609 (-4.5 %)	11.9603 (-1.2 %)	14.4059 (0.6 %)
B-Cl	9.9991 (-3.7 %)	11.9465 (-1.5 %)	14.8851 (0.4 %)
B-Br	10.1315 (-2.6 %)	11.9319 (-0.7 %)	15.1059 (0.3 %)
B-I	10.3203	11.8903	15.5287
Al-F	11.1761	11.5943	14.1377
Al-Cl	11.6901	11.2454	14.6624
Al-Br	11.8680	11.2251	14.8772
Al-I	11.8554	11.2113	15.3509
Ga-F	11.5458	11.4904	13.9705
Ga-Cl	12.0337	11.1450	14.4848
Ga-Br	11.8222	11.5221	14.7211
Ga-I	11.8946	11.6867	15.0485
Sc-F	10.9861	11.5415	13.5916
Sc-Cl	11.2909	11.5687	14.0733
Sc-Br	11.1962	11.6360	14.3676
Sc-I	11.1179	11.3186	14.6759

The GW method electronic structure calculations are limited by computational resources. However, band structure calculations without GW on the B-Cl crystal show that conduction band and valence band edges are relatively flat across the reduced Brillouin zone, with extrema at the high symmetry k-points. The same behaviors are reflected in the band diagrams computed using the GW method, as can be seen in the side-by-side comparison of Figure 3.7. For this reason, we believe that the band gaps found via the GW method are well converged despite the low number of k-points used. The electronic band gaps found all range from 2.25 ~ 2.61 eV and mostly increase with the substitution of each heavier halogen atom.
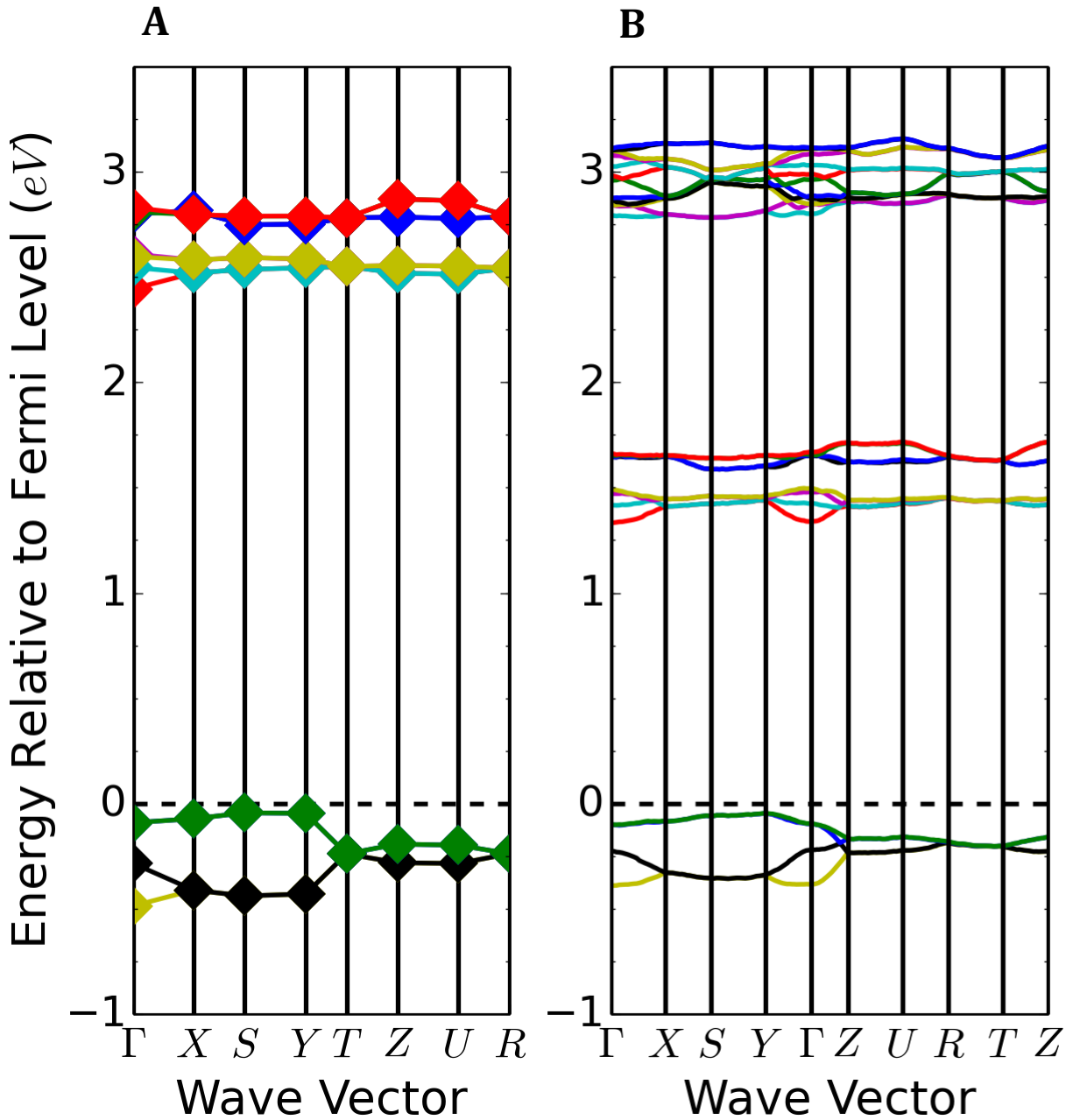
Figure 3.7. Two band diagrams for the B-Cl crystal. (a)The band diagram calculated using the standard DFT yields an electric band gap smaller than the optical gap. (b) a sparse band diagram calculated using the more costly GW method yields a more realistic electronic band gap. Different bands are assigned different colors to guide the eye.

The complex anisotropic permittivities computed for each crystal and all are found to have highly anisotropic dissipation. This is not unexpected considering that the similar

compound, copper phthalocyanine, exhibits anisotropic permittivity relative to the molecular stacking direction.[28, 29] For the materials explored here, relatively little complex permittivity is found in the *a*-direction. Unfortunately, not a single crystal optical properties measurements could be found in literature for comparison, only data for amorphous and nanocrystalline materials. Further complicating the problem, it is known that the local molecular environment can affect the absorption spectra.[30] In order to reconcile the calculations performed for anisotropic structures with measurements done on isotropic materials, the anisotropic permittivity is averaged. To this end, the complex refractive index is then taken as the square root of the averaged complex anisotropic permittivity. Figure 3.8 shows the directionally averaged extinction coefficient, along with those for each lattice direction and that measured for an amorphous film of the B-Cl derivative. Notice the extra peaks between 400~485 nm, which also occur in the other boron derivatives. These may be physical but only observable in single crystals or they are an artifact of the BSE method and/or the limited number of k-points used. Either way, the optical band gap absorption peak position aligns well with experiment with a difference of 75 meV for B-Cl and 91 meV for B-F.[31] When compared to the work of Fulford *et al.*, whom has measure the extinction coefficient of B-Cl dissolved in toluene, the differences are small. The maximum difference between B-Cl, B-F, and B-Br is 31 meV.[4] These results are a tabulated in Table 3.2.Due to the averaging of the complex anisotropic permittivity, the extinction coefficient magnitudes and the optical band gap are only accurate to first order, but nonetheless presented in Table 3.2.

Table 3.2. The first peak of the extinction coefficients indicating the optical band gap are listed for the subphthalocyanine derivatives. Experimental values are given in parentheses.

Molecule	Optical Band Gap (nm)	Electronic Band Gap (eV)	Exciton Dissociation Energy (eV)
B-F	559 (583)[31] (562)[4]	2.50	0.28
B-Cl	565 (585)[31] (565)[4] (587)[33]	2.49	0.29
B-Br	558 (566)[4]	2.51	0.29
B-I	554	2.58	0.34
Al-F	567	2.52	0.34
Al-Cl	550	2.54	0.29
Al-Br	543	2.56	0.28
Al-I	549	2.56	0.30
Ga-F	571	2.47	0.30
Ga-Cl	580	2.52	0.38
Ga-Br	546	2.56	0.29
Ga-I	540	2.61	0.31
Sc-F	621	2.24	0.25
Sc-Cl	566	2.37	0.18
Sc-Br	546	2.47	0.20
Sc-I	552	2.50	0.25
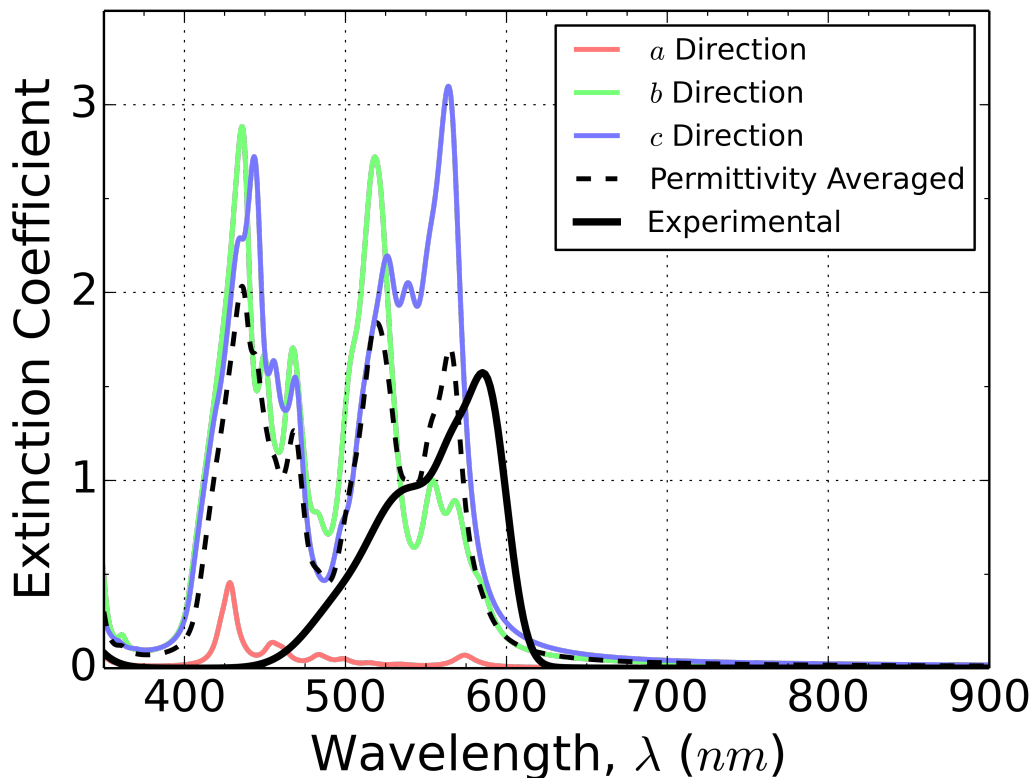
Figure 3.8. The extinction coefficient for each direction is plotted with directionally averaged extinction coefficient and the experimental extinction coefficient for B-Cl from Ref. [31]. Despite the conjectural nature of this comparison, the optical band gap is well matched and the optical band gap extinction coefficients can be compared between the proposed derivatives.

The static permittivity is also computed as part of the BSE calculations at the long wavelength limit. As mentioned above, the static permittivity is related to the exciton dissociation energy, which is important for device performance. In the proposed derivatives, the static permittivity is found to generally decrease with heavier halogen atoms, which can be seen in Figure 3.9. We suspect this is due to the larger halogen atoms introducing more free volume into the unit cells which lowers the permittivity despite larger halogen atoms having a larger atomic polarizability. The authors have yet to find static permittivity measurements of any of the proposed derivatives for validation. However the values presented here can still be used for relative comparisons.
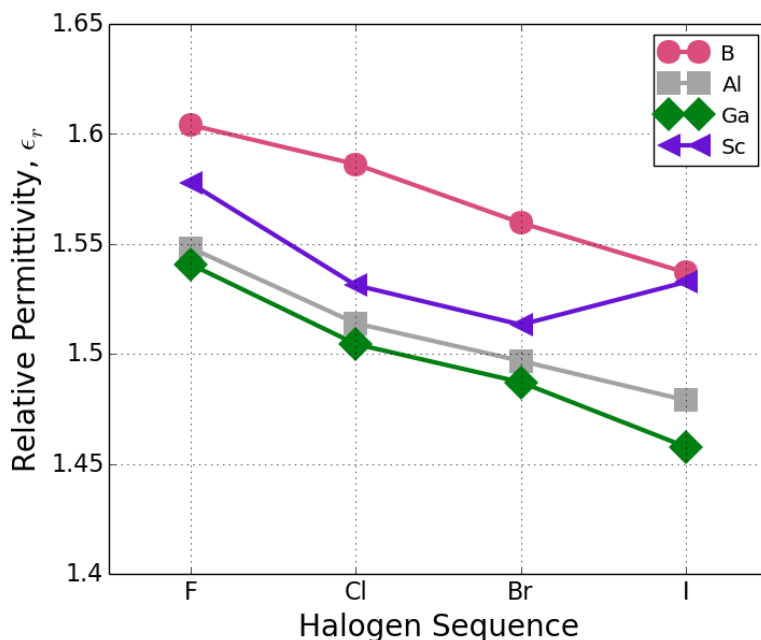
Figure 3.9. The static permittivity of the proposed derivatives is plotted against the halogen sequence.

Finally, we simulate the I-V curves for the solar cell of Ref. [31] using the methods contained therein. These simulations were carried out under the assumption that a quarter of the C_{60} sites are occupied with ball-in-cup aligned subphthalocyanine derivatives. The I-V curves for four derivatives are show in Figure 3.10. These include B-I as it has the largest molecular dipole moment, In-I as it has the smallest molecular dipole, Sc-F as it has the smallest molecular dipole of the derivatives that were found to be stable enough for crystal structure prediction, and B-Cl as it is the commonly known derivative. In this simulation, B-I can offer a small improvement over B-Cl.
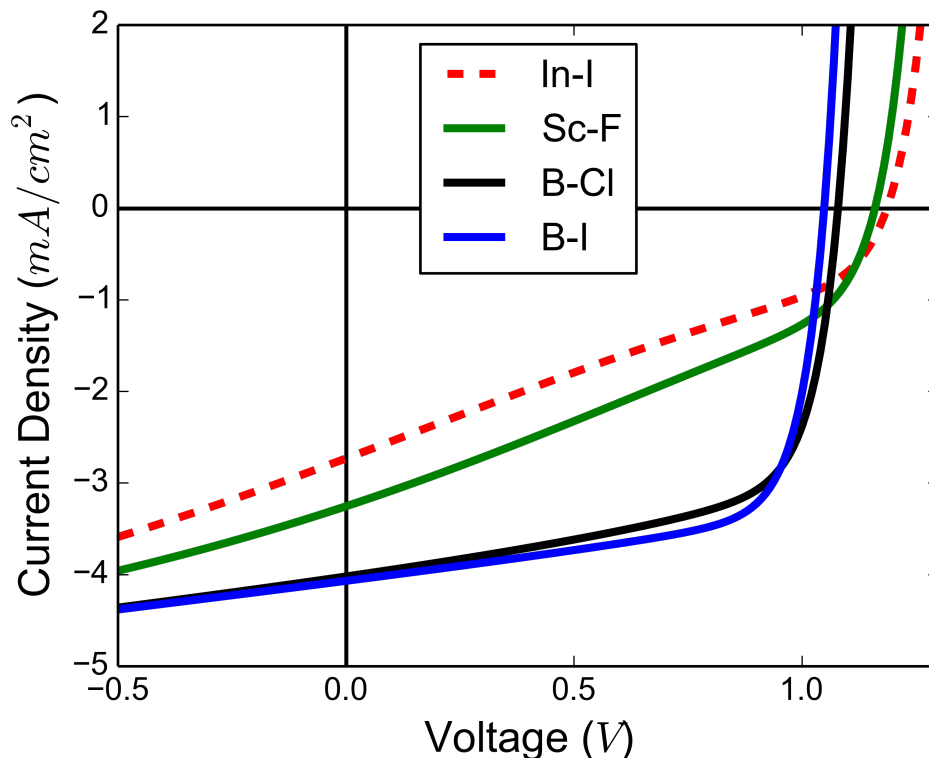
Figure 3.10. Simulated I-V curves for a device substituting four derivatives are plotted. This simulation assumes some molecular dipole ordering at the interface.

3.8 Conclusions

A series of concept SubPc molecules has been generated through systematic elemental substitutions. Calculation of their electronic properties and prediction of their crystal structures reveals several interesting trends that can guide device design. The degree of openness of the molecule canopy is controlled by trivalent atom. Molecular dipole moments range from 1 ~ 6 D. These may be used as another parameter device design. All crystal structures found are orthorhombic and belong to the space group *Pnma*. Predicted optical band gaps match experimental well, while the predicted spectra are accurate to first order. The static permittivities of the molecules are found to increase within the halogen sequence.

3.9 References

1.   Lewis, N. S. "Toward cost-effective solar energy use." Science 315 (5813): 798–801. (2007)

2.   Mutolo, K. L., E. I. Mayo, B. P. Rand, S. R. Forrest, and M. E. Thompson "Enhanced open-circuit voltage in subphthalocyanine/C60 organic photovoltaic cells." Journal of the American Chemical Society 128 (25): 8108–8109. (2006)

3.   Claessens, C. G., D. González-Rodríguez, and T. Torres "Subphthalocyanines: singular nonplanar aromatic compounds synthesis, reactivity, and physical properties." Chemical reviews 102 (3): 835–854. (2002)

4.   Fulford, M. V., D. Jaidka, A. S. Paton, G. E. Morse, E. R. L. Brisson, A. J. Lough, and T. P. Bender "Crystal Structures, Reaction Rates, and Selected Physical Properties of Halo-Boronsubphthalocyanines (Halo= Fluoride, Chloride, and Bromide)." Journal of Chemical & Engineering Data 57 (10): 2756–2765. (2012)

5.   Morse, G. E., and T. P. Bender "Boron Subphthalocyanines as Organic Electronic Materials." ACS Applied Materials & Interfaces 4 (10): 5055–5068. (2012)

6.   Diaz-Garcia, M. A., and F. Agullo-Lopez… "High second-order optical nonlinearities in subphthalocyanines." … and Laser Science … (1996)

7.   Kietaibl, H. "Die Kristall- und Moleklstruktur eines neuratigen phthalocyaninhnlichen Borkomplexes." Monatshefte fur Chemie 105 (2): 405–418. (1974)

8.   Rand, B. P., D. P. Burk, and S. R. Forrest "Offset energies at organic semiconductor heterojunctions and their influence on the open-circuit voltage of thin-film solar cells." Physical Review B 75 (11): 115327. (2007)

9.   Campbell, I. H., S. Rubin, T. A. Zawodzinski, J. D. Kress, R. L. Martin, D. L. Smith, N. N. Barashkov, and J. P. Ferraris "Controlling Schottky energy barriers in organic electronic devices using self-assembled monolayers." Physical Review B 54 (20): R14321. (1996)

10.   Wang, Y., J. Lv, L. Zhu, and Y. Ma "CALYPSO: A method for crystal structure prediction." Computer Physics Communications 183 (10): 2063–2070. (2012)

11.   Oganov, A. R., and C. W. Glass "Crystal structure prediction using ab initio evolutionary techniques: Principles and applications." The Journal of chemical physics 124 (24): 244704. (2006)

12.   Pettersson, L. A. A., L. S. Roman, and O. Inganäs "Modeling photocurrent action spectra of photovoltaic devices based on organic thin films." Journal of Applied Physics 86 (1): 487–496. (1999)

13.   Hanwell, M. D., D. E. Curtis, D. C. Lonie, T. Vandermeersch, E. Zurek, and G. R. Hutchison "Avogadro: an advanced semantic chemical editor, visualization, and analysis platform." Journal of cheminformatics 4 (1): 1–17. (2012)

14.   Becke, A. D. "Density-functional thermochemistry. III. The role of exact exchange." The Journal of Chemical Physics 98 5648. (1993)

15.   Vosko, S. H., L. Wilk, and M. Nusair "Accurate spin-dependent electron liquid correlation energies for local spin density calculations: a critical analysis." Canadian Journal of Physics 58 (8): 1200–1211. (1980)

16.   Lee, C., W. Yang, and R. G. Parr "Development of the Colle-Salvetti correlation-energy formula into a functional of the electron density." Physical Review B 37 (2): 785. (1988)

17.   Petersson, G. A., and M. A. Al-Laham "A complete basis set model chemistry. II. Open-shell systems and the total energies of the first-row atoms." The Journal of chemical physics 94 6081. (1991)

18.   Sosa, C., J. Andzelm, B. C. Elkin, E. Wimmer, K. D. Dobbs, and D. A. Dixon "A local density functional study of the structure and vibrational frequencies of molecular transition-metal compounds." The Journal of Physical Chemistry 96 (16): 6630–6636. (1992)

19.   Godbout, N., D. R. Salahub, J. Andzelm, and E. Wimmer "Optimization of Gaussian-type basis sets for local spin density functional calculations. Part I. Boron through neon, optimization technique and validation." Canadian Journal of Chemistry 70 (2): 560–571. (1992)

20.   Blöchl, P. E. "Projector augmented-wave method." Physical Review B 50 (24): 17953. (1994)

21.   Perdew, J. P., K. Burke, and M. Ernzerhof "Generalized gradient approximation made simple." Physical review letters 77 (18): 3865. (1996)

22.   Klimeš, J., D. R. Bowler, and A. Michaelides "Chemical accuracy for the van der Waals density functional." Journal of Physics: Condensed Matter 22 (2): 022201. (2010)

23.   Klimeš, J., D. R. Bowler, and A. Michaelides "Van der Waals density functionals applied to solids." Physical Review B 83 (19): 195131. (2011)

24.   Kosugi, N. "Strategies to vectorize conventional SCF-Cl algorithms." Theoretica chimica acta 72 (2): 149–173. (1987)

25.   Wang, Y., J. Lv, L. Zhu, and Y. Ma "Crystal structure prediction via particle-swarm optimization." Physical Review B 82 (9): 094116. (2010)

26.   Gajdoš, M., K. Hummer, G. Kresse, J. Furthmüller, and F. Bechstedt "Linear optical properties in the projector-augmented wave methodology." Physical Review B 73 (4): 045112. (2006)

27.   Onida, G., L. Reining, and A. Rubio "Electronic excitations: density-functional versus many-body Green's-function approaches." Reviews of Modern Physics 74 (2): 601. (2002)

28.   Gordan, O. D., M. Friedrich, and D. R. T. Zahn "The anisotropic dielectric function for copper phthalocyanine thin films." Organic electronics 5 (6): 291–297. (2004)

29.   Debe, M. K. "Variable angle spectroscopic ellipsometry studies of oriented phthalocyanine films. II. Copper phthalocyanine." Journal of Vacuum Science & Technology A 10 (4): 2816–2821. (1992)

30.   Heremans, P., D. Cheyns, and B. P. Rand "Strategies for increasing the efficiency of heterojunction organic solar cells: material selection and device architecture." Accounts of chemical research 42 (11): 1740–1747. (2009)

31.   S.E., Morris, B. D., S. M.E., H. H., W. M.J., K. J., K. J., and S. M. "Effect of axial halogen substitution on the performance of subphthalocyanine based organic photovoltaic cells." Organic Electronics 15 (12): 3660 − 3665. (2014)

32.   Fulford, M. V., D. Jaidka, A. S. Paton, G. E. Morse, E. R. L. Brisson, A. J. Lough, and T. P. Bender "Crystal Structures, Reaction Rates, and Selected Physical Properties of Halo-Boronsubphthalocyanines (Halo= Fluoride, Chloride, and Bromide)." Journal of Chemical & Engineering Data 57 (10): 2756–2765. (2012)

33.   Gommans, H. H. P., D. Cheyns, T. Aernouts, C. Girotto, J. Poortmans, and P. Heremans "Electro‐Optical Study of Subphthalocyanine in a Bilayer Organic Solar Cell." Advanced functional materials 17 (15): 2653–2658. (2007)

CHAPTER 4

Effect of Long-Range Electrostatics on Interfacial Excited States

4.0 Synopsis

Exciton dissociation at heterojunctions in photovoltaic devices is not completely understood despite being fundamentally necessary to generate electrical current. *Ab initio* based methods can yield the excited-state properties of materials with very good accuracy. One of the fundamental issues for *ab initio* calculations is that hybrid interfaces combining materials with Wannier-Mott excitons and those with Frenkel excitons can easily require thousands of atoms to encompass the exciton-wave function. The problem is further exacerbated by a large permittivity difference at the interface, which requires meso-scale boundary conditions to accurately predict electrostatic potentials. For these reasons, we have constructed a model of excited states at hybrid interfaces based on an effective mass Schrödinger equation. In this continuum model, carrier wave functions are represented by their envelope function rather than resolving the atomic scale variations. Electrostatic interactions are accounted for using the Poisson equation. For our model system, we use a pentacene/silicon interface. Because carrier mobility is low in pentacene relative to silicon, the hole is frozen such that it only interacts with the electron though an immobile positive charge density. The inputs to this model are as follows: dielectric permittivities, electron effective masses, interfacial width, band alignment, and the hole wave function.

4.1 Motivation and Background

As one of our solutions to building a renewable energy infrastructure, photovoltaics (PV) have been the subject of intense research. While traditional silicon solar cells still dominate the commercial market, significant effort has been devoted to finding and perfecting novel solar cell designs that can surpass silicon in terms of price, performance, and lifespan. In terms of efficiency, classical semiconductors such as silicon, gallium arsenide, etc. remain unmatched,[1] but these materials have relatively costly and demanding production techniques. Many emerging PV technologies have aimed to reduce production costs by using easier to manufacture materials rather than improve performance as a means of becoming more economically viable. These emerging technologies such as perovskite, organic, quantum dot, and dye-sensitized solar cells, combine very different materials in heterojunctions. These heterojunctions pose particular theoretical challenges for predicting charge transport across them. The problem comprises both corrections to the energetics and transport theory. In our previous work we discussed issues with the current state of the transport theory and addressed the issue of energetics with some semi-classical corrections. In this work, we have constructed a model based on the works of Stier *et al*. and Bolcatto *et al*. using the effective mass Schrödinger equation to self-consistently calculate excited states and energies at heterojunction interfaces.[2, 3] To better understand the reasons for the theoretical difficulties in addressing heterojunction excited states, a review excited states in bulk materials is included.

In bulk materials, electrons can be excited to bound states below the conduction band (or LUMO level), which are referred to as excitons. Excitons, which are comprised of an electron-hole pair, are bound via Coulomb interactions. The exciton binding energy refers to the additional energy required to excite the electron fully into the conduction band and separate the electron and hole. Materials with high dielectric constants and low carrier effective masses typically have Wannier-Mott type excitons, which are characterized by

79

being spread over many unit cells or molecules and having low binding energies that are quantized in similar way to the hydrogen atom. Materials with the opposite set of properties, low dielectric permittivity and high carrier effective masses, typically have Frenkel type excitons which are strongly bound and typically do not spread over more than a few atoms or molecules. From a theoretical standpoint, it is possible to calculate exciton binding energies for either type of material with good accuracy using the GW approximation and the Bethe-Salpeter equation.

The difficulty in analyzing heterojunctions using electronic structure calculation methods is that describing the interface requires a large real-space calculation so as not to represent a thinly layered structure. For a heterojunction using two Frenkel materials, it might be possible to use these methods because the Frenkel excitons are usually small enough to be computationally viable. But for a heterojunction containing a Wannier-Mott type material, the excited state volume requires far too much computational resource for most electronic structure methods. For heterojunctions containing two Wannier-Mott type materials, it is expected that excited state dissociation energies will be on the order of $k_B T$, like they are in the bulk, which makes their calculation less of a practical application and more theoretical curiosity. This leaves the case of a hybrid heterojunction between a Wannier-Mott and Frenkel type material where the excited state dissociation energies are conceivably large enough to be of practical consideration and their real-space volumes large enough for them to be inaccessible to a full treatment by atomic scale electronic structure calculations. For these reasons, we implement an effective mass Schrödinger equation model based on Stier *et al*. [2] and the frozen hole approximation.[4]

Before continuing, it is important to address the terminology used in this paper. When describing a bound excited state in relatively homogenous bulk material, we refer to the exciton binding energy as the energy required to separate the electron and hole in their lowest excited state from each other. However in real devices, we are interested in the

energy required to separate and collect carriers at opposite sides of the interface as this directly detracts from the open circuit voltage.[5] This leaves us with two different pictures: in the bulk the exciton must gain enough energy for the electron to reach the conduction band (Figure 4.1a). However at an interface, we want to know the energy required for the electron to reach the conduction band and then be collected far from the interface. The hole only needs to leave the interface to be collected in the opposite direction. For this reason we are reporting the dissociation energy for current collection across heterojunctions rather than the exciton binding energy. The difference in the LUMO and conduction band in Figure 4.1b is the band edge offset energy and is the energetic difference between the two schemes.
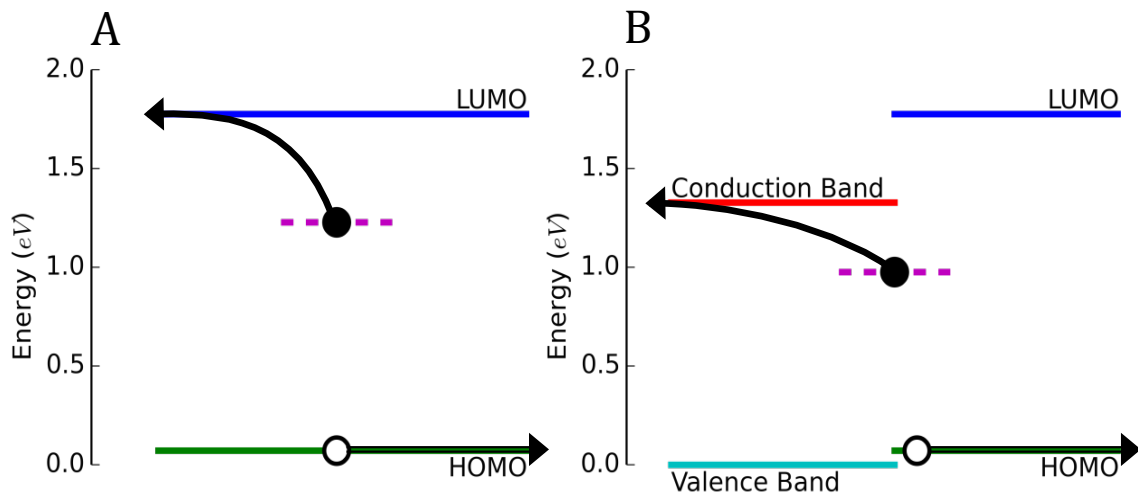

Figure 4.1. In (a), the dissociation energy of the excited state only requires that the electron and hole move far apart in any direction. In (b), the with the interface, the excited state dissociation energy for current collection is the energy required to move the electron into the conduction band and far away from the interface and the hole moving far in the opposite direction.

There is one final curious difference between Wannier-Mott and Frenkel excitons in their binding energy treatments. From a theoretical standpoint, the exciton binding energies of Wannier-Mott excitons are given as the lowest energy eigenvalue in a discrete spectrum of energy eigenvalues that goes as $E \sim 1/n^2$. For Frenkel excitons, the binding energy is

usually given as the Coulomb binding energy between the hole and the electron. The energy eigenvalues are, of course, a combination of kinetic energy and Coulomb interaction. The difference in formulation reflects that as Wannier-Mott excitons dissociate, their separate electron and hole wave functions are expected to become much more diffuse, whereas for Frenkel excitons they are expected to remain roughly the same spatially as they move farther away from each other. In our hybrid system, we treat the dissociation energy is calculated relative to an electron kinetic energy which becomes zero as it travels far into the silicon. We do not include the hole's kinetic energy because it is expected to change insignificantly as it travels away from the interface.

4.2 Theory

Our model development is not motivated by lack of accuracy of *ab initio* methods but rather by the desire to reduce computational cost. To simulate a Wannier exciton in a material where that excited stated extends over many unit cells requires inclusion of hundreds to thousands of atoms and description of their electron wave functions, when this is an excess of information and we are only interested in the electron and hole wave functions. For these reasons we opted to use the effective mass Schrodinger equation approach,[2, 6, 7] which uses envelope wave functions as perturbations of the rapidly varying wave functions at the atomic scale, see Figure 4.2 below. This approach has been used with quantum dots[8] and junction tunneling.[6] Fundamentally, these models could be considered second principles models because they use first principles models for input parameters and trade exact electronic structure for more accurate capture of the effect of meso-scale structures on electronic structure. In our implementation, we make no assumptions of wave functional forms. The Schrödinger equation is directly solved on a finite volume grid for electron wave functions and their energy eigenvalues. The effects of materials properties are incorporated through our electron Hamiltonian.
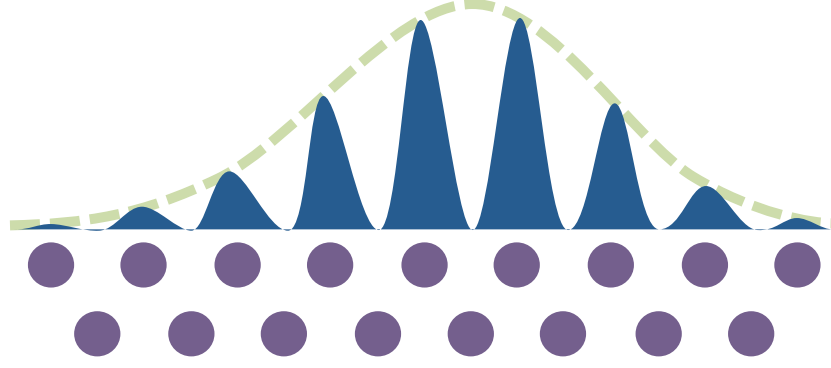
Figure 4.2. Trading the rapidly varying wave function (filled blue) for the slowly varying one (dashed green line).

Our electron Hamiltonian is composed of four terms: kinetic energy, Coulomb interaction between the hole and the electron, the effective potential from the band edge offset, and the self-polarization due to the interface (also known as image potential or self-energy).

$$\widehat{H}_e = -\frac{\hbar^2}{2}\nabla \cdot \frac{1}{m_e(z)}\nabla + q_e\phi_h + V_{band} + \Sigma_e.$$

We include the effective mass in the Laplacian because it produces better continuity across the interface due the change in effective mass.[6] The band edge offset potential, V_{band}, is a step function representing the difference between the LUMO of the pentacene and the conduction band of the silicon. The self-polarization potential, Σ_e, from the electron interacting with itself through the interface cannot be given in closed form, which will be discussed in further detail in the methods section.

The potential field, ϕ_h, created by the hole is obtained by solving the Poisson equation. By using anon-uniform the dielectric constant, we can capture the effect of the hole's 'image' charge on the electron. This formulation still requires the hole be represented by a charge density. From GW/BSE calculations; it is known that in pentacene crystals, excitons are delocalized over several intermolecular distances.[9]

$$q_h|\psi_h|^2 = -\nabla \cdot [\epsilon(z)\nabla\phi_h]$$

It would be convenient to replace the charge density and the Coulomb term with a molecular pseudopotential that is tuned to give the correct exciton binding energy, however this would fail to capture the effect of the holes 'image' charge on the electron that we get from solving Poisson's equation. We examined several hole charge densities for their effect on the exciton binding energy and found that simply adapting a Gaussian profile results in an exciton binding energy that matches the first principles calculations of Sharifzadeh *et al.*[9]

4.3 Algorithmic Implementation and Model Parameters

We implemented a self-consistent iteration scheme to solve the above Schrödinger equation in real space on a regular, finite-volume grid. While not a basis set in a traditional sense, we choose a discrete grid because standard atomic orbitals will not likely represent the effect of the abrupt transition near the interface. We also did not use plane waves because we are not using a periodic system. We implemented our model in FiPy[10] using PySparse's[11] precondition conjugate gradient solver (PCG) as the backend solver for both the Schrödinger equation and the Poisson equation. Higher energy states are calculated by performing numerically stable Gram-Schmidt orthonormalizations before each solver update of the wave function. This PCG solver is found to occasionally create non-converging oscillations in the wave function if too many iterations are performed between updates of the corresponding energy eigenvalue. However, increasing the number of iterations between eigenvalue updates yields a more quickly converging calculation. Our solution to improve the stability at a greater number of solver iterations per eigenvalue update is to mix old and new solutions for the wave function. Inspired by the DIIS method of Pulay,[12] we developed an efficient method for determining the optimal mixing parameter between old and new wave functions. We then coupled the optimal mixing parameter to the number of solver iterations per energy eigenvalue update via a rudimentary feedback algorithm (further described in Appendix 4.1). With this implementation, minimum energy electron wave

functions can be reliably calculated even if the wave function is assigned a random value at every grid point.

The classical result of the self-potential for a point charge near a sharp dielectric interface is inappropriate in this model due to the non-integrable singularity in the self-potential at the interface. We have elected to implement a diffuse dielectric interface model. To our knowledge, no closed form solution exists for the self-potential with a diffuse dielectric interface. Therefore, we implemented the numerical model for self-potential of a diffuse dielectric interface of Xue and Deng.[13] A plot of this dielectric constant and the image potential are shown in Figure 4.3. Our simplified implementation of the model of Xue and Deng is further detailed in Appendix 4.2.
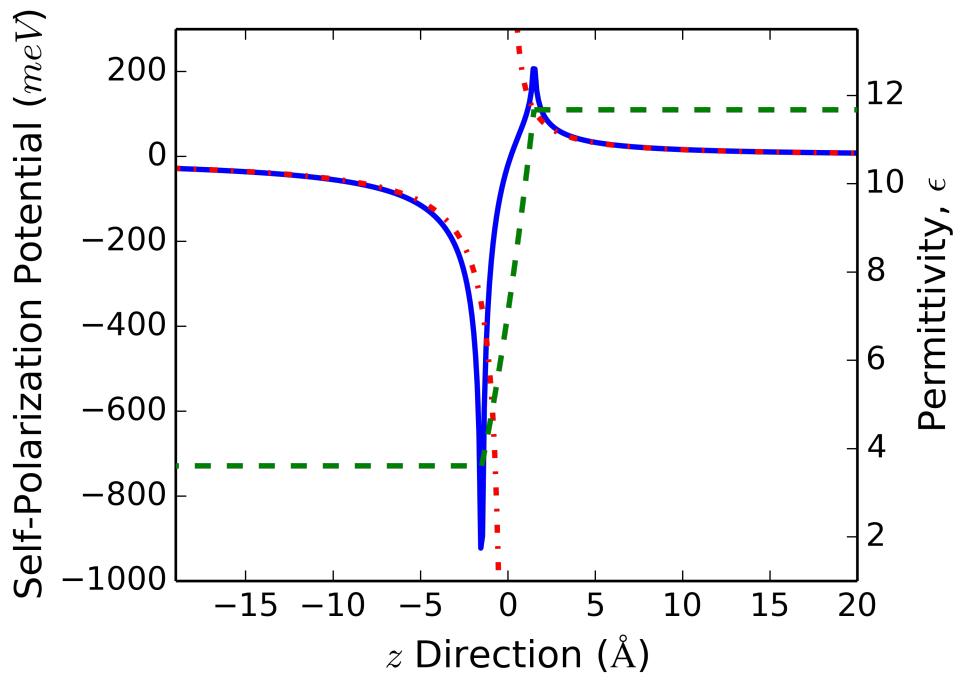

Figure 4.3. The dielectric permittivity relative to the interface is plotted with the green dashed line. The solid blue line is the calculated self-polarization energy and the dashed and doted red line is the divergent potential calculated for a sharp interface.

We created two versions of our simulation, a full three dimensional version and a two dimensional version, which, by assuming azimuthal symmetry about the axis normal to the

interface, allows the azimuthal coordinate of a cylindrical coordinate system to be eliminated, and thus reduces the memory requirements. Both are shown in Figure 4.4. Both cases use, effectively, the same parameters. The interface between the pentacene and silicon lies at half the vertical height of the simulation size. For wave functions, the Dirichlet boundary condition of $\psi = 0$ was applied at the exterior faces. For the hole potential calculated from the Poisson equation, mixed boundary conditions are used, with the Dirichlet boundary condition applied at the top and bottom faces, and the Neumann boundary condition of zero electric field at the lateral exterior faces. This combination of boundary conditions on the electric potential allows the application of external potentials mimicking a real device. As with Stier *et al.*, we find that for most cases, the spatial requirement to capture the electron wave function is much smaller (~10X) than the spatial requirement to converge the hole potential. Using the cylindrical version, we find that exciton binding energies change by less than 1 meV for a radial and axial size of 800 Å. For the 3D version, this translates to 800 Å in the vertical direction and approximately 1600 Å in the lateral direction. Although, for the full 3D case, this size scale is prohibitive, due mostly to memory limitations, smaller size scales proved useful in verifying that the ground state is indeed azimuthally symmetric and amenable to the less demanding 2D cylindrical model. For the grid spacing in the vertical direction, the sharpness of the self-polarization potential limits the spacing to 0.4 Å with an energy convergence of < 1 meV. In the radial direction, no such sharpness exists so the same energy convergence is achieved with a grid spacing of 1.0 Å. The Poisson equation is converged until PySparse reports a residual of less than 10^{-10}. Wave functions are iterated until the relative change in energy eigenvalue is less than 10^{-5}.
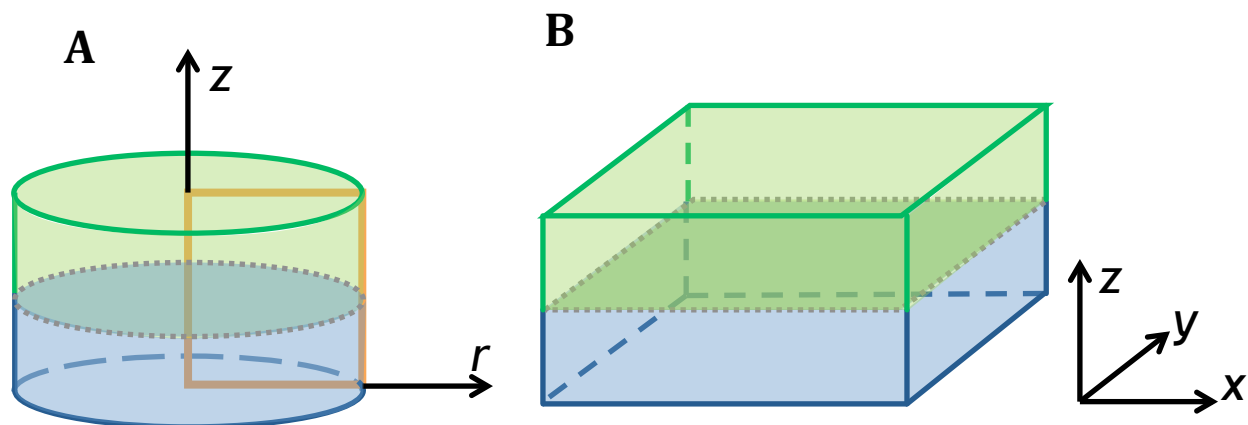
Figure 4.4. The two coordinate systems used in this work. For both, the green material represents the silicon and the blue represents the pentacene with the interface residing at half the z height. (a) The radially symmetric 2D cylindrical coordinates collapse the problem into a 2D grid inside the orange rectangle for which effectively larger simulations can be performed. (b)The standard 3D Cartesian coordinates are pictured.

For this model some materials parameters are required. These include the dielectric permittivities, the effective masses and the band offset between the LUMO of the pentacene and the conduction band of silicon. The values of the electron effective mass in pentacene and silicon are anisotropic which, while implementable in our model, was an unnecessary complexity for a first generation model, and thus representative values for both are taken from Refs [14] and [15]. The static dielectric permittivity of pentacene is taken as the average of the two experimental values presented in Ref.[16]. The LUMO of the pentacene molecule is found to be 478 meV above the conduction band of silicon in chapter 2 using the hybrid functional HSE06.[17] We chose a width,δ, of 3 Å for the width of the dielectric transition at the interface because our previous work indicates that this width completely fits between a pentacene molecule and silicon surface. The spacing is also in agreement with the work of Cappellini and Del Sole which indicates that 3 Å is the size scale for the dielectric constant of silicon to develop bulk behavior. [18]These values are presented in Table 4.1 below:

Table 4.1. The six materials parameters used in the model.

Static permittivity of silicon, ϵ_{Si}	11.68[19]
Static permittivity of pentacene, $\epsilon_{pentacene}$	3.61[16]
Electron effective mass in silicon, m_{Si}^*	1.0[15]
Electron effective mass in silicon, $m_{pentacene}^*$	4.0[14]
LUMO pentacene / Si conduction band difference	478 meV
Width of gradual dielectric interface, δ	3 Å

Before calculations of excited states at heterojunctions could be performed, the exciton binding energy of pentacene had to be reproduced. We use an azimuthally symmetric, Gaussian hole charge density because it can be used in both the two dimensional cylindrical and three dimensional models. The form of this charge density is described by the equation below.

$$\rho = \frac{q_h}{\sigma_z \sqrt{2\pi}} e^{-\frac{1}{2}\left(\frac{z-z_0}{\sigma_z}\right)^2} \frac{1}{2\pi\sigma_r^2} e^{-\frac{1}{2}\left(\frac{r}{\sigma_r}\right)^2}$$
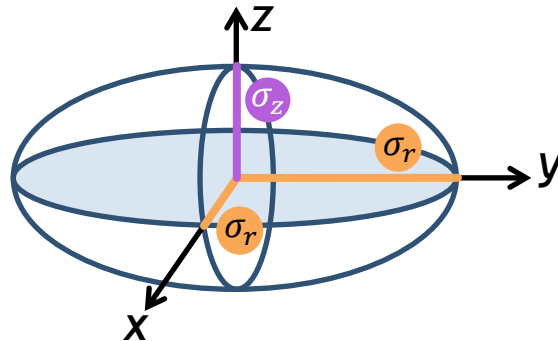

Figure 4.5. The azimuthally symmetric Gaussian density is roughly ellipsoidal where the principal axes in the x-y plane are the same.

A matrix of exciton binding energy calculations was performed varying both the thickness σ_z and width σ_r of the hole charge density to find values that reproduce the magnitude of 0.5 eV known from GW/BSE calculations and experiment.[9] This is shown in Figure 4.6. We opt for $\sigma_r = 6$ Åand $\sigma_z = 3$ Å because this corresponds approximately to twice the planar stacking distance of pentacene (≈3 Å) and twice the length (≈ 14 Å), and gives a Coulomb binding energy of 536 meV. This results in the electron wave function shown in Figure 4.6.

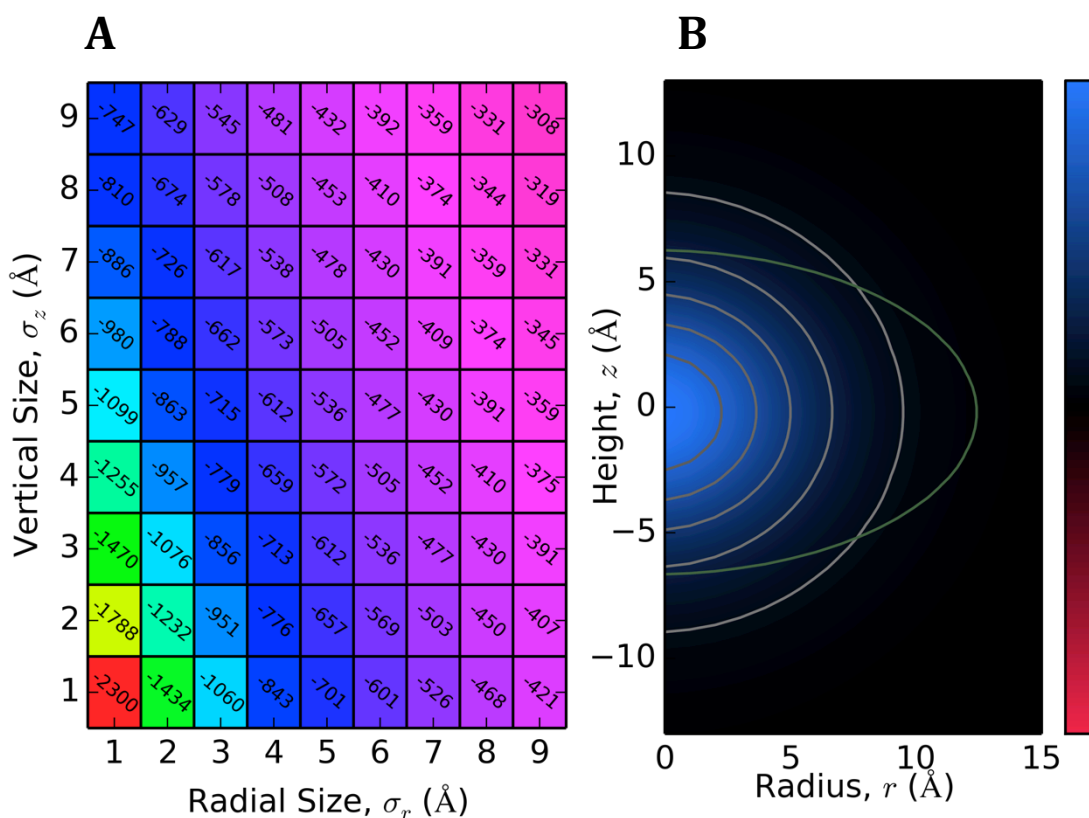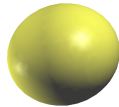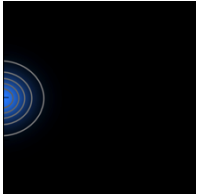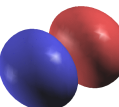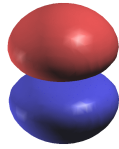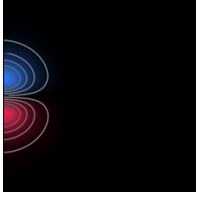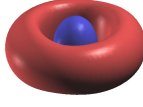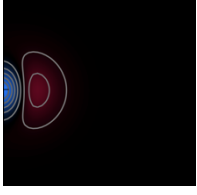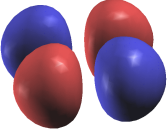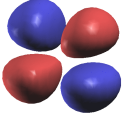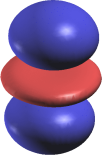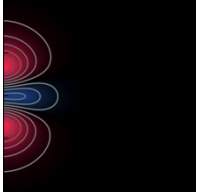**Figure 4.6. (a) The exciton binding energy of pentacene versus frozen hole charge density thickness and width parameters. Energies are shown in the square at corresponding width and thickness. (b) The first electron state is shown in blue/red for +/- values of the wave function. The green line is the isodensity contour containing 80% of hole charge density.**

The first few electron wave functions of the Gaussian hole are calculated using a reduced 3D size of 200 Å x 200 Å x 100 Å. While the electrostatic energies are under-represented due

to the poor Coulombic convergence from the smaller simulation size, the 3D azimuthally symmetric electron wave functions calculated correspond to the ones calculated with the 2D cylindrical model in both shape and energy eigenvalue. 3D states 1, 4, 5, and 10 match the 2D cylindrical wave functions states 1, 2, 3, and 4 in shape and are close in energy. The 3D states are consistently ~42 meV higher in energy eigenvalue. These results give confidence in our use of the 2D cylindrical model to find the exciton ground states.

Table 4.2. The 3D electron wave functions and their respective energy eigenvalues for a hole in pentacene. The corresponding 2D wave functions and their eigenvalues are given.

3D State	3D Eigenvalue (meV)	Corresponding 2D State	2D Eigenvalue(meV)
1	-417	1	-460
2	-327	-	-
3	-327	-	-
4	-298	2	-341
5	-258	3	-300

6	-249	-	-
7	-247	-	-
8	-223	-	-
9	-223	-	-
10	-213	4	-255

4.4 Results and Discussion

The effect of the hole position on the excited state dissociation energy has been examined by calculating the electron wave function for various distances between the hole and the interface. In Figure 4.7, we have plotted the exciton dissociation and Coulomb energies as a function of the distance from the interface with several of the electron wave functions shown. Moving the hole closer than 5 Å to the interface places a large fraction of

92

the hole density in the silicon, where this density is not optimal. We find that the excited state becomes more tightly bound as the hole moves closer to the interface. The electron wave function becomes more diffuse as the hole moves farther away from the interface. This widening can only be due to the weakening Coulomb interaction in the silicon as the hole moves farther away, since this is the only term in the Hamiltonian that depends on the hole position. We find that even if the hole is 100 Å away from the interface with silicon, the electron wave function is still located in the silicon. This result is surprising because the exciton binding energy is greater than the band offset energy. It seems that the band offset energy (pentacene LUMO/silicon conduction band difference) has a strong effect on the electron location.
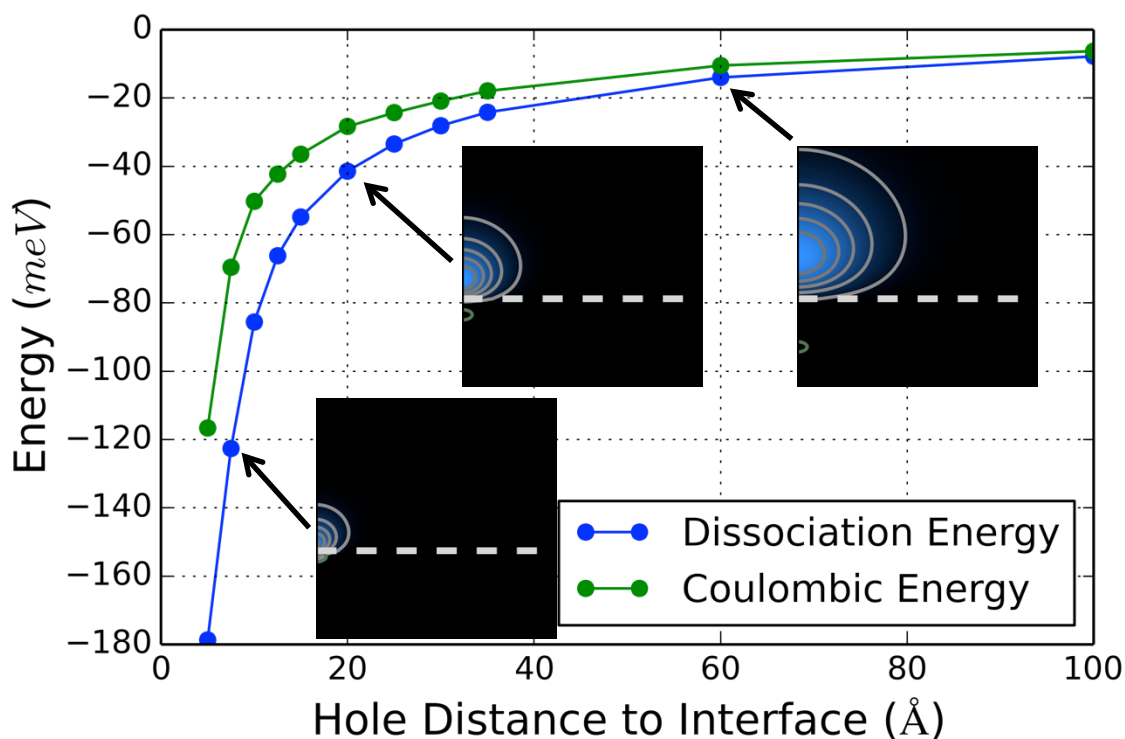
Figure 4.7. The dissociation energy (blue) and the Coulomb interaction (green) are plotted versus hole distance to the interface. Energies are reported such that negative values are binding. In the thumbnail images of the electron wave function (blue), the silicon is above the pentacene and the interface is denoted by the dashed white line. The small green half ellipse indicates the isodensity contour containing 80% of the hole. The same scale of 300 Å x 300 Å is used in each image.

To investigate the effect of band offset energy, a series of calculations were performed varying the band offset energy while the hole position is fixed at 20 Å from the silicon. We find that as the band offset energy increases, the first state energy of the electron residing in pentacene rises linearly until a critical band offset energy is reached, where the electron switches into silicon and beyond which the electron energy remains constant, as shown in Figure 4.8. Note that Figure 4.8 shows actual data, not a schematic. Below the critical band offset energy, the electron distribution inside the pentacene remains unchanged since band offset energy is a uniform potential applied to the pentacene. Above the critical band offset energy, the electron distribution in the silicon changes little because the coulomb interaction remains constant and only the height of the potential barrier to entering the pentacene changes. In other words, because the band offset energy is a flat potential in pentacene and once the electron switches to the silicon the electron no longer feels the band offset energy as a flat potential but as an increasingly tall potential barrier. Curiously, the critical band offset energy required to cause the electron to reside in the silicon (~425 meV) is smaller than both the energy eigenvalue (460 meV) and the Coulomb energy (536 meV) of the first electron state in the bulk pentacene exciton.
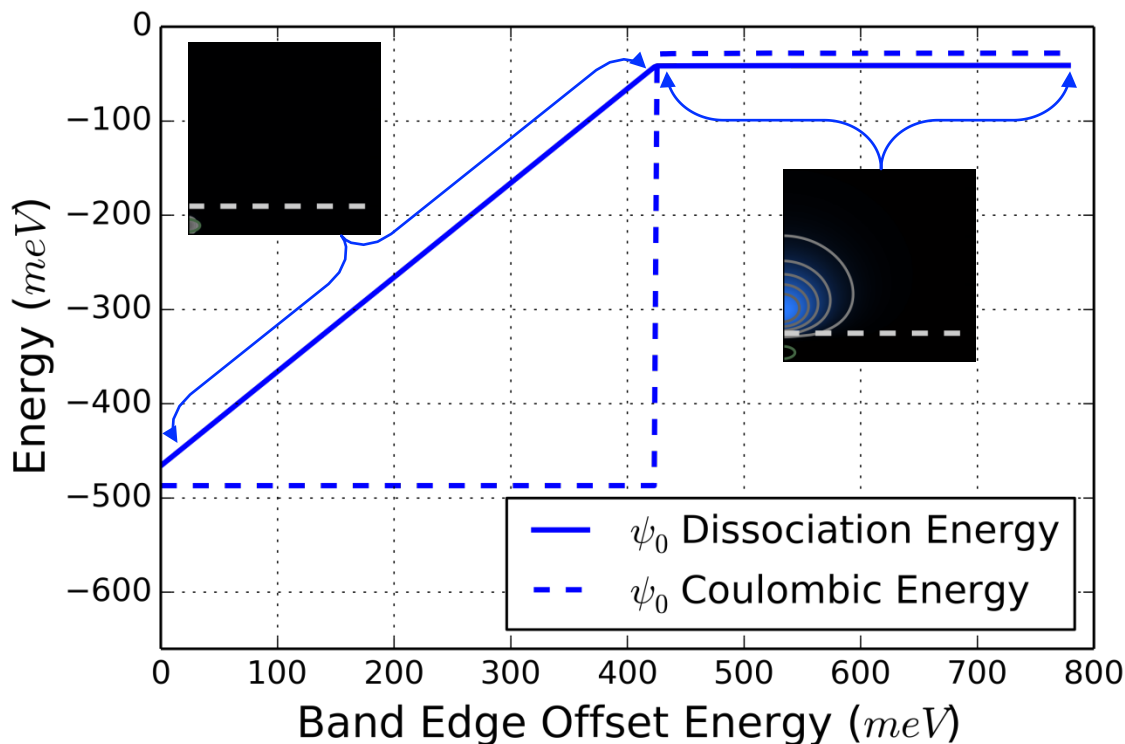
Figure 4.8. The dissociation energy and Coulomb energy are plotted versus the band edge offset energy. Energies are reported such that negative values are binding. Below the critical value the electron sits in the pentacene and above, it resides in the silicon.

If the next higher energy electron state is calculated, it can be seen (in Figure 4.9.) that the second state's wave function below the critical band edge offset energy is essentially the same as the first state's wave function above the critical band edge offset energy. The first and second states are not degenerate states at the critical band edge offset energy because they cannot be truly linearly independent as there is always some non-zero wave function overlap. Above the critical band edge offset energy, the second wave function's similarity to the higher order electron wave functions seen in Table 4.2, suggests that azimuthally symmetric, lower energy dumbbell states probably exist.

95
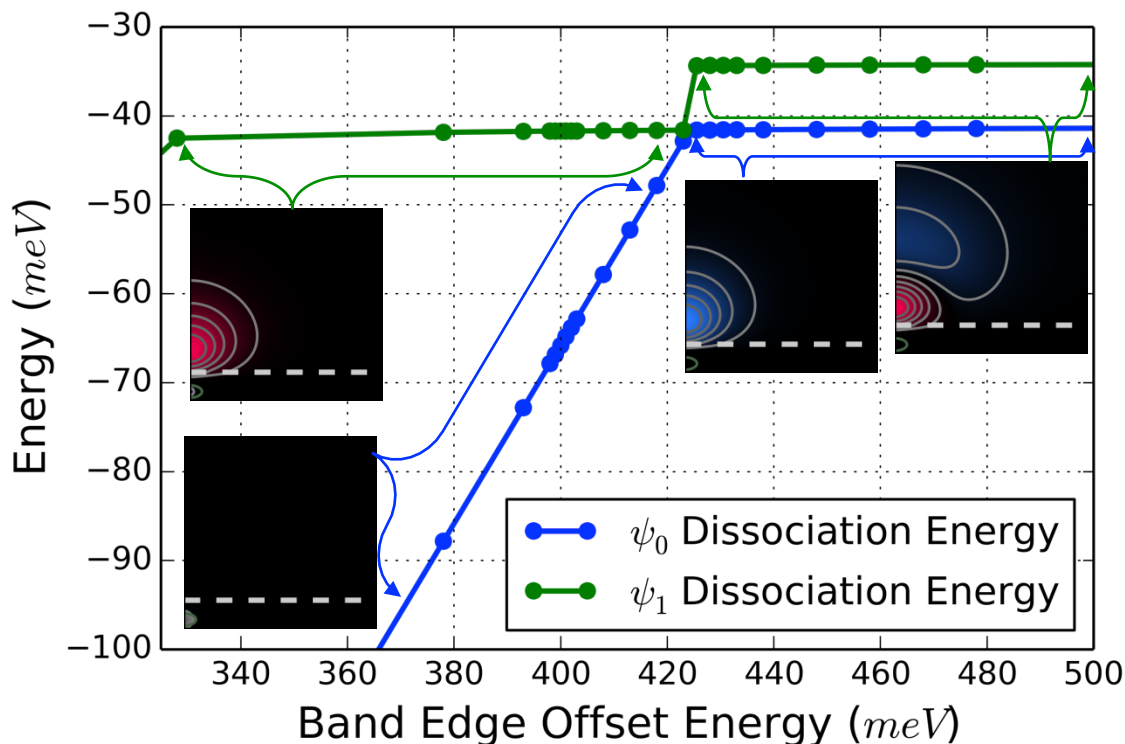
Figure 4.9. The dissociation energies and the wave functions of the first and second states of the electron are shown above as functions of the band edge offset energy. Energies are reported such that negative values are binding. The dissociation energy of the first state is shown in blue and the second in green. Positive and negative values of the wave functions are shown in blue and red respectively. The critical band edge offset energy is located at ~ 425 meV.

The sharp transition between the electron residing in the pentacene and the silicon persists for all reasonable distances between the hole and interface. The critical band edge offset energy is calculated for a series of hole distances in Figure 4.10. This establishes a design parameter space for the energetically favorable separation of electron and hole. Beyond ~ 15Å, the critical band edge offset is only affected by the Coulomb interaction between the hole and electron. Below ~ 15Å, the electron wave function begins to occupy a hybrid state between what would be the two lowest states if the hole was further from interface.
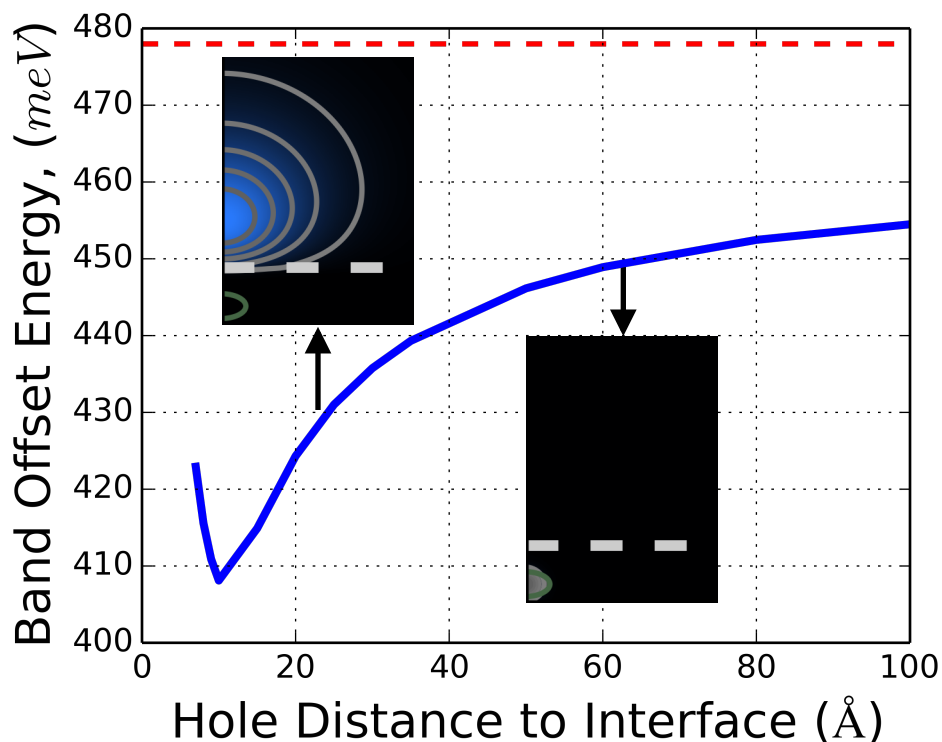
Figure 4.10. The critical band offset energy is plotted versus the hole distance to the interface. Above this line, it is favorable for the electron to reside in the silicon. Likewise, below the line, the electron prefers to reside in the pentacene. The dashed red indicated the band edge offset value used in Figure 4.7.

The model explored here is a significant step forward in capturing the long-range electrostatic interactions in excited states at interfaces for several reasons. The first is portability, this model can easily be used with other materials systems since only six materials and two hole parameters are required. The second is computational efficiency, most of these calculations were performed on a single desktop computer simply because it was more convenient than using the available high performance computing resources. The third is extensibility; while full size 3D calculations were found to be too expensive for this proof-of-concept implementation, off-the-shelf finite element codes with automatic mesh refinements exist, which can alleviate this problem. Finally, there is no theoretical reason that prevents the addition of arbitrary potentials, using the time-dependent Schrödinger equation, or even coupling to phase field models of ferroelectrics. However, before other

97

interface topologies can be implemented, an efficient computational means calculating self-polarization energies for arbitrary permittivity distributions must be found.

4.5 Conclusions

We have created an efficient model for incorporating the effects of long-range electrostatic effects on excited states at interfaces. We find that above a critical band edge offset energy, the electron is more stable in the silicon and exhibits Wannier-Mott type behavior. Below this value, the electron prefers to remain in the pentacene and exhibits Frenkel type behavior. Interestingly, this critical value is less than either the bulk exciton binding energy or energy eigenvalue of the first electron state in the pentacene exciton. Above the critical band edge offset energy, the size of Wannier-Mott type electron wave function is proportional to the frozen hole distance to the interface. As far as we know, this is the first time this behavior has been demonstrate in a hybrid inorganic/organic interface system.

4.6 Appendices

Appendix 4.1. Optimal Wave Function Mixer and Coupled Iteration Control Algorithm

To improve convergence and stability when iteratively minimizing the energy of an eigenstate wave function, we mix the old and the newly calculated wave function using a linear mixing parameter, α.

$$|\psi_{mixed}\rangle = \alpha|\psi_{new}\rangle + \beta|\psi_{old}\rangle$$

$$1 - \alpha = \beta$$

We have to then normalize the mixed wave function to get the final wave function:

$$|\psi_{final}\rangle = \frac{|\psi_{mixed}\rangle}{\sqrt{\langle\psi_{mixed}|\psi_{mixed}\rangle}}$$

What we really want is to minimize the final energy eigenvalue.

$$E_{final} = \langle\psi_{final}|\hat{H}|\psi_{final}\rangle$$

We can expand the final energy eigenvalue in terms of the mixing parameter:

$$E_{final} = \frac{\langle\psi_{mixed}|\hat{H}|\psi_{mixed}\rangle}{\langle\psi_{mixed}|\psi_{mixed}\rangle}$$

$$E_{final} = \frac{(\alpha\langle\psi_{new}| + \beta\langle\psi_{old}|)\hat{H}(\alpha|\psi_{new}\rangle + \beta|\psi_{old}\rangle)}{(\alpha\langle\psi_{new}| + \beta\langle\psi_{old}|)(\alpha|\psi_{new}\rangle + \beta|\psi_{old}\rangle)}$$

$$E_{final} = \frac{(\alpha\langle\psi_{new}| + \beta\langle\psi_{old}|)\hat{H}(\alpha|\psi_{new}\rangle + \beta|\psi_{old}\rangle)}{\alpha^2\langle\psi_{new}|\psi_{new}\rangle + \beta^2\langle\psi_{old}|\psi_{old}\rangle + \alpha\beta[\langle\psi_{new}|\psi_{old}\rangle + \langle\psi_{old}|\psi_{new}\rangle]}$$

E_{final}

$$= \frac{\alpha^2\langle\psi_{new}|\hat{H}|\psi_{new}\rangle + \beta^2\langle\psi_{old}|\hat{H}|\psi_{old}\rangle + \alpha\beta[\langle\psi_{new}|\hat{H}|\psi_{old}\rangle + \langle\psi_{old}|\hat{H}|\psi_{new}\rangle]}{\alpha^2\langle\psi_{new}|\psi_{new}\rangle + \beta^2\langle\psi_{old}|\psi_{old}\rangle + \alpha\beta[\langle\psi_{new}|\psi_{old}\rangle + \langle\psi_{old}|\psi_{new}\rangle]}$$

Since our old wave function is normalized and our new one can be easily normalized:

$$\langle\psi_{old}|\psi_{old}\rangle = 1$$

$$\langle\psi_{new}|\psi_{new}\rangle = 1$$

And since $\hat{H}$ doesn't change with iteration:

$$\langle\psi_{old}|\hat{H}|\psi_{old}\rangle = E_{old}$$

$$\langle\psi_{new}|\hat{H}|\psi_{new}\rangle = E_{new}$$

Also remember these identities:

$$\langle\psi_{new}|\psi_{old}\rangle^* = \langle\psi_{old}|\psi_{new}\rangle$$

$$\langle\psi_{old}|\hat{H}|\psi_{new}\rangle^* = \langle\psi_{new}|\hat{H}|\psi_{old}\rangle$$

We can clean up the final energy eigenvalue to a simpler form:

$$E_{final} = \frac{\alpha^2 E_{new} + \beta^2 E_{old} + \alpha\beta[\langle\psi_{old}|\hat{H}|\psi_{new}\rangle^* + \langle\psi_{old}|\hat{H}|\psi_{new}\rangle]}{\alpha^2 + \beta^2 + \alpha\beta[\langle\psi_{old}|\psi_{new}\rangle^* + \langle\psi_{old}|\psi_{new}\rangle]}$$

But for any complex number:

$$z^* + z = 2\text{Re}\{z\}$$

so:

$$E_{final} = \frac{\alpha^2 E_{new} + \beta^2 E_{old} + 2\alpha\beta\text{Re}\{\langle\psi_{old}|\hat{H}|\psi_{new}\rangle\}}{\alpha^2 + \beta^2 + 2\alpha\beta\text{Re}\{\langle\psi_{old}|\psi_{new}\rangle\}}$$

And for simplicity:

$$V_{on} = \text{Re}\{\langle\psi_{old}|\hat{H}|\psi_{new}\rangle\}$$

$$P_{on} = \text{Re}\{\langle\psi_{old}|\psi_{new}\rangle\}$$

So:

$$E_{final} = \frac{\alpha^2 E_{new} + \beta^2 E_{old} + 2\alpha\beta V_{on}}{\alpha^2 + \beta^2 + 2\alpha\beta P_{on}}$$

Also note that there are no complex terms here, which is nice.

We can substitute α for β:

$$E_{final} = \frac{\alpha^2 E_{new} + (1-\alpha)^2 E_{old} + 2\alpha(1-\alpha)V_{on}}{\alpha^2 + (1-\alpha)^2 + 2\alpha(1-\alpha)P_{on}}$$

We compute the derivative to minimize E_{final} with respect to α.

$$\frac{\partial E_{final}}{\partial\alpha}$$
$$= \frac{2[(P_{on}-1)(E_{new}-E_{old})\alpha^2 + (2P_{on}E_{old} - 2V_{on} + E_{new} - E_{old})\alpha + (V_{on} - P_{on}E_{old})]}{[2\alpha^2(P_{on}-1) - 2\alpha(P_{on}-1) - 1]^2}$$

Since we are looking for extrema, we need the zeros of the numerator this rational function since the denominator is always positive. Using the quadratic equation to find the zeros of the numerator gives two values of α that correspond to the extrema points.

$$(P_{on}-1)(E_{new}-E_{old}) = a$$

$$2P_{on}E_{old} - 2V_{on} + E_{new} - E_{old} = b$$

$$V_{on} - P_{on}E_{old} = c$$

$$\alpha_{ex} = \frac{-b \pm \sqrt{b^2 - 4ac}}{2a}$$

We know which roots we want based on the concavity of the numerator, if the function is concave up, then the minima occurs at the larger root. If the function is concave down, the minima occurs at smaller root. We can write this simply:

$$\alpha_{optimal} = \frac{-b + \text{sign}(a)\sqrt{b^2 - 4ac}}{2a}$$

If the discriminant is negative there is no optimal value inside the bounds of $(0,1]$. If the computed $\alpha_{optimal}$, is less than 0, there is no optimal value inside the bounds of $(0,1]$. In both cases we simply defer to a preset minimum value of the mixing parameter. If the computed value of $\alpha_{optimal}$ is greater than one, we simply use $\alpha_{optimal} = 1$. We couple the value of $\alpha_{optimal}$ to the number of solver iterations used per step through a rudimentary control mechanism. If the minimum value of the mixing parameter we used, we decrease the number of solver iterations. If the value of $\alpha_{optimal}$ is greater than some cut-off value (usually 0.8) the number if solver iterations is increased. Using this method, the energies converge more quickly and less noisily while the solver rarely requires any hand tuning.

Appendix 4.2. Numerical Model For The Self-Potential of a Point Charge near a Gradual Dielectric Interface.

This model is taken from Xue and Deng and has been reformulated to be concise and easier to implement. [13]The dielectric function is defined as a piecewise function:

$$\beta = \frac{\sqrt{\epsilon_{High}} - \sqrt{\epsilon_{Low}}}{\delta}$$

$$\alpha = \frac{\sqrt{\epsilon_{High}} + \sqrt{\epsilon_{Low}}}{2}$$

$$\epsilon(z) = \begin{cases} \epsilon_{Low}, & z \leq -\dfrac{\delta}{2} \\ (\alpha + \beta z)^2, & -\dfrac{\delta}{2} < z < \dfrac{\delta}{2} \\ \epsilon_{High}, & z \geq \dfrac{\delta}{2} \end{cases}$$

The self-polarization potential energy (or image potential energy) as a function of the source point charge position z_s is given by:

$$\Sigma_e(z_s) = \frac{Q_s}{2} \int_0^\infty \frac{F(k, z_s)}{8\pi} dk$$

The charge of the self-interaction particle is Q_s and the famous ½ term is due to this being a self-energy. The function F is the difference between the Coulomb Green's function for the gradual interface and the ordinary Coulomb Green's in a Fourier-Bessel form. Unsurprisingly, F is also piecewise and is defined as follows.

$$F(z_s) = \begin{cases} F_{Low}, & z_s \leq -\dfrac{\delta}{2} \\[2ex] F_{Inter}, & -\dfrac{\delta}{2} < z_s < \dfrac{\delta}{2} \\[2ex] F_{High}, & z_s \geq \dfrac{\delta}{2} \end{cases}$$

$$F_{Low} = \frac{Q_s}{\epsilon_{Low}S(k)} e^{2kz_s} 2\beta \left[k \left(\sqrt{\epsilon_{High}} e^{k\delta} - \sqrt{\epsilon_{Low}} e^{-k\delta} \right) - \beta \sinh k\delta \right]$$

F_{Inter}

$$= \frac{Q_s}{\epsilon(z_s)S(k)} e^{-k\delta} 2\beta \left[k \left(\sqrt{\epsilon_{High}} e^{-2kz_s} - \sqrt{\epsilon_{Low}} e^{2kz_s} \right) + \beta \left(e^{-k\delta} - \cosh 2kz_s \right) \right]$$

$$F_{High} = \frac{Q_s}{\epsilon_{High}S(k)} e^{-2kz_s} 2\beta \left[k \left(\sqrt{\epsilon_{High}} e^{-k\delta} - \sqrt{\epsilon_{Low}} e^{\delta k} \right) - \beta \sinh k\delta \right]$$

We separate the dominator as a separate function since it has no dependence on z_s

$$S(k) = \left(-2k\sqrt{\epsilon_{High}} + \beta \right) \left(2k\sqrt{\epsilon_{Low}} + \beta \right) - \beta^2 e^{-2k\delta}$$

For our numerical evaluation of the self-polarization potential energy integral, we simply used Simpson's rule with $dk = 0.001 \text{ Å}^{-1}$ and $k_{max} = 100 \text{ Å}^{-1}$ which provides us with sufficient accuracy. For anyone wishing to reproduce this work, we suggest reading Refs. [13] and [20].

4.7 References

1.   National Center for Photovoltaics "Best Research-Cell Efficiencies." (2015)

2.   Stier, O. "Electronic and optical properties of strained quantum dots modeled by 8-band k · p theory." Physical Review B 59 (8): 5688–5701. (1999)

3.   P, G. B., and R. P. C "Partially confined excitons in semiconductor nanocrystals with a finite size dielectric interface." Journal of Physics: Condensed Matter 13 (2): 319. (2001)

4.   Pahl, E., and U. Birkenheuer "Frozen local hole approximation." J. Chem. Phys. 124 (21): 214101. (2006)

5.   Renshaw, C. K., and S. R. Forrest "Excited state and charge dynamics of hybrid organic/inorganic heterojunctions. I. Theory." Phys. Rev. B 90 (4): (2014)

6.   BenDaniel, D. J. "Space-Charge Effects on Electron Tunneling." Physical Review 152 (2): 683–692. (1966)

7.   Li, Y., O. Voskoboynikov, C. P. Lee, and S. M. Sze "Computer simulation of electron energy levels for different shape InAs/GaAs semiconductor quantum dots." Computer Physics Communications 141 (1): 66–72. (2001)

8.   Movilla, J. L., and J. Planelles "Image charges in spherical quantum dots with an off-centered impurity: algorithm and numerical results." Computer Physics Communications 170 (2): 144–152. (2005)

9.   Sharifzadeh, S., Ariel Biller, L. Kronik, and J. B. Neaton "Quasiparticle and optical spectroscopy of the organic semiconductors pentacene and PTCDA from first principles." Physical Review B 85 (12): 125307. (2012)

10.   Jonathan, E. G., W. Daniel, and A. W. James "FiPy: Partial Differential Equations with Python." Computing in Science & Engineering 1 6–15. (009)

11.   Geus, R., and Peter Arbenz. "PySparse and PyFemax: A Python framework for large scale sparse linear algebra." PyCon'03 (2003)

12.   Pulay, P. "ImprovedSCF convergence acceleration." J. Comput. Chem. 3 (4): 556–560. (1982)

13.   Xue, C., and S. Deng "Coulomb Green's function and image potential near a planar diffuse interface, revisited." Computer Physics Communications 184 (1): 51–59. (2013)

14.   Doi, K., K. Yoshida, H. Nakano, A. Tachibana, T. Tanabe, Y. Kojima, and K. Okazaki "Ab initio calculation of electron effective masses in solid pentacene." J. Appl. Phys. 98 (11): 113709. (2005)

15.   Green, M. A. "Intrinsic concentration, effective densities of states, and effective mass in silicon." Journal of Applied Physics 67 (6): 2944–2954. (1990)

16.   Kim, C. H., O. Yaghmazadeh, D. Tondelier, Y. B. Jeong, Y. Bonnassieux, and G. Horowitz "Capacitive behavior of pentacene-based diodes: Quasistatic dielectric constant and dielectric strength." J. Appl. Phys. 109 (8): 083710. (2011)

17.   Krukau, A. V., O. A. Vydrov, A. F. Izmaylov, and G. E. Scuseria "Influence of the exchange screening parameter on the performance of screened hybrid functionals." J. Chem. Phys. 125 (22): (2006)

18.	Cappellini, G. "Model dielectric function for semiconductors." Physical Review B 47 (15): 9892–9895. (1993)

19.	Dunlap, W. C. "Direct Measurement of the Dielectric Constants of Silicon and Germanium." Physical Review 92 (6): 1396–1397. (1953)

20.	Stern, F. "Image potential near a gradual interface between two dielectrics." Physical Review B 17 (12): 5009–5015. (1978)

CHAPTER 5

Outlook

Computer-based materials modeling has made substantial progress in the last 30 years, with great strides in both available computing power, and computational methodology. Prediction of materials properties via simulation is becoming routine, accurate, and more important across almost all materials systems. However, there still exists the grand challenge in materials science of predicting crystal structures especially from molecular structures. For any reliable means of high throughput design of molecular materials, there will need to be improvements to the current methods.

In this work, I have predicted the structure of a series of subphthalocyanine-based compounds that have never been synthesized, and their crystal structures, symmetry, optical band gaps and permittivities. The ability to examine new compounds for design of materials is a key point in the development of modern technology. Furthermore, I have applied similar techniques to the examination of organic-silicon interfaces, and calculated corrections for the long-range electrostatic effects on the excited states. Finally, I have created a self-consistent model to understand the excited state structure of an organic/inorganic interface. Through this approach, I gained deeper insight into the behavior of excited states at this complex boundary, which will allow further understanding and engineering new hybrid organic/inorganic materials for energy production. With all of this, there is still a great deal left to explore in terms of accurate electronic modeling of materials.

In the realm of interfacial engineering, there are more interface topologies that can be investigated beyond the simple planar interfaces used here in chapters 2 and 4. There is enough, probably, to create another thesis. Yet, the classical self-polarization energy of point charges seems to lack any efficient algorithm for the one to one mapping from permittivity to self-polarization energy. If this is not equivalent to another problem class, then there is likely a very good applied mathematics publication to be had. This would also be a good edition to any future second-principles models.

In the literature regarding these second principles models, there is almost no application of time-dependence in any form, which would be useful to capture dissociation kinetics. There are several ways to attempt this: direct implementation of the time-dependent Schrodinger equation, the use of non-equilibrium Green's functions, the time-dependent Bethe-Salpeter equation, and possibly kinetic Monte Carlo. The merits of each would have to be investigated.

Another question with second principles models, is there a self-consistent means to un-freeze the hole, which produces reasonable results for the exciton binding energy and hole wave function while using realistic inputs? Could molecular site energies be used better localize the hole (and possibly electron) while giving good results and what would that formulation look like?

In terms of improving solar cells, all of this thesis will not be helpful if no materials system can ever best the reigning champion, silicon, but at this point it is not known what the best technology will turn out to be. Furthermore, these results have direct application to organic light emitting diodes, which are already in use as displays. It is likely that these models could be helpful, albeit in the reverse process, of light production.